Intercalation of carbon nanotube layer for fabrication of high-performance thin film composite membrane for efficient separation

鄧, 璐遥

(Degree)
博士（学術）

(Date of Degree)
2024-03-25

(Date of Publication)
2025-03-01

(Resource Type)
doctoral thesis

(Report Number)
甲第8938号

(URL)
https://hdl.handle.net/20.500.14094/0100490163

Doctoral Dissertation

Intercalation of carbon nanotube layer for fabrication of high-performance thin film composite membrane for efficient separation

(効率的分離のための高性能薄層複合膜作製を目指したカーボンナノチューブインターカレーションに関する研究)

January 2024

Graduate School of Engineering,
Kobe University

DENG LUYAO
鄧　璐遥

Acknowledgments

First and foremost, I would like to thank my supervisor Prof. Matsuyama Hideto for his guidance throughout my doctoral study. I thank him for offering me such a good environment to do research, and providing suggestions and encouragement when I encounter difficulties. It has been a privilege to learn from such an inspirational mentor, who would always push me to achieve the best I can; the experience of which will remain with me for the rest of my life.

Special thanks are given to Dr. Gonzales Rolly Ralph, who never tires of giving guidance and solutions for every problem that I have ever had, and promoting the research to a new level. I thank him for every discussion and revision, and every drinking night we had during those struggle time.

I am grateful to Dr. Takagi Ryosuke, Dr. Xu Guorong, Dr. Guan Kecheng and Dr. Matsuoka Atsushi and for the lengthy discussion and experimental help. A special mention must go to Dr. Takagi Ryosuke who gave every single suggestion from experimental to discussion during the group meeting. All those arguments we had are bringing new solutions and making the research work better.

I also wish to thank seniors from the research group, Dr. Xu Ping, Dr. Hu Mengyang, Dr. Zhang Pengfei, Dr. Mai Zhaohuan and Dr. Li Zhan for their constant support. I thank Xiang Shang, Ji Wenhui, Zhou Siyu, Fang Shang, Fu Wenming, Wang Zheng, He Shengnan and Shi Yongxuan for their constant support and kindness concern.

Last and importantly, I would like to express my deepest gratitude to my friends, family, especially my parents, Deng Dianping and Liu Jiaying, and my husband, Luo Kun. You are my strongest supporters during my whole doctoral study. I love you all!

Abstract

Carbon nanotube (CNT) interlayer intercalation is a popular way to improve the performance of thin-film composite (TFC) polyamide (PA)membrane by forming an interlayer between PA selective layer and substrate layer. However, this modification is still in its infancy and remains problems unsolved. To better understand the function of CNT in TFC membranes, this dissertation offers a comprehensive study into the influence of CNT interlayer intercalation on shaping the surface morphology and properties of TFC PA membrane, and enhancing the membrane performance in both aqueous and non-aqueous application.

Firstly, through fabricating the interlayered TFC membrane with different CNT interlayer thickness (i.e., CNT loading amount), the transition of PA morphology and surface charges were fully investigated, and were confirmed as a result of enhanced monomer release during interfacial polymerization (IP), due to the hydrophobic nature of pristine CNT which reduced the interaction between polyketone (PK) substrate and IP monomer in aqueous phase. The cross-linking degree of PA layer was proved to be increased and highly correlated to its zeta potential value, demonstrating an interesting way to obtain a neutral PA surface by adjusting the CNT interlayer thickness. Consequently, the neutral CNT-interlayered TFC membrane was fabricated at a certain CNT loading amount, and demonstrated to have excellent desalination and antifouling performances in aqueous reverse osmosis (RO) system. This work gave a unique perspective on how the CNT interlayer works in the TFC membrane, which offered references to other interlayer materials on understanding their mechanisms.

Secondly, after reaching a success in aqueous system, the CNT-interlayered TFC membrane was further applied to the non-aqueous system of organic solvent nanofiltration (OSN). The CNT-interlayered TFC membrane was able to selectively retain smaller molecules such as dyes and sugars, even in organic solvent environments. OSN tests revealed that the optimal membrane displayed a methanol permeance of 5.34 L m^{-2} h^{-1}/bar with an extremely low molecular weight cut-off (MWCO) of 170-180

g/mol, which was much lower than the reported work using CNT interlayer. These results were attributed to the reduced PA intrusion, enlarged PA filtration area, and the gutter layer effect brought about by the CNT interlayer. Furthermore, the CNT interlayer was shown to have high tolerance against organic solvents.

Finally, given that excellent performances were achieved during OSN application, further application expansion of CNT-interlayered TFC membrane to solvent-solvent separation was conducted in organic solvent reverse osmosis (OSRO) process. Considering that a highly cross-linked PA layer is required for solvent separation, a polydopamine (PDA)-modified CNT interlayer were applied to prepared the CNT-interlayered TFC membrane for the purpose of increasing the IP monomer adsorption on the basis of CNT enhanced monomer release. The resultant CNT-interlayered TFC membrane demonstrated excellent performances in OSRO with membrane permeances enhanced three times higher with rejection remained at 99.2% when using 5 wt% methyl tertbutyl ether (MTBE) in methanol. By comparing the separation performances of three different kinds of solvent combinations (methanol/toluene, methanol/MTBE, and acetonitrile/toluene), the interactions between selective layer and different solvent mixtures were first considered as one of the factors affecting the rejection, and were analyzed based on Hansen solubility parameters (HSP) theory. Even if a huge polarity difference existed between two components, the mixture of the two could have a strong interaction with the membrane, resulting in a lower separation performance. This work provides insights into the high-performance OSRO membrane design and the solvent separation mechanism.

In summary, this dissertation placed a high emphasis on the function of CNT intercalation on modifying the TFC PA membrane from the perspective of high-quality PA generation and PA surface property regulation. This study demonstrates the CNT-dependent regulation to the property and performance of TFC membrane, such capabilities could aid in the development of next-generation TFC membranes.

Contents

Chapter 1 General Introduction

1.1. Research background

1.1.1. Water scarcity and industrial by-products

With the development of society and economy, the world's population continues to grow, resulting in increasing resource shortages and serious environmental pollution. One of the typical examples is the global water scarcity and pollution [1]. Water is the most widespread substance found in the natural environment and organisms. Although 71% of our planet surface is covered by water and current estimation shows that the Earth's hydrosphere contains a huge amount of water about 1386 million cubic kilometres [2, 3], 97.5% of this amount are saline waters which cannot be consumed directly and only 2.5% is fresh water. Unfortunately, only 0.26% of the total amount of fresh waters are concentrated in lakes, reservoirs and river systems where they are most easily accessible for our economic needs and absolutely vital for water ecosystems [3, 4]. The great renovation and self-purification of waters during the global water cycle gave a birth of illusion of immutability and inexhaustibility of water resources to human being who take this gift for granted from mother of nature. However, the truth is that the water cycle and renovation are determined not only by natural climate as previously, but now also by human's economic activities. The ever-increasing pollution of natural waters has aggravated the qualitative depletion of water resources. Industrial and municipal wastewater as well as water returning from irrigated areas are the major sources of intensive pollution of waterways and water bodies, which leads to a severe situation of fresh water shortage.

Another non-negligible issue is overuse of the fossil fuels which inevitably causes the pollution of environment and water bodies. For example, the rapid development of petrochemical, fine chemical and biopharmaceutical industries has met human society's needs for materials and chemicals. However, these industries involve many organic

synthesis reactions, target compound separation, catalyst recovery and other processes, which require a huge amount of organic solvent during the production of chemicals [5, 6]. The processing of downstream products such as these solvent mixtures has become an issue that industry must concern. Most of the solvent mixtures are disposed by incineration and landfill [7, 8], causing serious environmental pollution and excessive carbon emissions. Therefore, whether it is wastewater or industrial solvent mixtures, if these waste resources can be recycled and reused, it will greatly alleviate the energy crisis and environmental problems of human society.

1.1.2. Traditional thermal-based separation and purification technologies

Separation and purification are important links in industrial production. By separating the various components in the mixture, products with higher purity can be obtained. Separation and purification processes, which involve the technologies of evaporation, distillation, crystallization, adsorption-based separation, and extraction, etc. [9, 10], constitute one of the standard configurations in modern industries including pharmaceutical, food processing, petrochemicals, and water treatment. Currently, the most widely used separation and purification method in industry is the thermal-based separation process, such as distillation, which uses heating and cooling to separate the mixture into different components based on the difference in saturated vapor pressure of each component in the mixture. Although high separation efficiency enables these thermal-based separation facilities into large-scale application, the extremely high energy consumption still poses a threat to environment with large carbon footprint. Researches have shown that these conventional energy-intensive separation approaches account for 10–15% of the world's energy consumption, which could leave a large carbon footprint [6]. Distillation also faces a big challenge in separating azeotropes due to the similar boiling point of each component [11]. All these limitations motivate engineers and scientists to explore new environmentally-benign alternative separation technologies.

1.2. Membrane technologies and membranes

Membrane separation technology, emerged in 1960s, is an established separation process for both gaseous and liquid feed streams, with demand for membranes ranging from pore sizes of several hundred nanometres down to <1 nm. Due to the advantages of small footprint, high efficiency and integration, and less energy consumption, the membrane technologies show great potential in replacing the traditional thermal-based separation processes and becoming the mainstream in the global separation and purification market [12-14]. By using a driving force, the membrane technology can selectively separate molecules from mixtures through pressing the mixture to pass through a thin film having specific pore size. Membrane technologies encompass the construction of membrane modules and membrane fabrication. According to the pore size of the separation membrane, the most interest membrane technologies can be roughly divided into microfiltration (MF), ultrafiltration (UF), nanofiltration (NF), reverse osmosis (RO) and forward osmosis (FO) technology (**Table 1.1**). The MF technology can reject microorganisms or solid particle with a particle size of around 0.1-10 μm. UF technology can reject particles with a particle size between 10-100 nm, such as high molecular polymers, proteins, polysaccharides and other macromolecules. NF technology can achieve the screening of monovalent and divalent salt ions. In RO technology, all substances except water molecules can be rejected including the monovalent salts. In addition to the above-mentioned pressure-driven membrane technologies, the FO technology uses the osmotic pressure difference of solutions on both sides of the membrane as the driving force to realize the spontaneous transport of water molecules across the membrane. There are many types of membrane separation technologies. Appropriate separation and purification solutions can be selected according to actual needs and application scenarios, which greatly improves the recycling efficiency of water or solvent resources, and brings convenience to production and life. At the same time, as the complexity of the application system increases, more and more problems are highlighted in practical applications, such as membrane fouling, membrane material solvent tolerance and other issues. Therefore,

membrane separation technology puts forward higher requirements for membranes.

Table 1.1. Types of membrane technologies [12].

	Microfiltration	*Ultrafiltration*	*Nanofiltration*	*Reverse osmosis*
Pore size (nm)	50–10 000	1–100	~2	<2
Water permeability ($l\,m^{-2}\,h^{-1}\,bar^{-1}$)	>500	20–500	5–50	0.5–10
Operating pressure (bar)	0.1–2.0	1.0–5.0	2.0–10	10–100
MWCO (Da)	Not applicable	1000–300 000	>100	>10
Targeted contaminants in water	Bacteria, algae, suspended solids, turbidity	Bacteria, virus, colloids, macromolecules	Di- and multivalent ions, natural organic matter, small organic molecules	Dissolved ions, small molecules
Membrane materials	Polymeric, inorganic	Polymeric, some inorganic	Thin-film composite polyamide, cellulose acetate, other materials (Schafer *et al.*, 2005)	Thin-film composite polyamide, cellulose acetate

Membrane pore structure is one of the most important properties of a membrane, as it largely determines the selectivity as well as the permeability of a membrane. According to the uniformity of membrane structure, the membrane can be roughly divided into symmetric, asymmetric and composite membrane as shown in **Figure 1.1** [9]. For the symmetric membranes, it is fabricated by using one material through phase inversion, particle stretching and dry-stretching [14, 15], and electrospinning [16, 17]. The pore diameters do not vary over the entire cross section of the membrane, and the membrane flux is mainly determined by the thickness of the membrane [12]. Most of the MF and some of the UF membranes are symmetric-structured and have a relatively wide pore size distribution (PSD). However, this wide PSD has significant disadvantage of greater sensitivity to fouling because the largest pores initially take a disproportionate flux (flow $\propto d_{pore}^4$) making them susceptible to blocking [18]. Therefore, membrane scientists come up with the asymmetric membrane structure to shrink the pore size and obtain an isoporosity of membrane pores. The integrally skinned asymmetric (ISA) (also termed as asymmetric membranes) membranes are also composed of the same polymer but possess an asymmetric structure where the skin layer is present on top of the membrane. Most of the UF membranes and some loose NF membranes are asymmetric membranes which can also be fabricated through phase inversion method and have a much smaller pore size [19, 20]. To further enhance the flexibility on membrane structure tailoring to enhance the performance, composite

membranes were developed which contain a substrate layer and selective layer. Normally, composite membranes are made in a two-step process: (1) fabricating a microporous substrate and (2) depositing/casting a barrier/selective layer on the surface of the microporous substrate layer. This approach offers great flexibility for selecting different materials to tailor the membrane structure and properties, and greatly bring the membrane performance to the level that other symmetric and asymmetric membrane ever reached before.

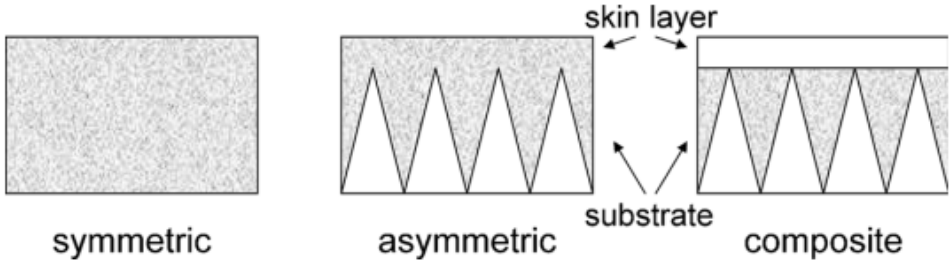

Figure 1.1. Types of membrane according to membrane structure [9].

Since the fabrication of selective layer can be quite flexible, this composite membrane structure has become a huge advantage for the membrane which requires a dense structure and high rejection rate, such as NF and RO membrane. Because of the higher density of the top selective layer, the membrane's flux and selectivity are determined by this layer, while the porous sublayer has little impact on the membrane separation properties. There is an obvious trend that thinner and denser selective layer can ensure a higher membrane performance, and therefore a new concept of thin-film composite (TFC) membrane occurred. Numbers of methods, such as dip-coating, spin-coating, casting a diluted volatile solution containing a polymer on the substrate [21], and interfacial polymerization (IP), have been developed to fabricate this thin selective layer with a thickness lower than 1 μm. Among them, the method of IP has achieved a great success in fabricating a polyamide (PA) selective layer for TFC membrane. Due to the standard fabrication routine, easy amplification and high separation efficiency, the TFC PA membranes have become one of the most widely used membrane for separation in various scenarios including aqueous and non-aqueous application, which are also the main research target of this study.

1.3. Overview of thin-film composite polyamide membranes

Membrane technologies can acquire increasing popularity and widespread application, which is inseparable from the development and preparation of high-performance separation membranes. Since 1965, Morgan proposed the first concept of using interfacial polycondensation reaction to prepare highly cross-linked and ultrathin polymer films [22, 23], the IP-prepared TFC PA membranes have been considered as one of the most important breakthroughs over the past decades. In this section, an overview of TFC PA membranes (hereinafter referred to TFC membrane) is given from the perspective of their unique structures and versatile applications. Later, unremitting endeavors on improving the TFC membrane performances are elaborately discussed in the following.

1.3.1. Structure of TFC membranes

Typical TFC membranes have an asymmetric structure and compose of a porous substrate layer and a dense PA selective layer which is prepared via IP, as shown in **Figure 1.2**. The IP technique begins with impregnating a microporous support membrane with an aqueous solution of a reactive diamine monomer such as m-phenylenediamine (MPD). Then, the porous sublayer membrane charged with the monomer is immersed into a water-immiscible organic solution containing a second reactive monomer such as a di/tri-acid chloride (e.g., trimesoyl chloride (TMC)). The polymerization of these two monomers occurs at the interface of two immiscible solvents and is diffusion-limited due to the high reactivity of the monomers. This interfacial reaction leads to the rapid formation of a highly cross-linked thin film layer that remains attached to the substrate matrix. The fabricated PA film with excellent solvents and acid/alkali-tolerance and heat-resistance is the core part of the TFC membrane [24], which largely determines the perm-selectivity of the TFC membrane. The PA layer does not appear any visible pores under an electron microscope, and is believed to be nonporous material which relies on solution-diffusion, steric hindrance or Donnan effect to achieve the selective penetration of molecules [25, 26]. It is

precisely because of the decisive role of PA layer that many studies are devoted to regulating the TFC membrane performance through modifying the PA layer (see Section 1.4.1 for more detailed discussion). For example, for the TFC membranes used in RO or FO applications, TMC is generally used as the oil-phase monomer, and MPD is used as the water-phase monomer. The resulting PA usually exhibits a large specific surface area with high cross-linking degree which ensures a high rejection rate for monovalent salts. For TFC membranes used in NF applications, selectivity is the key indicator to evaluate a NF membrane performance. Therefore, piperazine (PIP) is generally used as the water-phase monomer to prepare a PA layer with smooth surface feature and lower cross-linking degree. The prepared TFC NF membranes have excellent selectivity towards divalent salts or macromolecules.

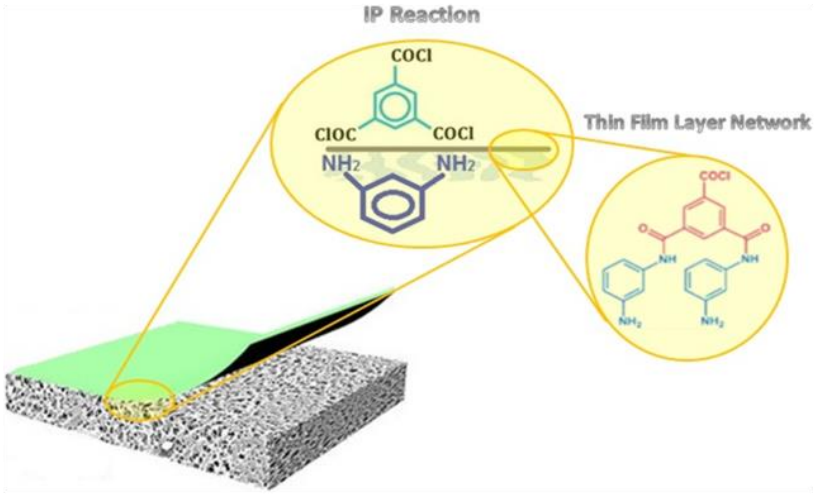

Figure 1.2. Schematic diagram of a typical TFC membrane formed using IP method between MPD and TMC monomers [14].

The porous substrate layer of TFC membrane is generally MF or UF membranes prepared using polysulfone (PSF) [27], polyethersulfone (PES) [28, 29], poly acrylonitrile (PAN) [30], polyimide (PI) [31], or other kinds of inorganic materials [32]. For a very long time, these substrate layers were believed to solely provide good mechanical integrity and low mass transfer resistance to the TFC membranes. However, studies have shown that the surface properties of substrate layer, such as hydrophilicity, roughness and porosity, also affect the PA formation to a large extent [33, 34]. For

example, Ghosh [35] et al. studied the effects of pore size, porosity and hydrophilicity of the substrate on the PA formation. Their study found that the hydrophilic substrate membrane could lower the diffusion rate of IP monomer through forming hydrogen bonds, resulting in a PA layer with low cross-linking degree and poor selectivity. However, having a certain degree of hydrophilicity to the substrate is necessary for an integral PA generation, because it ensures a more uniform distribution and adsorption of IP monomer during IP reaction. Not only hydrophilicity, other properties such as porosity and pore size also play a role in affecting the IP reaction [34]. These pioneer works have successfully drawn peoples' attention to the importance of substrate membrane, and give inspirations to versatile solutions for improving the TFC membrane performances (see Section 1.4.2 for more discussion).

1.3.2. Classic transport and rejection mechanisms in TFC membranes

The mass transport in the dense, nonporous PA film of TFC membranes is governed by the solution-diffusion model [36]. Taking aqueous application as an example, water and solute molecules first dissolve into the PA layer, then diffuse through the PA matrix under chemical potential gradient, and then desorb into the permeate side. The separation of fresh water from saline water is achieved because of the difference in the permeabilities of water and solutes in polymer matrix. The water flux, J_w, is described as

$$J_w = A(\Delta P - \Delta\pi)$$

where A is the water permeability coefficient (or permeance), and ΔP and $\Delta\pi$ are the applied pressure and osmotic pressure differences across the PA layer, respectively. Similarly, the solute flux, J_s, is expressed by

$$J_s = B\Delta C$$

where B is the solute permeability coefficient and ΔC is the concentration difference across the PA layer.

For a given membrane, the water and solute permeability coefficients of the active layer are determined by the intrinsic water permeability (P_w) and solute permeability (P_s), respectively:

$$A = \frac{P_w V_w}{\delta_m R_g T}$$

$$B = \frac{P_s}{\delta_m}$$

where V_w is the molar volume of water, δ_m is the film thickness, R_g is the ideal gas constant, and T is the absolute temperature.

When plotting water-solute selectivity (P_w/P_s) *versus* water permeability (P_w) in **Figure 1.3a**, performance data of existing TFC membranes are mostly confined in the blue-box region, wherein the highest selectivity for a given permeability approaches the solid line. This line represents the trade-off relationship between permeability and selectivity, which is widely observed in membrane processes using synthetic polymer materials [25]. Ideal membranes are expected to have high values of both water permeability and water-salt perm-selectivity (i.e., the red-box region in **Figure 1.3a**). Nevertheless, such a combination is difficult to achieve, as most material properties that affect water permeability would in turn exert similar effects on solute permeability.

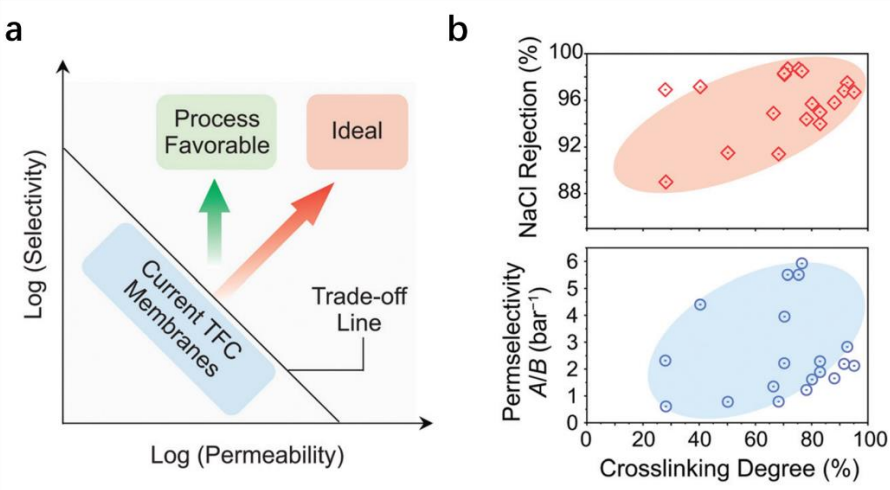

Figure 1.3. (a) Permeability-selectivity trade-off relationship for TFC PA desalination membranes; (b) Correlation of crosslinking degree with salt rejection and perm-selectivity of TFC membranes [36].

The permeability differences of water and solutes (water-solutes selectivity) in TFC PA membranes is determined by the combined mechanisms of steric hindrance, Donnan exclusion, and dielectric effect [26]. The steric hindrance is related to the pore size (or

free volume) of PA, which allows molecules with smaller sizes to permeate while keeping larger ones from doing so. The Donnan exclusion is governed by the fixed charge density on the membrane surface. For example, a negatively charged surface effectively rejects anions (e.g., SO_4^{2-}). To maintain electroneutrality on both sides of the membranes, cations (e.g., Na^+) are therefore also excluded by the membrane, leading to a good overall rejection of salts (e.g., Na_2SO_4). The dielectric effect is related to an energetic penalty that solutes have to pay while transferring from a solvent with a high dielectric constant (i.e., water) to a medium with a low dielectric constant (i.e., polymer membrane material). The presence of such an energetic penalty thus hampers the diffusion of solutes (e.g., salt ions) through the membrane [26].

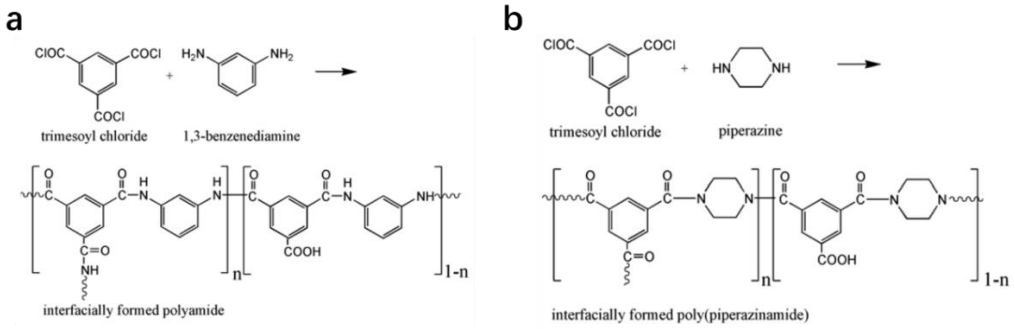

Figure 1.4. (a) Fully aromatic polyamide based on TMC and MPD; (b) Semi-aromatic polyamide based on TMC and PIP. The symbol *n* denotes the degree of crosslinking (*n* has value in between 0-1; n=1 for fully cross-linked polyamide and n=0 for fully linear one) [37].

The three solute rejection mechanisms discussed above are relevant to the material characteristics of the selective layer, which stems from the molecular structure of the PA materials. Taking cross-linking degree as an example, the PA forms a fully crosslinked structure (i.e., the "n" segment in **Figure 1.4**) with a monomer ratio of 3:2 for MPD to TMC. In an actual IP process, some linear segments (i.e., the "1-n" segment in **Figure 1.4**) would also form under a monomer ratio of 1:1 for MPD to TMC. In this case, unreacted acyl chloride groups undergo hydrolysis to form carboxylic groups, thereby imparting a negative charge to the membrane surface. The crosslinked segments

more rigidly resist swelling due to the presence of chain linkages between polyamide backbones, thus impeding solute transport. In contrast, the linear segments are likely to undergo more severe swelling, which facilitates solute transport within the polymer matrix. As shown in **Figure 1.3b**, both NaCl rejection and perm-selectivity exhibit an overall good correlation with the crosslinking density, implying that increasing crosslinking segments is a feasible strategy toward the design of membrane with high water-salt selectivity. Noted that this is only one example of how material characteristics determine membrane transport properties. Efforts to elucidate the structure-property-performance relationship of the PA selective layer will be of paramount importance in guiding the future design of high-performance TFC membranes.

1.4. Applications of TFC PA membranes

1.4.1. Aqueous separations

At first, the TFC membrane is mainly used in water treatment because these membranes were developed as a follow-up to the phase inversion asymmetric membranes to meet demand in the growing desalination industry in the 80's [38]. The first commercialized IP-made TFC membrane was disclosed by Cadotte in 1985 [39, 40]. The RO membranes produced by this technique exhibited a dramatically improved salt rejections performance and permeances in comparison to ISA membranes [41]. Today, most of the RO desalination plants use fully aromatic TFC membranes. The technology has further witnessed different membrane modules such as spiral wound, tubular and hollow fiber to enhance the separation with higher energy efficiency [12]. After decades of bursting development of TFC membrane in both scientific researches and commercialization, membrane manufactures are able to design the membrane for specific scenarios including seawater (SW) desalinations, brackish water (BW) desalinations, wastewater reuse, ultra-pure production for semiconductor, home-use water purifier, etc [9] (**Table 1.2**). For example, targeting to remove the trace contaminants of boron in seawater while maintaining a high seawater desalination

efficiency, the membrane manufacturer Toray recently released a fully cross-linked aromatic TFC membrane for SWRO coded TM820R. This membrane exhibited a water productivity of 35.6 m^3/day with 99.8% of total dissolved solid (TDS) rejection, and 95% of boron rejection which is a breakthrough among commercial SWRO membranes [42, 43]. For the BWRO, because of the much less salinity (1,500-10,000 mg/L) in BW than SW (average salinity of 35,000 mg/L), the operating condition for BWRO can be quite gentle than the SWRO system, which indicates the BWRO TFC membranes can be re-designed to adapt the BWRO system with high economic efficiency [44-47]. Some of the commercial BWRO membranes including BW30-365 from Dow™ Filmtec, BWRO TM720-370 from Toray Standard and ESPA3 from Nitto/Hydranautics, etc, have received great successes in dealing with the BW in real application [45].

Table 1.2. Commercial SWRO membrane material and configuration [43].

Company	Membrane/ Element	Chemical Formula	Product in 2020	Data Re-sources
Dupont	B-10 -Asymmetric hollowfiber-		✕	1
	A-15 -Composite spiral-		✕	2
FilmTec/ Dow/Dupont Water Solutions	FT-30 -Composite spiral-	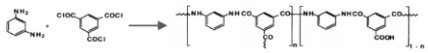	○	2
Toyobo	HOLLOSEP -Asymmetric hollowfiber-	CTA 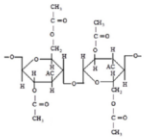	○	3
Toray	PEC-1000 -Composite spiral-	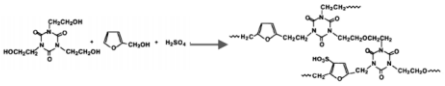	✕	2
	UTC-80 -Composite spiral-	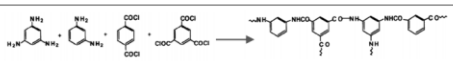	○	2
Nitto Hydranautics	-Composite spiral-	Similar to FT-30	○	-
LG Chem	-Composite spiral-	Similar to FT-30	○	-

Data Resources:
1. USP 3567632A
2. Peterson, R. J. Journal of Membrane Science,83(1993)81-150,Elsevier Science Publishers B. B:Amsterdam.
3. Takahito Nakao, Yuki Miura, Kenji Furuichi and Masahiro Yasukawa, *Membranes* **2021**, *11*, 183. https://doi.org/10.3390/membranes11030183.

Note: Product in 2020 ○: Available ✕: Unavailable.

Different from the RO membranes which in principle require a high retention for all substances except water, the NF membranes lay more emphasis on selectivity. Thus, the TFC PA membranes used in NF application are more flexible in pore size and

selectivity which is a contribution of unique separation mechanism of NF membrane. Unlike the separation of TFC RO membrane is mainly governed by steric hindrance or size sieving (high density of selective layer to maintain a high retention for all molecules except water), the Donnan exclusion, which is a contribution of surface charge, plays a crucial role the separation using NF membranes. As discussed in previous section, the regulations of cross-linking degree and surface charges can be quite flexible though changing the ratio and species of IP monomer, which means the TFC membranes can meet the qualification for NF application through adjusting the properties of PA layer. Currently, several membrane manufacturers in the world have launched their TFC NF membrane products, such as NF 45 from Dow/Film Tec, NTR 7450 from Nitto–Denko and UTC 20 form Toray Ind. Followed by the optimization of membrane configuration, these membrane products have been widely used in BW desalinations [48], mono-/di-valent ion separation [49], textile dye wastewater treatment [50] and other wastewater treatments.

1.4.2. Non-aqueous separations

Since the TFC membrane reached a huge success in aqueous applications, researchers start to exploit the feasibility of TFC membrane as an alternative of ISA membrane to use in non-aqueous separation such as solvent-solute separation or solvent-solvent separation. However, the application of TFC membrane in organic system lags behind at the beginning mainly owing to the poor solvent stability of conventional polymer substrate layer. Nevertheless, emerging solvent-resistant materials, such as polyimide (PI) [51-53], polyacrylonitrile (PAN) [54], polyvinylidene difluoride (PVDF) [55, 56], polytetrafluoroethylene (PTFE) [57, 58] and polyketone (PK) [59-61], etc., have been developed and utilized as substrate layer for TFC membranes, making the TFC membranes show great potential in non-aqueous application. One of the representative for non-aqueous separation is organic solvent nanofiltration (OSN) process, which uses external pressure as the driving force and allows to separate molecules with molecular weight around 200-1000 g/mol from organic solvents [62]. A pioneer work of OSN using TFC membrane was done by

Livingston and co-workers [31] where they prepared an ultrathin PA selective layer through controlled IP method to use for separating dyes from organic solvents. Due to the ultrathin PA layer thickness down to sub-10 nanometer, the TFC membrane with crumple micro-texture exhibited the excellent separation performance with methanol permeance up to 52 L m^{-2} h^{-1} bar^{-1}, and rejection of dye molecule methyl orange (MO, 327.3 g/mol) up to 98.9%.

Another attempt of TFC membrane for non-aqueous separation is the solvent-solvent separation which is commonly represented by the organic solvent reverse osmosis (OSRO) process. In sharp contrast to OSN (solvent-solute) separation with distinct difference in size, the OSRO (solvent-solvent) separation places much greater demands on the structural regulation of membranes since the size difference of different solvents is very small. Shortly after cellulose acetate (CA) membranes were first used in water RO [63], attempts were taken to use this membrane to separate alcohol/hydrocarbon mixtures [64, 65]. Later, membranes made from polyacrylonitrile (PAN) [66], cellulose acetate butyrate (CAB) [67], polyethylene (PE) [68], perfluorodioxole copolymer [69-71], silica-zirconia [72], organosilica [73], polyamide-imide Torlon® [74], polydimethylsiloxane (PDMS) [75], and metal oxides/polymer of intrinsic microporosity 1 (AlO_x/PIM-1) [76] were developed. However, these membranes still suffer from insufficient separation performance or large-scale fabrication. Recently, with using of solvent-resistant materials as substrate, the TFC membranes have shown the potential in the OSRO process [61, 77, 78]. Liu et al. [61] reported a polyketone (PK)-based TFC PA membrane used in OSRO process for separating aliphatic alcohols, aliphatic alkanes, and aromatic compounds from methanol. Superior separation performances and long-term stability were achieved for methanol/toluene (9:1, weight percent) mixture with separation factor of 8.4 under operation pressure of 3 MPa. It is noteworthy that the permeance of the PK TFC membrane was 0.17 L m^{-2} h^{-1}/bar, much higher compared to the permeance of the organosilica membrane (0.01 L $m^{-2}h^{-1}$/bar). This significant enhancement demonstrated the contribution of thin, dense, and crumpled structure of the PA separation layer.

Over the past decades, the TFC membranes have fully proven their excellent

performance in both aqueous and non-aqueous separation. However, the TFC membranes are still in their infancy. Those brilliant research works give an impressive start on understanding not only the transport mechanism in PA layer, but also the structure-performance relationship, which open up a new prospect on pursuing modifications to improve the TFC membrane performances in both aqueous and non-aqueous applications.

1.5. Performance optimization of TFC PA membranes

Given that the wide use of TFC membranes in both aqueous and non-aqueous application, extensive works have been done to improve the TFC membrane performances for different purposes, such as high separation performances, antifouling and chlorine-resistance in water RO process. However, regardless of the applications and purposes, modifications for TFC membranes can be essentially sorted from three aspects: modification of PA selective layer, modification of substrate layer and structure design: interlayer.

1.5.1. Modification of PA selective layer

Modifying the PA selective layer is, potentially, a direct strategy for fabricating a high-performance TFC membrane, and this strategy has been a topic of interest for quite some time. The PA modification roughly includes two ways: the bulk modification (e.g., introducing new IP monomers and embedding nanofillers/additives) and surface modification (e.g., grafting and coating after IP).

Regardless for aqueous or non-aqueous applications, the objectives of introducing new IP monomers, nanofillers or additives, in essence, are to increase the transport channel and to regulate the PA properties. New monomers can regulate the PA chain structure on a molecular level through forming amide bond in the IP reaction. The monomers can be either amino functionalized or acyl chloride functionalized, differential in reactive activity and targeting dissolving phase. Compared to acyl chloride functionalized monomers which are highly reactive and easy to hydrolyze [79], the amine functionalized monomers are more developed because of the easy synthesis

and chemical stability. Planar molecules are initially used as co-/sole monomer to synthesize PA films with different cross-linking structures which highly correlate to separation performances. Jin et al. [80] reported a TFC NF membrane fabricated using 2,2'-oxybis-ethylamine (2,2'-OEL) as the co-monomer with PIP. The prepared TFC membranes had a high flux at 35.6 $L^{-1}m^{-2}/h$ despite the salt rejection slightly decreased (**Figure 1.5**).

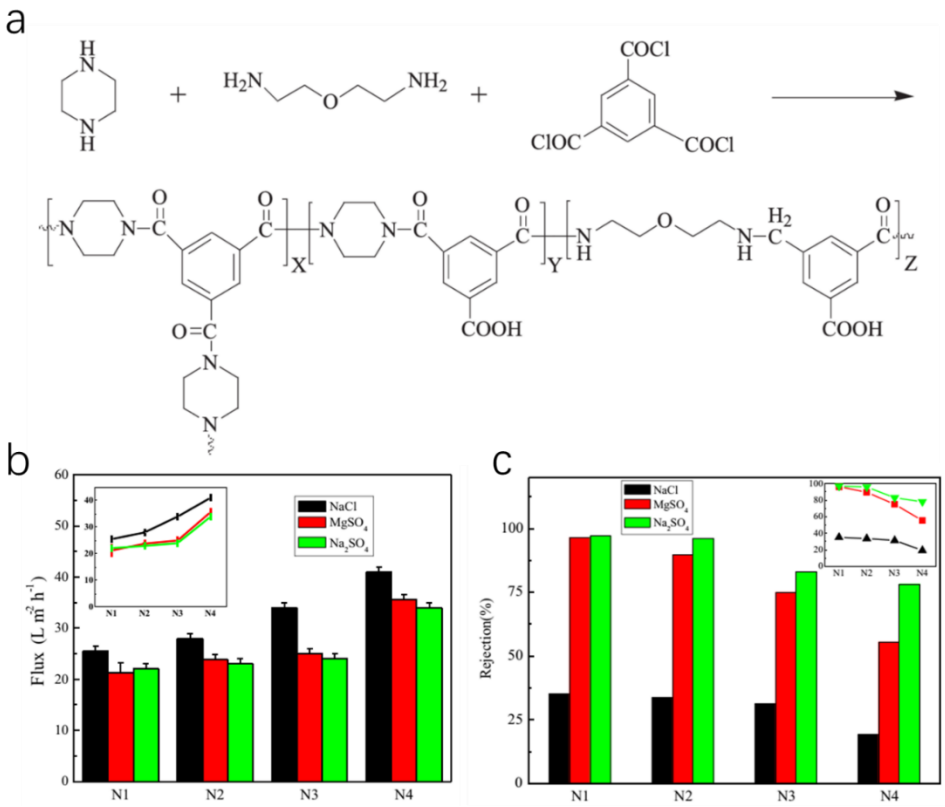

Figure 1.5. (a) IP reaction using 2,2'-OEL and PIP as monomers; Flux (b) and rejection (c) of TFC membranes with different 2,2'-OEL blending [80].

Generally, incorporating new IP monomers often leads to a decrease on cross-linking degree of PA, further resulting in increased permeances but compromised rejections. However, this rejection compromise can be tolerated depending on the substances have to be rejected. Novel monomers having specific functional groups, such as zwitterion [81-83] and fluorine [78, 84], were further designed to provide additional contributions on regulating the surface properties of PA, since performances such as antifouling or solvent separation are surface charge-dependent or polarity-dependent [71]. Kushida et

al. [78] regulated the polarity of PA layer with using fluorine-content molecules (5-Trifluoro-1,3-phenylenediamine (TFMPD)) as the IP monomer to reach with TMC (**Figure 1.6**). Due to the fluorine element, the PA layer turned to less polar and allowed the permeation of nonpolar solvents, such as aliphatic and aromatic hydrocarbons, which could not permeate through the conventional hydrophilic polyamide membranes using MPD as a diamine monomer. The membrane was used to separate toluene from toluene-containing solvent mixtures, with selective permeation of toluene and 93.9% rejection of 1,3,5-triisopropylbenzene (TIPB).

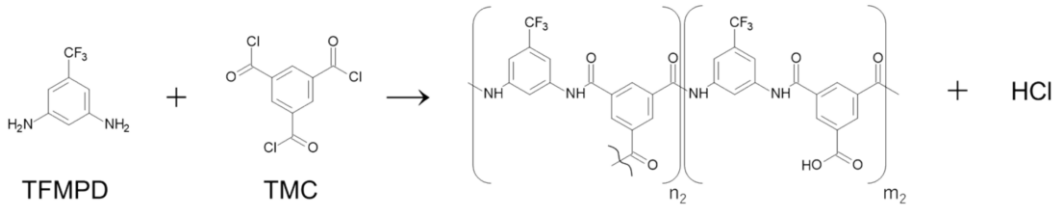

Figure 1.6. IP reaction of TFMPD and TMC [78].

As investigations on understanding the free volume of selective layer going far, molecules with non-planar structure or intrinsic cavity, such as 3D dendritic poly(amidoamine) [85], contorted phenol and naphthol [51, 53, 86], acyl chloride-functionalized triptycene [79, 87], amine-functionalized porphyrins [88], pillar arene [52, 89], cyclodextrin (CD) or amino-cyclodextrin [90-93] and molecular water-wheel Noria [94-96], were applied as IP monomers to fabricate a selective layer with abundant interconnected micropores and high microporosity. Taking the advantage of 1,1'-Bi-2-naphthol (BINOL) with unique contorted configuration with a rotatable axis linking two rigid naphthyl rings, Fu et al. [53] successfully synthesized a polyarylate (PAR) selective layer using a tetrafunctional BINOL-based monomer 7,7'-dihydroxy-2,2'-binaphthol (7,7'-OH-BINOL) with a rotatable highly kinked unit, as the sole aqueous monomer to react with TMC. The unique molecular structure endows the membrane with ultrahigh fractional free volume (FFV) of 21%, and exhibits very high solvent permeability when applying in OSN application. Xiong et al. [93] reported a ethylenediamine (EDA)-functionalized β-cyclodextrin (β-CD) to be used as the IP

monomer to synthesize a selective layer with intrinsic CD cavity (**Figure 1.7**). This TFC membrane was tested in NF application, and showed water permeance of 13.5 $Lm^{-2}h^{-1}$/bar and high rejections to common salts (e.g., Na_2SO_4, $MgSO_4$) because of the pore size exclusion effect of *β*-CD and the negative charge of the membrane.

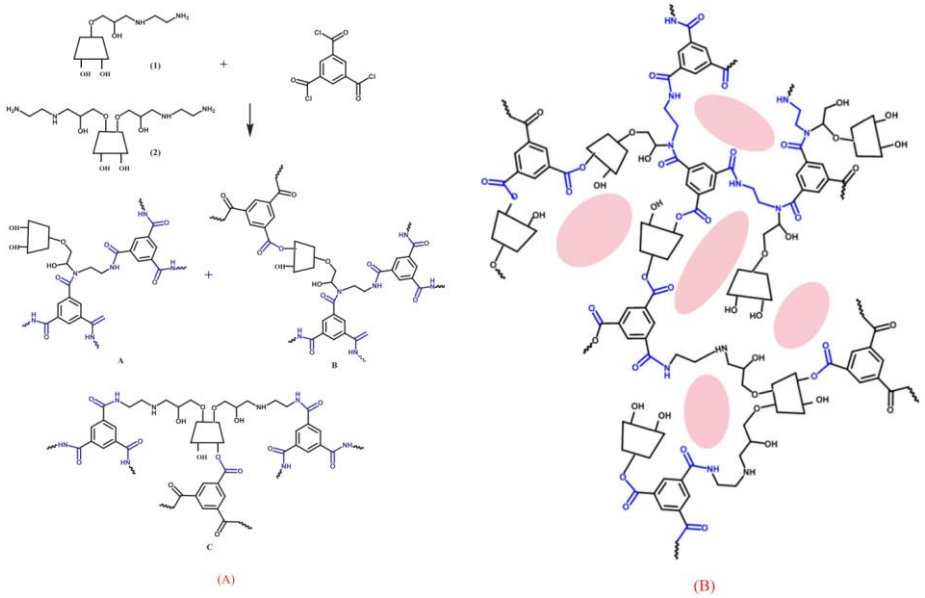

Figure 1.7. (A) Reaction scheme of the interfacial polymerization between *β*-CD-EDA and TMC (B) possible pore structures in the selective layer of TFC_*β*-CD-EDA membrane [93].

Aside from using new IP monomers, blending nanofillers or additives into aqueous or organic IP phase can also be used to modified the PA layer. However, nanofillers often encounter bad compatibility with material body and easy agglomeration [97]. To fix this problem, functionalized nanofillers were synthesized to better combine with the material through chemical bonding. The most commonly used nanofillers include graphene quantum dots (GQDs) [98], graphene oxide (GO) nanosheets [99] and metal organic frameworks (MOF) nanoparticles [100]. With the help of nanofillers, enhanced membrane permeances could be achieved with slightly compromise on rejection. Thus, such nanofiller modifications are often reported for TFC NF or OSN membranes as less density of the selective layer is acceptable. Additives such as surfactant (e.g., Sodium dodecyl sulfate (SDS) [101]) and zwitterionic molecules (e.g., 1,3-propanesultone (1,3-

PS) [102]) can regulate the PA formation through affecting the IP monomer diffusion. For example, Zhang et al. [102] used 1,3-PS as the additive to blend into the organic IP phase. The 1,3-PS molecules can interact with MPD by hydrogen bond and hinder MPD diffusing farther from the interface, further causing a mild and uniform reaction process. Thinner multilayer PA structure can be formed via a mild and uniform interfacial polymerization process, achieving larger surface area, which is responsible for the improved water flux.

Due to the self-limitation of IP reaction and the multi-functionalities of IP monomer, active sites could be generated and remained on the PA surfaces. These active sites can be the unreacted acyl chloride groups from organic phase monomers, carboxyl groups hydrolyzed from acid chloride monomer, and the amide bond or amine groups in PA molecular chain, which provide abundant surface grafting or coating modification feasibilities. Moreover, compared with the introduction of new IP monomer, the surface modification has less impact on the cross-linking structure of PA, as the process are often conducted on an already-formed PA layer. The grafting method is more stable than the coating method since there are chemical bonds connected between molecules and the PA molecular chain. The grafting molecules can be specifically designed to impart the selective layer with desired surface properties such as hydrophilicity, polarity and chargeability [103]. For instance, hydrophilicity and neutral-charged property are matters when antifouling property is desired for the membrane used in water treatment. With this requirement, a great interest of grafting zwitterionic molecules onto the PA surface is catching attention due to the superior hydration capacity and electrostatic interaction shielding effect of zwitterionic molecules [104]. Aside from grafting or coating small molecules such as zwitterion [105, 106], polymers having linear or branched structure such as polyvinyl alcohol (PVA) [107, 108], poly(methacrylic acid) (PMA) [109, 110], polydopamine (PDA) [111-113], polyethylene glycol (PEG) [114-116], hyperbranched polyethyleneimine (PEI) [117, 118], hyperbranched poly(amine ester) (PAE) [119], hyperbranched polyglycerol (hPG) [120] and poly(amidoamine) (PAMAM) [121, 122], have also been applied to surface grafting or coating.

1.5.2. Modification of substrate layer

The formation of PA layer is significantly controlled by the diffusion rate of diamine monomer from the substrate pores to the organic phase. Thus, the growth of the PA layer is generally known as a self-limiting diffusion-controlled process [23, 123]. Considering the IP reaction take places *in-situ* on the surface of substrate, that gives the fact that the substrate inevitably plays a non-negligible role in the TFC membrane performance and PA formation. Prominent research works have given profound investigations on the substrate properties functioning in shaping the PA layer and membrane performances from the perspective of, for instance, hydrophilicity and pore size.

The IP monomers in aqueous phase tend to absorb more on the substrate with hydrophilic surface and large pore size, which could result in a retarded release of aqueous monomer when triggering the IP reaction. In addition to influencing the absorption and distribution of IP monomer, the pore size is also highly related to the PA intrusion which show a great relation to the transport resistance of the TFC membrane [124]. In the light of the above, strategies such as hydrophilic modification or pore size tailoring were applied to the modification of substrate layer to further influence the PA formation [125].

The commonly used hydrophilic modifications for substrate layer include plasma treatment, surface grating and coating, additive blending. The plasma treatment gained popularity for the hydrophilic modification, as it can generate oxygenated hydrophilic moieties with little affecting the pore size and porosity. This method has been proved to be prominent in enhancing the hydrophilicity of substrate made by polyvinylidene fluoride (PVDF) [126], polypropylene (PP) [127, 128], polyethylene (PE) [129] and etc. For example, Park [129] et al. reported a TFC PA membrane fabricated using a plasma-treated PE membrane as the substrate layer. The water contact angle (WCA) of PE membrane can be dramatically reduced from ~120° to ~43° by increasing the plasma exposure time. The optimal TFC membrane prepared using a PE substrate with a WCA of 75° exhibited~30% higher water flux than a commercial RO membrane. Similar with

the surface grafting and coating modification of PA layer, these ingenious surface modifications are also applicable for substrate layer. Materials such as polydopamine (PDA), polyethylene glycol (PEG), zwitterionic molecules were induced onto the substrate surface to control the IP monomer release, further forming a PA layer with different properties [130].

Different from the surface modification only giving a difference in hydrophilicity on substrate surface, blending additives into substrate matrix is another way to tailor the hydrophilicity integrally. Due to the additive blending occurring before the membrane fabrication, such as nonsolvent-induced phase separation (NIPS) process, this method is sometime accompanied by changes in membrane structure and pore size. However, the overall hydrophilicity can not only influence the storage and release of IP monomer during PA formation, but also has an effect on reducing the transport resistance when molecules passing through the membrane. This is particularly important to reduce the internal concentration polarization (ICP) phenomenon of the forward osmosis membrane. Additives such as zwitterionic polymer, PEG and PDA are blended into the membrane matrix to improve the hydrophilicity of the substrate. Also, the additional functional groups induced by additives could interact with IP monomers by covalent bond, hydrogen bond and etc., further influencing the PA formation.

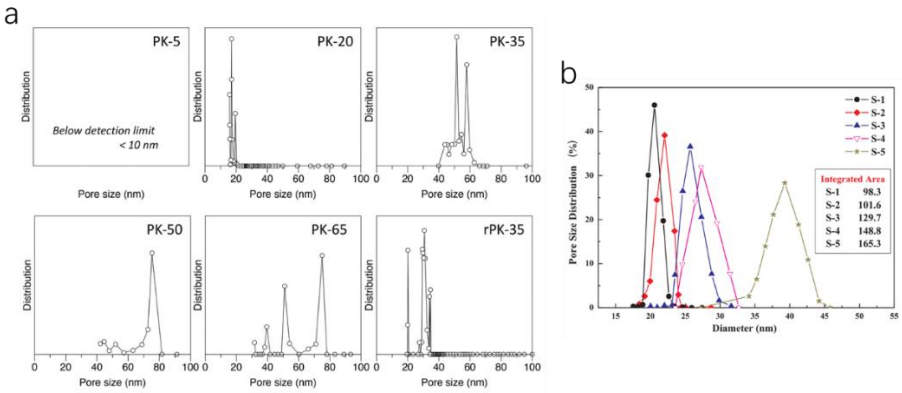

Figure 1.8. Pore size regulation of PK (a, number after sample name represents the methanol concentration in coagulation bath [131]) and PSF (b, numbers after sample number represent the PSF concentration in casting solution: 20 wt%, 18 wt%, 16 wt%, 14 wt% and 12 wt% correspond from S-1 to S-5).

For the pore size regulation, the commonly used method is tuning the pore size from the fabrication step, such as changing the fabrication condition. For example, Guan et al. [131] regulated the pore size of PK through changing the coagulation bath composition (**Figure 1.8a**), then compared the performance of corresponding TFC membranes in RO process. Yasukawa et al. [132] investigated the influence of PK substrate thickness on pore size and FO performance of resulting TFC membrane. Zhang et al. [133] studied the solid content of PSF substrate (**Figure 1.8b**) and the impact of support surface pore characteristics on the active layer formation process and the accordingly obtained active layer properties.

1.5.3. Structure design: Interlayer

Other than the modifications of PA layer and substrate layer mentioned here, a novel membrane structure design has gained interests among membrane communities to improve the TFC membrane performances. The traditional substrate membrane structure tailoring methods, such as adjusting the solid content, membrane thickness, and composition of the coagulation bath during the NIPS fabrication process allow control over pore size, surface morphology, and other membrane characteristics. However, problems also occur along with these methods. For example, decreasing membrane thickness and creating a denser structure may impact the mechanical strength and decrease permeance due to the increased mass transfer resistance.

To achieve a balance between structural integrity and performance, the interlayer intercalation strategy intrigues membrane scientists due to its less substrate-dependence. The interlayer intercalation has been demonstrated as an effective way to enhance the membrane performance from the perspectives of gutter layer effect [134-136], substrate surface property regulation [137, 138], IP reaction facilitation [58] and PA intrusion prohibition [138, 139]. Tang et al. did a series of work on proving the gutter layer effect of interlayer from both experimental and modeling [135, 136]. Separately, the interlayer is reported to act as a “storage” for the aqueous diamine monomer and facilitate the following interfacial polymerization process by controlling the release of IP monomer [59, 130, 140]. Shen et al. [130] introduced a PDA interlayer onto PES substrate, and

tested the MPD storage and release rate during the IP reaction (**Figure 1.9**). Results show that the PDA can help to adsorb more MPD molecules and restricted the MPD release when IP reaction occurred, resulting in a PA selective layer with ultrathin thickness of ~26 nm, which is a sharply decrease compared with conventional PA layer.

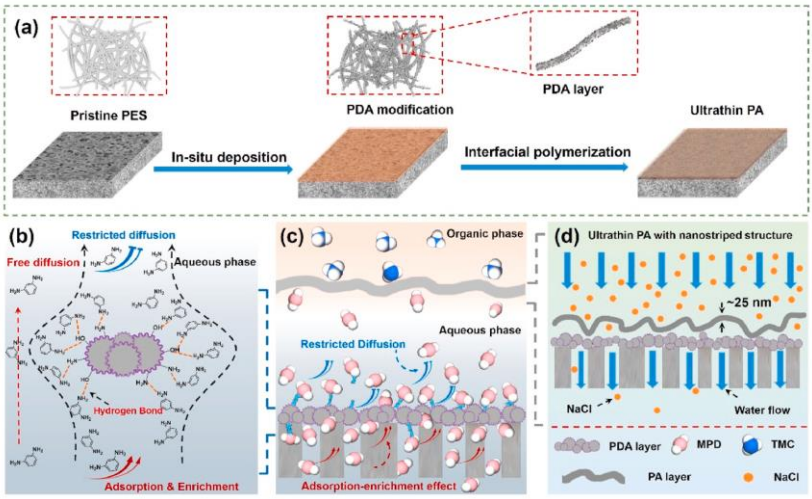

Figure 1.9. Schematic of the PDA decoration for an ultrathin and nanostriped PA membrane for high-performance RO [130].

Different from the blending method which always suffers from the agglomeration and compatibility problem, the interlayer working as an individual layer between selective layer and substrate layer can be less affected by these problems, providing substantial choices on interlayer materials. Upon the obvious significance of interlayer on membrane performances, abundant attempts were conducted with regards to different interlayer materials, which are detailly sorted in following section.

1.6. Kinds of interlayer materials

Membrane scientists have developed several materials that can be used to fabricate interlayers, such as three-dimensional (3D) nanoparticles (e.g., SiO_2 [141], zeolite [142], ZIF-8 [123, 143]), two-dimensional (2D) nanosheets or nanoplates (e.g., graphene oxide (GO) [144, 145], MXene [146]) and one-dimensional (1D) nanotubes or nanowires (e.g., carbon nanotubes (CNTs) [137, 138, 147, 148], cellulose nanocrystals (CNCs) [149-151]). The specific chemistry of each interlayer material can

bring different influences on the as-prepared TFC membrane performances [134].

1.6.1. Three-Dimensional nanoparticles

ZIF-8 is a common MOF material which consists of metal ions/clusters coordinately linked by organic ligands [152]. The microporous structure of ZIF-8 demonstrates the feasibility of using ZIF-8 as a material of separation material [153]. In Wang's work [154], a ZIF-8 interlayer were introduced between PA selective layer and PSF substrate layer. The as-prepared TFC membranes were optimized upon the thickness of ZIF-8 interlayer which can be controlled by changing the quantity of ZIF-8 in *in-situ* growth procedure. The optimal interlayered ZIF-8/PA membrane achieved high water flux up to 27.1 kg m^{-2} h^{-1} and dye rejection rate of 99.8%. Both the permeance and selectivity of interlayered membrane are higher than those of conventional PA/ZIF-8 TFN membrane, thanks to more ZIF-8 with fewer aggregates in the interlayer as well as the regulated PA structure. Other kinds of MOF nanoparticles such as MIL-101(Cr) [155], ZIF-93 and HKUST-1 [156] were also be used for constructing interlayer by Langmuir-Schaefer (LS) methodology and *in-situ* growth on substrate, respectively, which have been proved to be beneficial to the TFC PA membranes with improved performance for removing pharmaceutical compounds from both organic solvent and water.

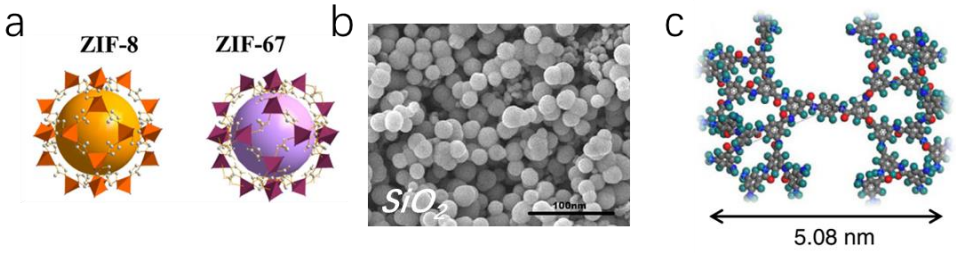

Figure 1.10. Some of 3D nanoparticles used to prepare interlayer. (a) ZIF-8&67 nanoparticles [143]; (b) SiO_2; (c) 32-amines terminated polyamide dendrimer.

Nanoparticles such as SiO_2 [141, 157], PDA [140], zeolite [142], polyamide dendrimer (PAMAM) [158] can also be used as interlayer materials (**Figure 1.10**). However, it should be aware that some interlayers of 3D nanoparticles are less uniform and even cannot be defined as a continuous layer due to steric configurations. Despite

this, researchers still distinguish them as interlayers because they are separately introduced or *in-situ* growth.

1.6.2. Two-Dimensional nanosheets

To prepare a true layer structure, researchers turn to using 2D nanomaterials to prepare the interlayer (**Figure 1.11**). The graphene oxide (GO) nanosheets have been widely studied as the right material to make novel separation membranes via layer-stacking techniques, due to their great flexibility of controlling the spacing [159, 160]. The features of high-aspect-ratio geometry and easy stacking to form a continuous and uniform layer make GO a possible candidate as interlayer materials [144, 161, 162]. However, the swelling and unstable problem in liquid environment limit the use of pure GO nanosheets as the interlayer [163, 164]. Regarding the concern about stability, modification of GO nanosheets should be conducted prior to formation of a GO interlayer. Li et al. [165] crosslinked the GO nanosheets using ethylenediamine (EDA) before preparing the GO interlayer. The crosslinked GO interlayer was quite stable in solvent environment, and the optimized PA layer showed ultralow average roughness (only about 2 nm) and ultrathin average thickness (about 15 nm). The membrane exhibited a high rejection rate of >98% for rhodamine B after immersing in pure N, N-Dimethylformamide (DMF) at 80 °C for more than 160 days. Other GO modification such as PDA [161] can also improve the stability of GO nanosheets when preparing the interlayer.

As another type of 2D nanosheets, MXene has properties such as a large surface area, abundant nanochannels, hydrophilicity, and a good mechanical property [166, 167]. Recently, the MXene membrane have shown its great potential in being apply to molecular separation [168, 169], making it becoming a promising material for interlayer fabrication. Wu et al. [146] deposited an interlayer of MXene nanosheets on a nylon substrate to carry out the IP reaction. The fabricated MXene-interlayered TFC FO membrane demonstrated simultaneously improved water flux and reduced reverse salt flux, which breaks the trade-off phenomenon between the permeability and selectivity of TFC membranes. Further, the optimized TFC membrane demonstrated its potential

for organic solvent recovery with high ethanol fluxes of 8.0 L m^{-2} h^{-1} in the active layer faces to feed solution (AL-FS) mode and 9.5 L m^{-2} h^{-1} in the active layer faces draw solution (AL-DS) mode with low reserve salt fluxes. Besides the cases of using pure MXene as interlayer, a combination of MXene with other nanomaterials such as CNT [170, 171] and CNC [149] were also a smart choice for preparing the interlayer from the perspective of controlling the layer spacing of MXene and providing multiple water transport path. The resultant interlayered TFC membranes were examined in both FO and NF application, and enhanced performances were demonstrated.

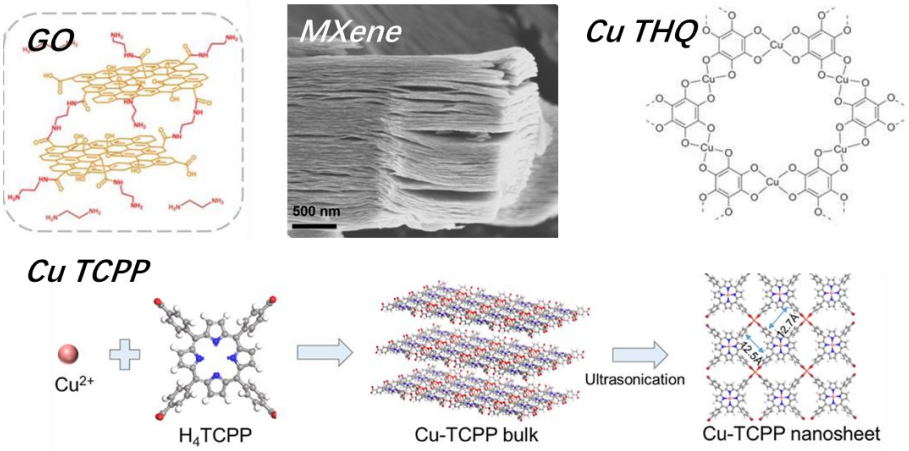

Figure 1.11. Some of 2D nanosheets used for preparing interlayer; GO [145], MXene [168], 2D MOF nanosheets Cu THQ [172] and Cu-TCPP [56].

The 2D MOF nanosheets such as Cu-TCPP is another good option for fabricating interlayer [55, 56], and the as-prepared MOF-interlayered TFC membrane exhibited excellent separation performance in OSN process. As researches on 2D interlayer deepening, problems with 2D interlayers become apparent, such as swelling, poor stability and high transfer resistance caused by tortuous transport pathway in such dense lamellar structures. The stability of the stacked layer is a common concern for the application of 2D membranes. Therefore, whether a TFC PA membrane with interlayer stacked by 2D nanosheets can exist stably between the substrate and PA layer is a crucial issue limiting its further application.

1.6.3. One-Dimensional nanotubes and nanowires

To deal with the problem of stability and transport resistance of 2D interlayers, the 1D nanotubes and nanowires were used as the interlayer materials as they have a high length-to-width aspect ratio (**Figure 1.12**), which is beneficial to form a porous network with less transport resistance in a 2D way. An earlier attempt on using 1D nanowires as an interlayer was released by Livingston et al. [31], where a $Cd(OH)_2$ nanostrand was introduced onto the substrate and served as a reservoir for the aqueous solution of MPD and controlled the release of MPD further to tailor the structure of PA layer.

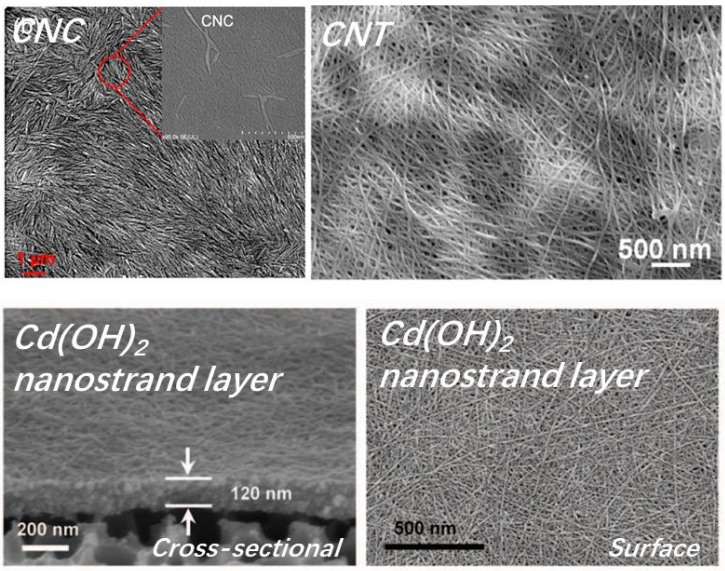

Figure 1.12. SEM images of interlayers prepared using different 1D nanotubes and nanowires of CNC [149], CNT [148] and $Cd(OH_2$ nanostrand [31].

Later, research works using carbon nanotubes (CNTs) [32, 58, 137-139, 148, 173, 174], cellulose nanocrystals (CNCs) [150, 151] and halloysite nanotubes (HNTs) [175] as interlayer materials were released, and the resultant interlayered TFC membranes have demonstrated enhanced separation performances in both water treatment and organic solvent treatment. Wang et al. [150] fabricated a TFC membrane using CNC as an interlayer. The influence of CNC loading amount on PA properties and TFC membrane performances were investigated. Results show that the cross-linking degree of PA layer decreased with increasing the CNC loading amount, which could be

attributed to the regulation of CNC to the IP reaction. However, the hydrophilic CNC interlayer also facilitated the water permeation during the NF process, making the TFC membranes exhibiting an ultra-high water permeation flux of 204 L m^{-2} h^{-1} with a Na_2SO_4 rejection of 96.7%.

Among these 1D interlayer materials, the CNT is the most widely used one due to its easy access, attractive smoothness, and hollow inner structure, which facilitate the rapid transport of water molecules inside and along the CNTs. The 1D steric configuration permits them to tightly stack into a continuous and homogeneous network and deposit onto porous substrates, which favors the formation of a defect-less overlying PA layer, thereby allowing for CNT-interlayered TFC membranes with high performance. Meanwhile, the specific functions of CNT interlayer are also under investigation to modulate the CNT interlayer from molecular level for better adapting to different application scenarios.

1.7. Advantages of using CNTs as interlayer material

With the use of CNT as the interlayer material, the CNT-interlayered TFC membranes are widely investigated in terms of the function of CNT interlayer and the different application. In this section, the regulation of CNT interlayer to the substrate layer and PA formation are summarized, and works on applying CNT-interlayered TFC membrane to different applications are reviewed.

1.7.1. Regulation of CNT interlayer on substrate and PA formation

As mentioned before, the 1D nanomaterials have more advantages than 2D and 3D nanomaterials in preparing the interlayer due to the formation of loose network with large specific surface area and less transport resistance. Similarly, the CNTs share their own advantages in comparison to CNCs and HNTs and other 1D nanomaterials from the following aspects: (1) CNT has much smaller diameter (e.g., <2 nm for single-walled CNT) and is more line-shaped under a certain aspect ratio, making it more flexible in attaching on the rough surface than the rigid and rod-shaped CNC and HNT [150]; (2) the formed intertwined CNT network could exhibit much uniformed pore

size and smoother surface features which are believed to be beneficial to the following IP reaction; (3) the abundant functional groups around CNT surface give possibilities to chemical modifications for different purposes such as hydrophilic or hydrophobic modification.

Given the advantages of CNT interlayer, it shows apparent effects on regulating the properties of substrate layer and PA formation. Shrinking the surface pore size, improving the surface porosity (depends on the structure of substrate), prohibiting the PA intrusion, and regulating the surface hydrophilicity and roughness is the main function that CNT interlayer can bring about [116, 117]. All these factors have been well demonstrated to be crucial factors for creating a detect-free PA layer.

For TFC FO membrane, substrate with large pore size is necessary for facilitating the substance transport and reducing the ICP phenomenon in FO process. For this purpose, MF membranes are often chosen as the substrate due to the large pore size and less density. However, the PA formed on MF substrate is usually less integral with poor perm-selectivity, which is because the severe PA intrusion into the large inner pores of substrate. In this case, introducing a CNT interlayer becomes a facile way to shrink pore size with little influences on the overall structure of MF substrate. By introducing a CNT interlayer, Zhou et al. [138] successfully reduced the pore size of PES MF substrate from ~600 nm to ~20 nm before conducting the IP reaction on the CNT interlayer. Thanks to the formation of large leaf-like PA layer and inhibited PA intrusion, the resultant CNT-interlayered TFC FO membrane exhibited seven times higher water flux as well as comparable salt rejection compared to previously reported FO membranes.

For expanding the application of TFC membrane to organic solvent separation, solvent-resistant substrate is an essential part for this purpose. Membranes such as PTFE and PVDF have become promising candidates for fabricating solvent-resistant TFC membrane. However, the hydrophobicity and large pore structures which are unpleasant features for IP reaction limit the further using of these membranes as the substrate of TFC membrane. Nevertheless, depositing a CNT interlayer can be a good way to solve the problem. Lu et al. [58] reported a fabrication of a high-permeance TFC

OSN membrane by the use of a PTFE MF substrate loaded with PDA-modified CNT network (PD/SWCNT/PTFE) as the support. A PA thin film has successfully grown on the surface of the CNT/PTFE composite membrane. The resulting PA TFC OSN membrane exhibits a high methanol permeance up to 13.2 L m^{-2} h^{-1} bar^{-1} with a rejection rate of 89.6% to 6-hydroxy-2-naphthalenesulfonic acid sodium salt (HNSA, Mw=246.21).

Besides regulating the substrate properties, the CNT interlayer can also influence the PA formation through enhancing or reducing the storage and release of IP monomer [112], which could further lead to differences in PA shaping induced by the reaction heat and nanobubbles release [170, 176]. For example, Ye et al. [176] tested the PIP diffusion behavior on the tannic acid-Fe(III) (TA-Fe) functionalized CNT interlayer to verify the effect of interlayer on the storage and diffusion of PIP during IP reaction. Results show that the PIP diffusion was hindered by increasing the interlayer amount, which was a result of the CNT functionalization using TA-Fe who provided a superior affinity to PIP molecules [177].

1.7.2. CNT-interlayered TFC membranes used in aqueous and non-aqueous separation

Over years, the CNT-interlayered TFC membrane have been widely investigated in NF [135, 147, 149, 176, 178], FO [171, 179] and RO [180, 181] applications. Gong et al. [139] reported a TFC NF membrane having a CNT interlayer. The structure and properties of PA active layer can be tuned by tailoring the properties of CNT interlayer. This TFC NF membrane exhibited a high divalent salt rejection (the rejection of Na_2SO_4 and $MgSO_4$ solution >98.3%) and dye rejection (the rejection of methyl violet (MV) >99.5%) with a high pure water flux around 21 L m^{-2} h^{-1} bar^{-1}, which are quite competitive performances among the reported NF membranes. Song et al. [180] reported a CNT interlayer having oriented CNT embedding in the PA separation layer. These semi-oriented CNTs along the transmembrane direction were proved to play a function of artificial water channel. The final TFC RO membrane presented extraordinary separation performance with high water permeance of 3.88 L $m^{-2}h^{-1}$/bar

and NaCl rejection of 99.2%, which far surpasses that of the normal CNT-interlayered TFC RO membranes.

After reaching success in aqueous separation, the CNT-interlayered TFC membranes are further applied to non-aqueous separation. One of the concerns of using CNT interlayers in organic solvent are their structural stability and the binding with substrates. Ye et al. [176] examined the structural stability of PTFE composite substrates coated with PDA-modified CNT layers (PD/SWCNT/PTFE) in various organic solvents by immersing the substrates in four organic solvents with different polarities, namely acetonitrile, methanol, DMF, and acetone. After 60-day soaking, the PD/SWCNT/PTFE composite substrates still maintain structural integrity, and no peeling phenomenon in the upper PD/SWCNT network film and no changes on their network structures were found, indicating that there is a strong binding force between the PD/SWCNT film and PTFE MF membrane. Zhou et al. [32] fabricated a CNT-interlayered TFC membrane using α-Al_2O_3 inorganic membrane as the substrate. PA selective layer with enlarged surface area was formed on the CNT interlayer. Combined with the highly permeable inorganic support, this membrane resulted a significant high ethanol permeance of ~10.6 L m^{-2} h^{-1} bar^{-1} and a high rhodamine B rejection of ~99.8%, which was approximately 4-13 times higher than that of conventional TFC PA membranes fabricated on polymer supports.

Due to the apparent performance enhancement of CNT-interlayered TFC membranes, more investigations on fabrication methods and structure optimization targeting specific applications are being conducted to further improve the membrane performances, which are imparting more potential in different processes.

1.8. Current problems of CNT-interlayered TFC membranes

Despite the plenty of works using CNTs as interlayer material to fabricate TFC membranes, there still some problems remain to be solved.

The first problem is lack of the understanding of CNT interlayer on controlling some certain surface properties of PA such as surface charges. Throughout the current works on CNT interlayers, most of them focus on the applicability of CNT interlayers to

different substrates and applications. However, the specific role of CNT interlayer on tailoring the PA surface properties is also important since part of the membrane performances are highly related to the membrane surface properties. Taking the property of surface charge as an example, the charge property of a membrane surface has been demonstrated as a decisive role affecting the membrane fouling in water treatment. The negatively charged foulants tend to deposit on a positively charged surface due to the electrostatic interaction and vice versa. Therefore, a neutral surface charge property is preferred to alleviate the charge-induced foulant adsorption indistinguishably. Apparently, this concept also works for the CNT-interlayered TFC membranes with satisfactory antifouling performances. Unfortunately, there are little investigations regarding to this aspect, which requiring further works in the future.

The second problem is the capability of CNT-interlayered TFC membrane to separate molecules with molecular weight less than 200 g/mol. The molecular weight cut-off (MWCO) is an important indicator to describe the pore size or rejection capability of a membrane in NF or OSN process. It refers to the lowest molecular weight solute (in g/mol) in which 90% of the solute is retained by the membrane. Although the CNT-interlayered TFC membrane can achieve a very high rejection of NaCl (99%~99.6%) in aqueous separation, this good retention capacity may not maintain in organic solvents due to the subsistent interactions between organic solvents and selective layers, resulting in a relatively high MWCO value. Currently, the reported CNT-interlayered TFC membranes share a MWCO range from 250 to 350 g/mol in OSN separation, which is lack of dominance in separating molecules with much lower molecular weight. However, the remarkable permeance enhancement brought by CNT interlayer still intrigues people to apply it for membrane modification. In the view of this situation, attempts on fabricating the CNT-interlayered TFC membrane with low MWCO is necessary to enlarge the application window of membrane to molecules with much smaller molecular size, for example, from solvent-solute separation (i.e., OSN) to solvent-solvent separation (i.e., OSRO). Moreover, the influence of CNT interlayer on forming a high-quality PA layer and its resultant effects on non-aqueous separations is also imperative to further investigate.

1.9. Research motivations and strategies

As seen from the above discussion, the CNT intercalation modification for TFC membranes still have plenty of room for improvement, calling for further investigations on in particular: (1) investigating the mechanism of CNT interlayer on shaping the PA morphology and surface properties; (2) reducing the MWCO of CNT-interlayered TFC membrane used in non-aqueous systems (i.e., OSN and OSRO). These motivations are therefore broken down into three works of this study:

(1) Intercalation of carbon nanotubes intermediate layer and its role in regulating the properties and performance of the polyamide selective layer

To figure out how the CNT intercalation modification influences the PA surface, a series of CNT-interlayered TFC membranes with different CNT interlayer thicknesses and IP monomer concentrations were prepared. By adjusting the amount of CNT, the PK surface properties was tailored. The function of CNT interlayer on shaping the morphology and structure of PA selective layer was studied through comparing the release of IP monomers. The effect of CNT interlayer on the membrane surface charge was investigated in terms of CNT interlayer thickness and IP monomer concentration. Finally, the antifouling performances were evaluated using surfactant and protein as model foulants.

(2) Organic solvent nanofiltration using carbon nanotube-interlayered thin film composite membrane

To acquire a TFC membrane with low MWCO for OSN application, the CNT-interlayered TFC membrane was further examined in OSN process for the removal of small molecules with molecular weight less than 200 g/mol. A series of triple-layered TFC membranes with CNT loading amount from 0 to 22.3 ug/cm^2 were prepared. The OSN performance of CNT-interlayered TFC membrane was fully investigated using dyes and drug molecules. The surface properties and chemical structure of PK substrate, CNT interlayer and PA selective layer were fully characterized. The long-term operation and solvent activation were performed to demonstrate the excellent separation capacity of TFC membrane.

(3) Molecular separation of organic solvent mixtures using carbon nanotube-interlayered thin film composite membrane

To further enlarge the separation scope on smaller scales, the solvent-solvent separation capacity of CNT-interlayered TFC membrane was examined in OSRO process for the first time. Since the CNT-interlayered TFC membrane has been well investigated in previous two works with enhanced performances demonstrated. Thus, in this work, a highly cross-linked tripe-layered TFC membrane was fabricated with using polydopamine (PDA)-modified CNT as the interlayer. Moreover, to illustrate the separation mechanism, the interactions between selective layer and different solvent mixtures were considered as one of the factors affecting the rejection, and were analyzed based on Hansen solubility parameters (HSP) theory by comparing the separation performances of three different kinds of solvent combinations. This work could provide insights on the design and fabrication of high-performance OSRO membrane also the understanding of solvent separation mechanism.

Chapter 2 Intercalation of carbon nanotubes intermediate layer and its role in regulating the properties and performance of the polyamide selective layer

2.1. Introduction

The exponential growth of the world's population and rapid economic development have led to a significant increase in the demand for clean and accessible water [182]. To address the water scarcity crisis, seawater desalination and wastewater reuse are increasingly being employed to provide a fresh and clean water supply [183, 184]. Due to the costly nature of conventional thermal-based desalination processes and the need for sustainable and efficient solutions in augmentation of water supply, alternative methods, such as membrane filtration, have been explored to mitigate water scarcity challenges while conserving energy [185].

Membrane applications have evolved to highly efficient processes not only for desalination [186, 187], as well as treatment of wastewater and industrial effluents [185]. Reverse osmosis (RO) is a pressure-driven membrane process that has gained extensive recognition and is considered the foremost technology for desalination and water treatment [188]. RO is now being widely employed in various applications, encompassing selective separation, purification, and concentration processes [189]. RO is able to separate dissolved solutes, which include monovalent ions like Na^+ and Cl^- and organic molecules with low molecular weights, from water through a semipermeable membrane that allows water to pass through while selectively blocking solutes.

An excellent membrane material candidate for RO is the thin film composite (TFC) membrane, which typically consists of a porous substrate and an ultrathin selective

polyamide (PA) layer prepared using interfacial polymerization (IP) [190]. Both the substrate and selective layers can be modified and controlled separately to achieve the desired properties and performance.

To fabricate high-performance TFC RO membranes, substantial works were conducted in terms of modifying the substrate and selective layer. Wherein, the interlayer intercalation strategy intrigues membrane scientists due to its less substrate-dependent. Moreover, the interlayer working as an individual layer between selective layer and substrate layer can be less affected by the agglomeration and compatibility problem, providing substantial choices on interlayer materials. Membrane scientists have developed several materials that can be used to fabricate interlayers, such as zeolite, ZIF-8, graphene oxide (GO), carbon nanotubes (CNTs) and cellulose nanocrystals (CNCs). Among them, the CNTs gained more interest to researchers due to their easy access, attractive smoothness, and hollow inner structure. The one-dimensional (1D) steric configuration permits them to tightly stack into a continuous and homogeneous network and deposit onto porous substrates, which favors the formation of a defect-less overlying PA layer, thereby allowing for CNT-interlayered TFC membranes with high performance.

On the other hand, the surface characteristics of TFC membranes are very important to ensure the quality of treatment process and managing surface interactions and foulant deposition mechanisms [191]. Roughness, porosity, pore size, exposed membrane surface area, polarity, and charge density all play significant roles in determining the performance of the membranes [192]. The membrane's selectivity and anti-fouling performance largely depend on the charge of its surface, which is consequently influenced by the polarizability of the functional groups at the liquid-solid interface [193]. Therefore, there is a pressing need for a straightforward method to control surface charge. Many researchers have attempted to customize the charge of the membrane surface to achieve efficient separation without sacrificing permeability, especially for treating solutions containing charged substances. Among the methods performed for membrane surface charge engineering in literature include layer-by-layer assembly [194, 195], specialized IP process [196], and surface grafting [193, 197].

These methods have certain limitations, such as multi-step operation, cumbersome process, and uncontrollable degree and rate of reaction [196]. Other earlier work on surface charge control of TFC membranes involve the quenching of residual acyl chloride groups in nascent PA films by secondary IP [198, 199] and regulation of the IP process to influence hydrolysis and cross-linking [200, 201].

Previous studies have demonstrated that CNT interlayer is a competitive material to modify TFC membranes by influencing the PA formation. However, the specific function of CNT interlayer thickness on shaping the PA morphology through affecting the IP has not been fully investigated yet. Moreover, the morphology of PA layer influences the permeability and selectivity of the membrane; however, the specific role of CNT interlayer on tailoring other surface properties, such as surface charge, which influences the performances of the TFC membranes for certain applications, such as fouling resistance and wastewater treatment, still remain unclear.

In this work, a network of CNT was applied as a coating on a polyketone (PK) substrate to control its surface characteristics and act as an interlayer for PA formation. The influence of the intercalation of CNT interlayer on PA morphology transition was investigated by determining the influence of CNT interlayer thickness on IP monomer release during PA generation. Aside from its influence on the structure of the PA selective layer, the effect of CNT interlayer on the membrane surface charge was investigated in terms of CNT interlayer thickness and IP monomer concentration. The membrane performance of the CNT-interlayered TFC membrane was investigated, including for ammonium separation, which was earlier found to be influenced by the cross-linking degree and surface charge of the PA selective layer [198, 202, 203]. Finally, the fouling control performance of the CNT-interlayered TFC membrane was investigated against model foulants, such as protein, surfactant, and bacteria. This work provides practical experimental observations and data on the mechanism of CNT to the PA formation, which offers a new perspective for understanding the role of interlayer on membrane fabrication.

2.2. Experimental

2.2.1. Materials

Polyketone (PK) polymer with a molecular weight of 200,000 g/mol was supplied by Asahi Kasei Co., Ltd. (Japan). Single-walled carbon nanotubes (CNTs, length range: 5–30 μm, diameter: < 2 nm, 95%) was purchased from Aladdin Chemical Co., Ltd. (China). 1,3,5-benzenetricarbonyl trichloride (TMC, 99%) and *m*-phenylenediamine (MPD, 99%) were purchased from Sigma-Aldrich Co., Ltd. (Japan). Resorcinol, sodium dodecyl benzene sulfonate (SDBS), acetonitrile, methanol, acetone, ethanol, isopropanol and hexane were purchased from Fujifilm Wako Pure Chemical Co. Ltd. (Japan). Deionized (DI) water was obtained from a water purification system manufactured (Merck Millipore Co., Ltd., Germany). Membrane testing was conducted with NaCl and NH_4Cl, both supplied by Wako Pure Chemical Co., Japan. Fouling control studies were performed using lysozyme (LYZ) (Wako Pure Chemical Co.), *Escherichia coli* (*E. coli*, NBRC 3301, Biological Resource Center, National Institute of Technology and Evaluation, Japan). Cetyltrimethylammonium bromide (CTAB, Sigma-Aldrich Co., Ltd.), tryptic soy broth (TSB, soybean casein digest medium, pH 7.3, Oxoid, Thermo Fisher Scientific, Japan) was used as the medium for *E. coli* culture. SYTO™ 9 green fluorescent nucleic acid stain (Life Technologies, Thermo Fisher Scientific) and glutaraldehyde (25%, aqueous solution, Sigma-Aldrich) were used for staining and fixing *E. coli* on the membrane surface. All chemicals were used as received without further purification.

2.2.2. PK membrane casting

The PK membrane substrate was fabricated by nonsolvent-induced phase separation (NIPS) [204]. Firstly, 10 wt% PK powder was dissolved in the mixture of resorcinol and DI water (35:65, wt%). The mixture was stirred at 80℃ for at least 5 h to form a homogenous casting solution. After overnight degassing at 60℃, the PK solution was cast onto a clean glass plate with a casting gap of 400 μm. Then, the casting plate was immediately immersed into a precipitation bath of methanol/water (35:65, wt%) for 20

min before transferring into pure acetone and hexane and immersing for 20 min each to make sure the membrane was fully washed. Finally, the PK membrane was dried in the air and stored for further used.

2.2.3. Fabrication of PK-CNT substrates and TFC membranes

To ensure the even coverage of the CNT layer, a dispersion process using SDBS surfactant was employed before coating. 10 mg SWCNT and 100 mg SDBS were dispersed in 100 mL of DI water. The mixture underwent probe sonication (SFX 250, BRANSON, Mexico) for 8 h and was then centrifuged at 10,000 rpm for 1 h. The supernatant, with a concentration of 0.098±0.011 mg/mL, was collected and used as the final CNT dispersion.

To create the PK-CNT substrate, a specific volume of the CNT dispersion (ranging from 0.1 to 3 mL CNT dispersion, diluted to 80 mL using DI water before filtration) was filtered onto the PK membrane (effective membrane area: 12.56 cm^2) using vacuum filtration method. The PK-CNT substrate was subsequently dried in an oven at 45℃ for a minimum of 4 h and then stored at room temperature until use. The PK-CNT substrates were labelled as PK-CNT-*x,* with *x* representing the corresponding volume of CNT dispersion used during filtration. The CNT loading amounts corresponding to different filtration volumes of CNT dispersion were summarized in **Table 2.1**.

Table 2.1. Sample names, CNT filtration volumes and their corresponding loading amounts.

Sample	CNT filtration volume (mL)	CNT loading amount (ug/cm^2)
PK	0	0
PK-CNT-0.1	0.1	0.74
PK-CNT-0.3	0.3	2.23
PK-CNT-0.5	0.5	3.71
PK-CNT-0.7	0.7	5.20
PK-CNT-1	1	7.43
PK-CNT-1.5	1.5	11.1
PK-CNT-2	2	14.9
PK-CNT-3	3	22.3

The TFC membranes used in this work were fabricated through interfacial polymerization (IP) using MPD and TMC following the reported method. Briefly, the PK-CNT substrate was fixed on a glass plate with CNT side face to the air. Then, 2 wt% MPD aqueous solution was induced onto the CNT side. After prewetted for 2 min, the excess MPD solution was poured out and the underlying PK-CNT substrate was gently dried using an air brush with a pressure below 0.1 MPa. Subsequently, 0.1 wt% TMC solution in hexane was poured onto the CNT side to react with the MPD molecules for 1 min. After removing the excess TMC solution, the nascent TFC membrane was further cured at 60℃ for 10 min. The control sample was also fabricated following the same IP procedure except using the pristine PK membrane as substrate. The fabricated membranes having different CNT loading amount were labelled as TFC-*y* which *y* represents the CNT filtration amount during fabricating the CNT interlayer. Unless stated otherwise, all TFC membranes were fabricated with an MPD concentration of 2 wt%. All TFC membranes were preserved in DI water at 4℃ for further use. The membrane fabrication process was shown in **Figure 2.1**.

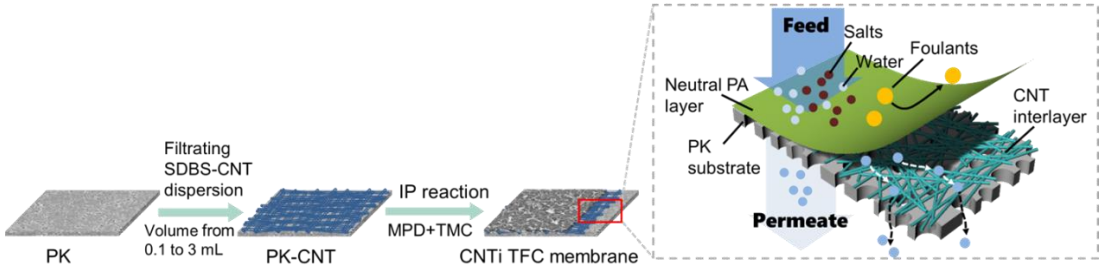

Figure 2.1. Schematic diagram of the fabrication of CNT-interlayered TFC membranes.

2.2.4. Membrane characterization

The membrane surface and cross-section morphologies were observed using field-emission scanning electron microscopy (FE-SEM, JSF-750F, JEOL, Japan) and transmission electron microscopy (TEM, JEM-2100F, JEOL, Japan). The *Image J* software was applied to analyze the surface pore size and porosity changes of PK membrane before and after CNT deposition based on SEM images. The element composition was detected using X-ray photoelectron spectroscopy (XPS, JPS-9010MC, JEOL, Japan) with monochromatic Mg Kα excitation. Fourier transform infrared

spectrometer (FTIR, Nicolet iS50, Thermo Fisher, USA) were applied to analyze the surface chemical composition. The overall pore size distribution was detected using a liquid-liquid displacement porometer (LLDP, LLP-1200A, Porous Material Inc, USA). The membrane was initially soaked in isopropanol prior to displaced by a specific testing liquid Galwick® (surface tension: 15.9 dynes/cm) in a pore size measurement. The membrane surface hydrophilicity was measured by a contact angle analyzer (WCA, DM-300, Kyowa, Japan) with a droplet volume of 2 μL. All samples were fully dried in an oven at 60℃ overnight before characterizations and all tests were performed at room temperature. The surface zeta potential of the TFC membranes was evaluated at different pH values of 3 to 10 using an electrokinetic solid surface analyzer (SurPASS 3, Anton-Paar GmbH, Austria).

2.2.5. Measurements of MPD storage capacity and release rate of PK and PK-CNT substrates

The MPD storage capacity and release rate of different substrate were determined according to a reported method [141, 205] (**Figure 2.2**). Briefly, a certain amount of MPD solution (2 wt%) was poured onto the top surface of substrate (membrane area: 1.017×10^{-3} m^2). After prewetting for 2 min, the excess MPD solution was removed from the substrate using air brush. Subsequently, the MPD-impregnated substrate was immersed into pure hexane without TMC. The concentration of released MPD in hexane was detected by an ultraviolet-visible (UV-vis) spectrophotometer (V-650KE, JASCO, Japan) based on a calibration curve of MPD concentration versus UV absorption at 295 nm (**Figure 2.3**).

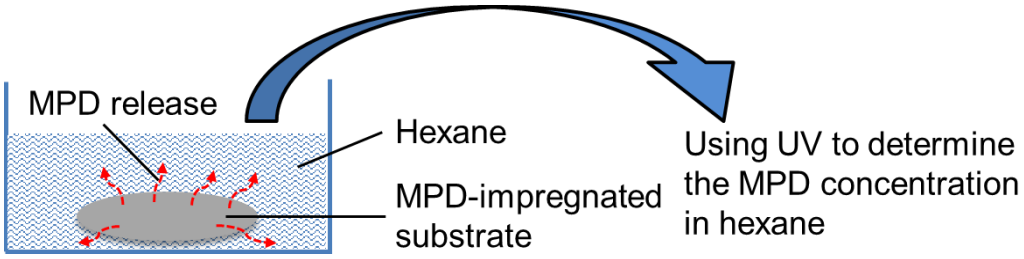

Figure 2.2. Schematic diagram of MPD storage capacity and release rate evaluation.

The MPD concentration variation ($\Delta Conc._{MPD-O}$, g/L) within a certain time duration of 1 min (Δt, min) was recorded and the release rate was represented as S_{MPD-O} (g L^{-1} min^{-1}) calculated based on the following equation:

$$S_{MPD-O} = \frac{\Delta Conc._{MPD-O}}{\Delta t} \quad (2\text{-}1)$$

Similarly, based on the stabilized MPD concentration after at least 6-h immersion, the MPD storage capacity C_{MPD} (g/m^2) was calculated according to the following equation:

$$C_{MPD} = \frac{Conc._{MPD-O,S} V_O}{A} \quad (2\text{-}2)$$

where $Conc._{MPD-O,S}$ (g L^{-1}) is the stabilized MPD concentration in organic phase; V_O (mL) is the volume of the organic phase (50 mL); A (m^2) is the membrane surface area which is 1.017×10^{-3} m^2 in this work.

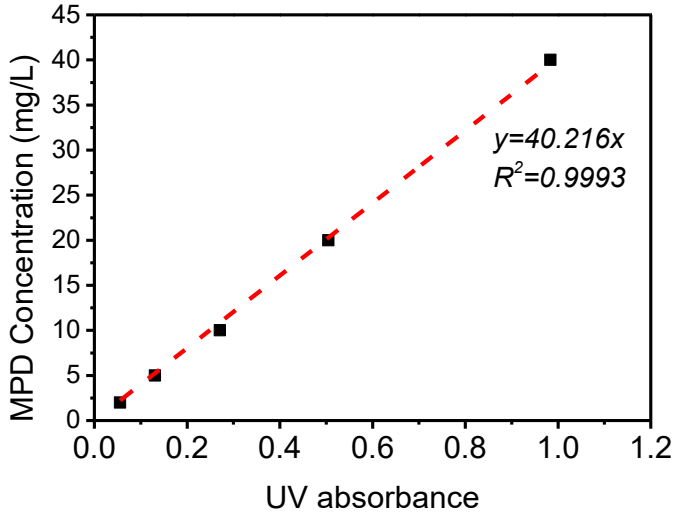

Figure 2.3. Calibration curve MPD concentration in hexane versus UV absorption at 295 nm.

2.2.6. Membrane performance evaluation

Filtration tests were conducted using a laboratory-scale cross-flow reverse osmosis (RO) system equipped with a membrane cell with an effective membrane area of 7.065 cm^2. The TFC membranes were pre-compacted with DI water at 20 bar for 1 h before filtration to obtain a steady permeate flux under 15 bar. DI water, 2000 mg L^{-1} NaCl, and 400 mg L^{-1} NH_4^+ (from NH_4Cl) were used as feed solutions. Water permeance (P,

L m^{-2} h^{-1}/bar, LMH/bar) and solute rejection (R, %) could be calculated based on the following equations:

$$P = \frac{M}{S \times t \times \rho \times p} \quad (2\text{-}3)$$

where M (g) is the weight gain of permeate within a certain testing period; S (m^2) is the effective membrane area; t (h) represents the filtration time; ρ (g/L) is the density of permeate; p (bar) is the operation pressure which is fixed at 5 bar during the testing.

$$R = \left(1 - \frac{C_p}{C_f}\right) \times 100\% \quad (2\text{-}4)$$

where C_p and C_f are the solute concentrations of permeate and feed solution, respectively. NH_4^+ concentrations in the feed and permeate solutions were measured using an ammonia test kit (Hach Co., Japan).

2.2.7. Fouling control evaluation

Fluorescent isothiocyanate-conjugated LYZ (isoelectric point: 10.5) was utilized as a model foulant to assess the membrane's ability to mitigate organic fouling. The membrane samples were immersed in a phosphate buffered saline solution (PBS, pH 7.4) containing 20 mg L^{-1} of the fluorescent protein. At pH 7.4, LYZ is positively-charged. The membranes were kept in the dark under 100 rpm agitation at room temperature for 12 h. Subsequently, the samples were rinsed with PBS solution to remove loosely-attached proteins. Confocal laser scanning microscopy (CLSM, FV1000D, Olympus Corp., Japan) was employed to image the membrane samples, and the images were analyzed using ImageJ software (National Institute of Health, USA).

The antibacterial properties of the prepared membranes were assessed by examining the adhesion of *E. coli*. Initially, a colony of *E. coli* from an agar dish was precultured in 20 mL of a 30 g L^{-1} fresh TSB medium for 12 h at 30 °C while shaking at 120 rpm, to reach a mid-exponential growth phase. The precultured bacterial suspension culture was diluted 50 times using TSB medium and cultured for 4 hours at 30°C under the same shaking conditions. Finally, the cultured bacterial suspension was diluted with TSB medium to an optical density of 0.05 at 450 nm (106 – 107 CFU mL^{-1}). For testing the membrane's bacterial adhesion property, membranes samples were soaked in 2 mL

of the bacterial suspension (pH 7). The membranes were incubated in the bacterial suspension at 30°C while shaking at 120 rpm for 24 h. Following incubation, the samples were rinsed twice with a 0.85% (w/w) aqueous NaCl solution and stained using SYTO™ 9 green fluorescent nucleic acid stain. The stained bacteria were fixed by immersing the membranes in a 2.5% (v/v) aqueous glutaraldehyde solution for 10 minutes and then placed in a 0.85% (w/w) aqueous NaCl solution. CLSM was employed for a qualitative assessment of the quantity of bacterial cells attached to the membranes.

Dynamic filtration using two model positively-charged foulants, protein LYZ and surfactant CTAB, was also conducted using the cross-flow RO setup. 2000 mg L^{-1} NaCl was first used as the feed solution until 50 mL of permeate was collected, and afterwards, the feed was replaced with 200 mg L^{-1} LYZ solution, and the operation continued until 400 mL of permeate was collected. On the other hand, the dynamic filtration using 200 mg L^{-1} CTAB was conducted in two cycles. In one cycle, 200 mg L^{-1} was first used as the feed solution until 25 mL of permeate was collected, and the feed was replaced with CTAB solution until 100 mL of permeate was collected. After which, NaCl solution was used as the feed solution again. The feed solutions were kept at a constant pH of 6.5 to 7.0 throughout the operation to maintain the charge of the model foulants and the membrane surface. The normalized water flux, or the ratio of the instantaneous and initial water flux values, were used to evaluate the fouling propensity and flux recovery.

2.3. Results and discussions

2.3.1. Structure and properties of PK-CNT substrates

By using NIPS and filtration deposition method, the PK and PK-CNT substrates were successfully prepared. **Figure 2.4** shows the surface morphologies of both pristine PK and PK-CNT substrates at various CNT loading amounts. To avoid any confusion, the filtration volume (0.1 to 3 mL) was used as the representative of loading amount. As the CNT loading increased, the PK surface became progressively covered by CNT, forming a continuous CNT network when the loading amount reached 0.5 (PK-CNT-

0.5). The CNT network tightly integrated with the PK surface due to the flexible structure of CNT, making it difficult to distinguish a clear boundary between PK and CNT network in the cross-sectional SEM images. To determine the thickness of the CNT layer, TEM analysis was conducted (**Figure 2.8**), revealing a linear increase in thickness with increasing the CNT loading amount (**Figure 2.7b**). This indicates that the filtration method employed in this work was reliable and reproducible for fabricating the CNT layer.

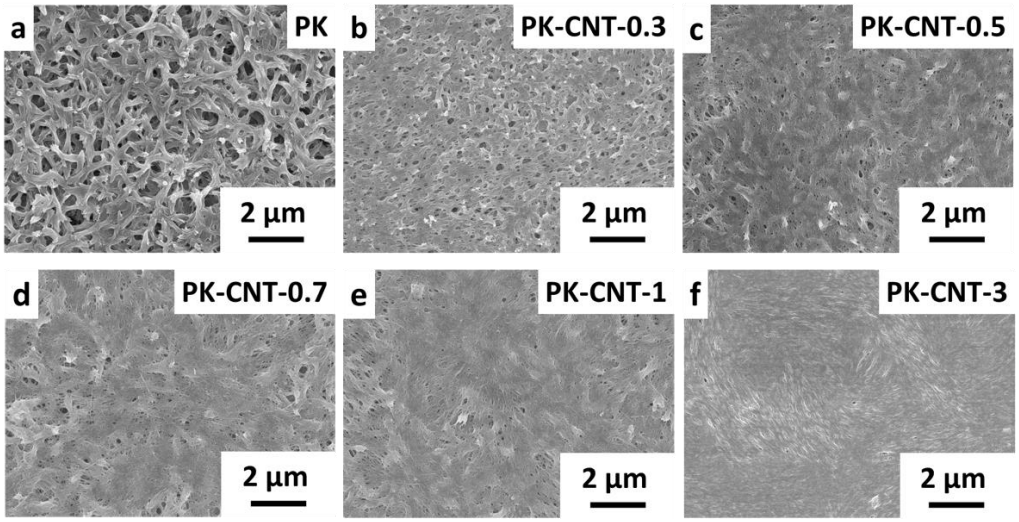

Figure 2.4. SEM surface morphology of PK and PK-CNT substrates.

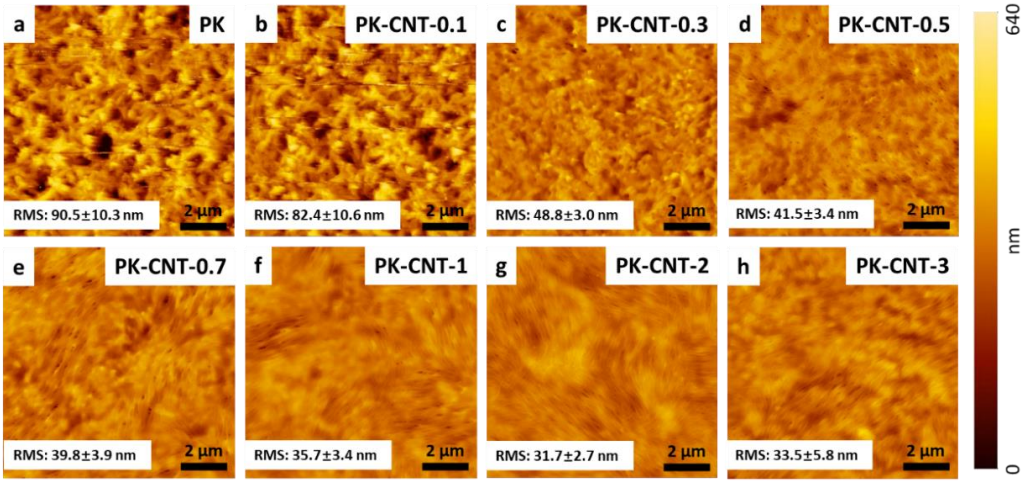

Figure 2.5. Large-scaled AFM images and corresponding surface roughness of PK and PK-CNT substrates with varying CNT loading amounts.

The AFM image in **Figure 2.5** provides a clearer view of the CNT layer with varying CNT loading amounts. The root-mean-square (RMS) surface roughness of the PK-CNT substrates decreased as the CNT loading amount increased, as summarized in **Table 2.2**. This reduction in surface roughness was a result of the CNT gradually masking the original surface features of PK.

One widely accepted concept is that, a moderate pore size of the substrate plays a positive role in PA formation and the TFC membrane performance [206]. This is due to its influence on IP monomer distribution [207] and the prevention of PA intrusion [139]. To further demonstrate the function of the CNT layer in regulating pore size, measurements of surface pore size distribution was conducted on PK after coating with CNT. Results depicted in **Figure 2.6a** reveal that as the CNT loading amount increased, the surface pore size shifted to a smaller range, with a central distribution reducing from approximately 150 nm for the pristine PK to about 20 nm for PK-CNT-0.5. This reduction in pore size for higher CNT loading amounts was consistent with previous literature [139, 176, 208]. However, when the CNT loading amount was increased to 0.7 and 1, the surface pore size did not change significantly. This was attributed to the fact that at a loading amount of 0.5, the CNT network had already formed and covered the PK surface, and further increases in loading amount mainly affected the thickness of the CNT layer rather than the surface pore size.

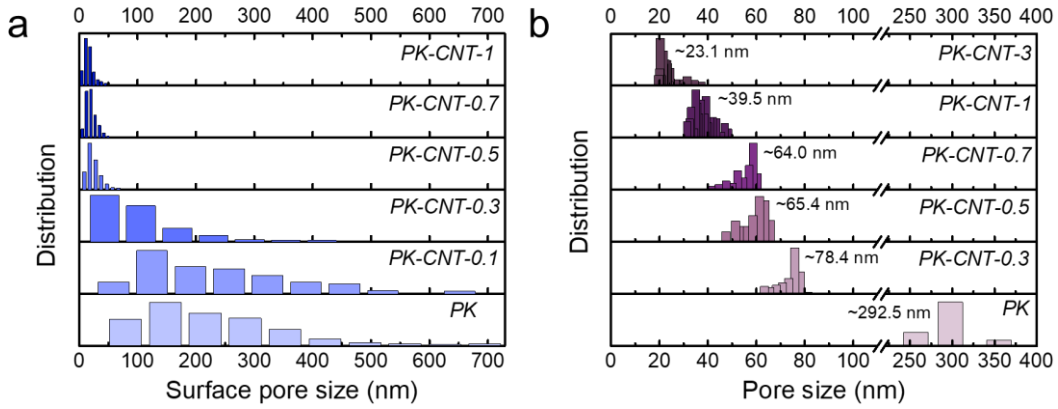

Figure 2.6. Surface (a) and overall (b) pore size of PK and PK-CNT substrate.

Moreover, the overall pore size distribution of the membranes, evaluated using a

liquid-liquid displacement porometer (LLDP) (**Figure 2.6b**), also showed an obvious change in pore size. The overall pore sizes of each membrane were observed to be slightly larger than those of the corresponding surface pore sizes. This is quite understandable since the LLDP measures the size of all pores in the membrane bulk, while the other only measures the sizes of the pores on the surface. Moreover, the difference between two kinds of pore size values became smaller with increasing CNT loading amount. For example, the overall pore size of PK substrate (~292.5 nm) was around two times higher than its surface one (~150 nm), and for PK-CNT-3, both two kinds of pore size became quite close (~20 nm for the surface, and ~23.1 nm for the overall). This shows that as the CNT layer thickness increases, the proportion of CNT layer participating in the evaluation of the overall pore size also increases. All these results demonstrate the effectiveness of CNT in adjusting the substrate pore size.

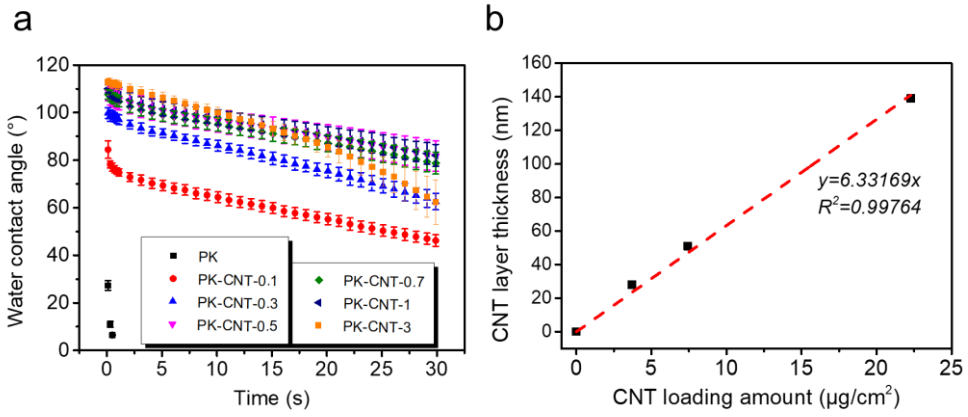

Figure 2.7. (a) Dynamic WCA of PK and PK-CNT substrate; (b) Linear increase in CNT interlayer thickness with increasing the CNT loading amount.

The additional properties of PK and PK-CNT substrates were listed in **Table 2.2**. The pure water permeance (PWP) values of PK and PK-CNT substrates were measured using a cross-flow ultrafiltration setup. Pristine PK exhibited a PWP of 3390±303 L m^{-2} h^{-1}/bar, and the PWP gradually decreased with increasing the CNT loading amount. This trend of reduced water permeance aligned with the decreased pore size and increased thickness after coating with CNT. Regarding hydrophilicity changes brought about by the CNT layer, water contact angle (WCA) measurements were employed,

and results were listed in **Table 2.2**. Pristine PK demonstrated excellent water affinity, with water droplets quickly spreading out and penetrating into the membrane instantaneously (the dynamic WCA profiles of PK and PK-CNT substrates are shown in **Figure 2.7a**). However, after introducing the CNT layer, the substrate surface became slightly hydrophobic, and the WCA increased to 80~90° (**Table 2.2**). This hydrophobic property was attributed to the non-functionalized nature of the CNT used in this study, which retained their intrinsic hydrophobic characteristics. Additionally, the reduced pore size and surface roughness contributed to the increased WCA. The moderate hydrophobic surface property was believed to facilitate easier molecule release and potentially affect the PA formation, which will be discussed in detail in the following sections.

Table 2.2. Properties of PK and PK-CNT substrates.

Samples	CNT loading amount (ug/cm^2)	CNT layer thickness (nm) [a]	RMS roughness (nm)	WCA (°) [b]	Pure water permeance (PWP) ($L\ m^{-2}\ h^{-1}$/bar)
PK	0	0	90.5±9.8	N/A	3390±303
PK-CNT-0.3	2.23	~14 [c]	48.8±3.0	80.7±2.7	2840±284
PK-CNT-0.5	3.71	28±5	41.5±3.4	93.0±5.1	1190±90
PK-CNT-1	7.43	51±4	35.7±3.4	90.4±3.5	843±65
PK-CNT-3	22.3	139±9	33.5±5.8	89.1±3.0	584±42

[a] CNT interlayer thicknesses were estimated from the TEM images of TFC membranes shown in **Figure 2.8**.

[b] WCA was measured after the water droplet was in contact with the membrane for 15s. The dynamic WCA profiles are shown in **Figure 2.7a.**

[c] This value was calculated based on the fitted curve shown in **Figure 2.7b**. Due to the ultralow CNT loading amount, it is still difficult to distinguish the boundaries in TEM at this CNT loading amount.

In summary, the CNT have successfully modified the surface properties of the PK membrane, resulting in smaller pore size, retained high surface porosity, and reduced hydrophilicity. These changes are believed to work together synergistically in the PA formation and influence the transport properties during separation, which will be further discussed in the following sections.

2.3.2. Effect of CNT interlayer on PA morphology and surface properties

After coating the CNT layer on the PK substrate, significant changes occurred in the surface properties, which were believed to influence the formation and properties of the PA layer. In this study, a detailed characterization and comparison on morphology of PA layer were performed.

Given that the membrane surface morphology plays an important role on the effective filtration area or fouling tendency during the filtration process, a detailed morphology comparison of the TFC membrane having different CNT interlayer was conducted (**Figure 2.8**). For the pristine TFC-C membrane (without CNT), the surface SEM image revealed two distinct structures: ridge-and-valley and nodular structures (**Figure 2.8a**). However, upon introducing a CNT intermediate layer with loading amount of 0.3, the ridge-and-valley structures transformed into larger leaf-like structures, and the nodular structures gradually transitioned into ridge-and-valley structures (**Figure 2.8e**). This change in structure was also evident in the cross-sectional SEM and TEM images, confirming an increase of apparent thickness of the PA layer due to the formation of leaf-like structures (**Figure 2.8b-d** and **Figure 2.8f-h** for TFC-C and TFC-0.3, respectively). This observation suggested that the IP reaction was somehow promoted by the presence of the CNT interlayer. Further increasing the CNT loading amount to 0.5 at which the CNT network covered the PK surface, the PA layer resulted in the appearance of large PA leaves covering the membrane surface (**Figure 2.8i**). The cross-sectional SEM and TEM images clearly displayed the multi-layered structure of PA, where the PA leaves overlapping with the PA parts formed at the base of the PA layer, thereby resulting in a multilayer structure (**Figure 2.8j-l**). However, when the CNT loading amount was increased to 1 and 3, a retreat of the overlapping tendency of PA was observed, accompanied by a reduction in leaf-like structures and even a re-appearance of nodular structures on the TFC-3 membrane (**Figure 2.8q-t**). This distinct transition in PA morphology indicates that there exists an upper limit for the CNT layer's facilitation to the PA formation, which is believed to be related to the CNT interlayer thickness and its influence on the IP reaction. The possible formation

mechanism will be discussed in detail in Section 2.3.3 of this work.

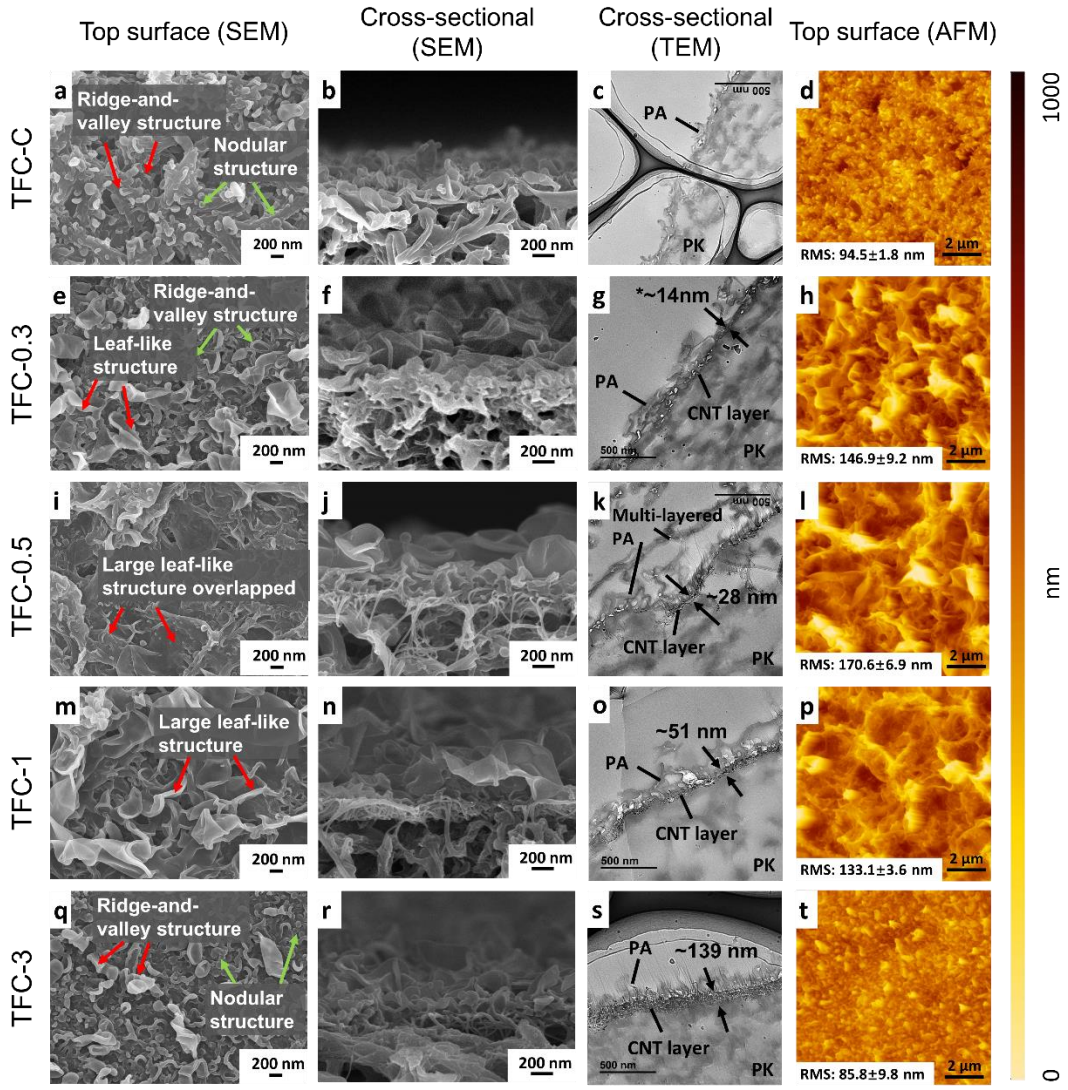

Figure 2.8. Surface and cross-sectional morphologies of TFC-C (a, b, c and d), TFC-0.3 (e, f, g and h), TFC-0.5 (i, j, k and l), TFC-1 (m, n, o and p) and TFC-3 (q, r, s and t). The CNT interlayer thicknesses were estimated based on the scale bar of TEM images except for the TFC-0.3 membrane for which the thickness was calculated based on the fitted curve given in **Figure 2.7b**.

Additional surface properties of TFC membranes were summarized in **Table 2.3**. The WCA values for all TFC membranes were around 70°.The surface roughness initially increased from ~94.5 nm to ~171 nm as the CNT loading amount increased from 0 to 0.5, and then gradually decreased to ~85.8 nm due to the retreat of the leaf-like structure.

This trend was consistent with the observed transition in PA morphology seen in the SEM images (**Figure 2.8**).

Table 2.3. Surface properties of the fabricated TFC membranes.

Samples	RMS roughness (nm)	WCA (°) [a]
TFC-C	94.5±1.8	72.1±2.2
TFC-0.1	130±1	69.8±2.5
TFC-0.3	147±9	67.4±1.6
TFC-0.5	171±7	66.8±1.0
TFC-0.7	153±12	69.6±1.4
TFC-1	133±4	70.8±2.2
TFC-3	85.8±9.8	74.6±3.1

[a] WCA was measured after the water droplet was in contact with the membrane for 15s.

The chemical composition of the pristine and CNT intermediate layer-intercalated TFC membranes were analyzed using XPS. The XPS wide spectra was given in **Figure 2.9**.

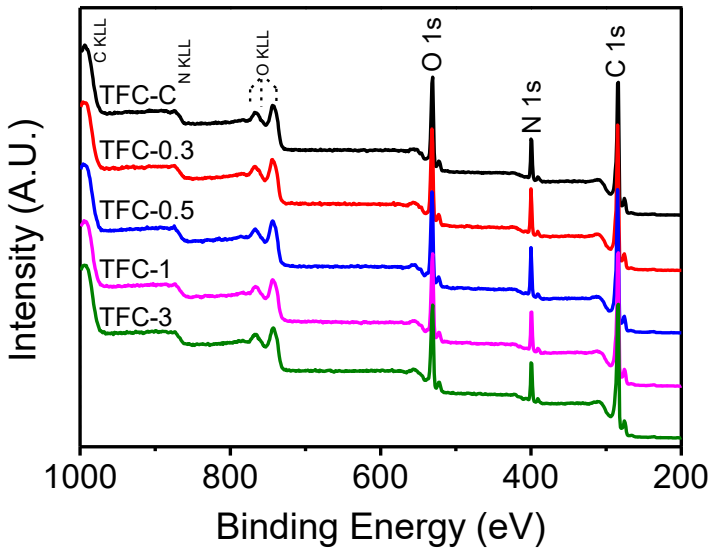

Figure 2.9. Wide-scan XPS spectra of TFC membranes with different CNT interlayers.

The cross-linking degree of the PA selective layers of the TFC membranes are shown in **Figure 2.10**. The pristine TFC membrane has a cross-linking degree of 0.48, and the cross-linking degree of the PA selective layer was observed to increase with the intercalation of the CNT intermediate layer. As the CNT dispersion coating amount increased, the cross-linking degree was observed to increase as well, with the highest

cross-linking degree of 0.67 for TFC-1 (TFC membrane prepared using PK substrate coated with 1 mL CNT dispersion). Further increasing the amount of CNT coating on the membrane substrate resulted in lower cross-linking degree values within the range of 0.57 (TFC-2) to 0.63 (TFC-1.5), which were all still higher than that of the pristine TFC membrane.

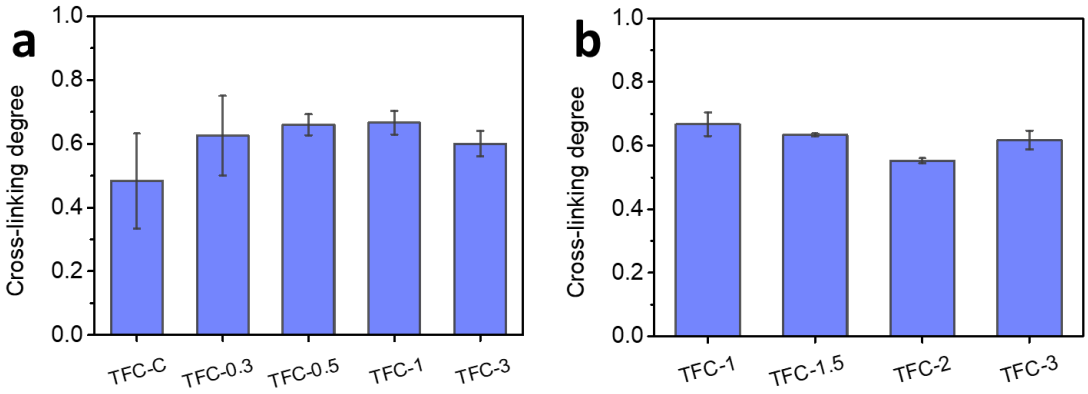

Figure 2.10. Cross-linking degree of the pristine TFC-C membrane and CNT-interlayered TFC membranes (TFC-x, where x is the amount [mL] of the CNT dispersion used for coating the PK substrate). The cross-linking degree was calculated based on the equation [209]: $\frac{N}{O} = \frac{3n+2(1-n)}{3n+4(1-n)}$. Element compositions are shown in **Table 2.4**.

Table 2.4. Elemental compositions of the fabricated TFC membrane detected by XPS.

Membrane	Element content (%)			Element ratio N/O	Cross-linking degree
	C	N	O		
TFC-C	73.1±1.2	11.1±0.9	15.8±0.8	0.71±0.07	0.48±0.15
TFC-0.3	72.4±0.4	12.1±0.7	15.5±0.5	0.78±0.07	0.63±0.12
TFC-0.5	72.6±0.2	12.2±0.1	15.3±0.3	0.80±0.02	0.66±0.03
TFC-1	73.4±0.1	11.4±0.7	15.3±0.6	0.80±0.02	0.67±0.04
TFC-3	72.9±0.3	11.7±0.1	15.4±0.3	0.76±0.02	0.60±0.04

Figure 2.11 shows the narrow scan spectra corresponding to oxygen (O1s) and carbon (C1s). The reduced percentage of O-C=O in **Figure 2.11a** also consisted with the increased cross-linking degree, indicating the validation of CNT interlayer on affecting the cross-linking degree of PA layer.

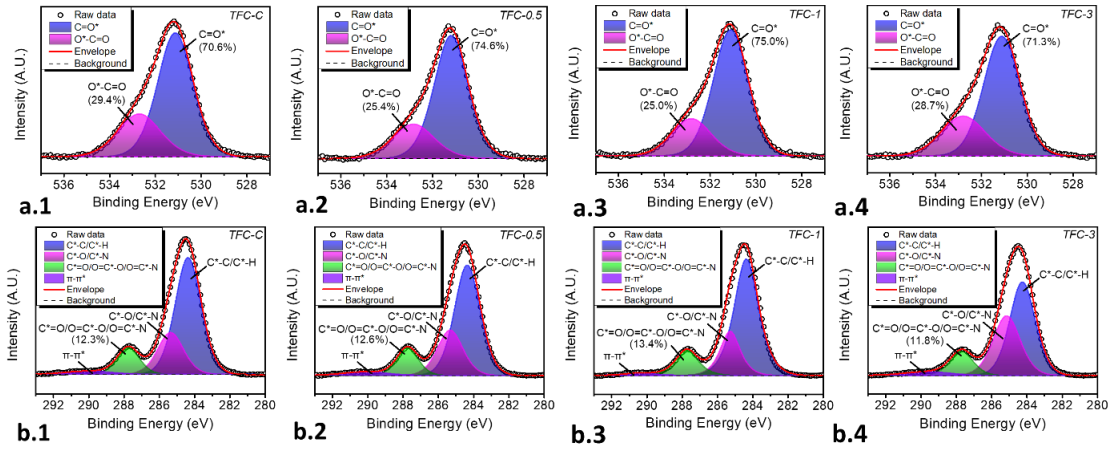

Figure 2.11. Narrow scan spectra of the TFC membranes obtained using XPS analysis. High-resolution deconvolution peaks of (a) oxygen (O1s) and (b) carbon (C1s) are provided. Legend: (1) Pristine (TFC-C), (2-4) TFC membrane prepared with substrate coated with 0.5, 1, and 3 mL of carbon nanotube dispersion.

The zeta potential of the pristine and CNT intermediate layer-intercalated membranes over a pH range of 3 to 10 was measured to analyze the influence of the presence of CNT intermediate layer on the TFC membrane's surface charge, and the curves are shown in **Figure 2.12**. The isoelectric points, or the pH at which the zeta potential is zero, of the TFC membranes are also highlighted. These isoelectric points were observed due to the protonation of amine groups and the dissociation of carboxyl groups at certain pH conditions. In comparison to the pristine TFC membrane, the TFC membranes with CNT intermediate layer exhibited less negative charge across almost all pH values, and the isoelectric points were observed at a higher pH value.

Comparing the TFC membranes with CNT intermediate layer, there was a clear change in the surface zeta potential as the CNT dispersion coating volume increased. As shown in **Figure 2.12a**, with an increase of CNT dispersion coating volume from

0.1 mL to 1 mL, the surface of the TFC membrane became less negative, with TFC-1 membrane exhibiting generally neutral to positive charges at all pH values. Further increasing the CNT dispersion volume during membrane substrate coating did not result in any significant change in the membrane surface zeta potential (**Figure 2.12b**).

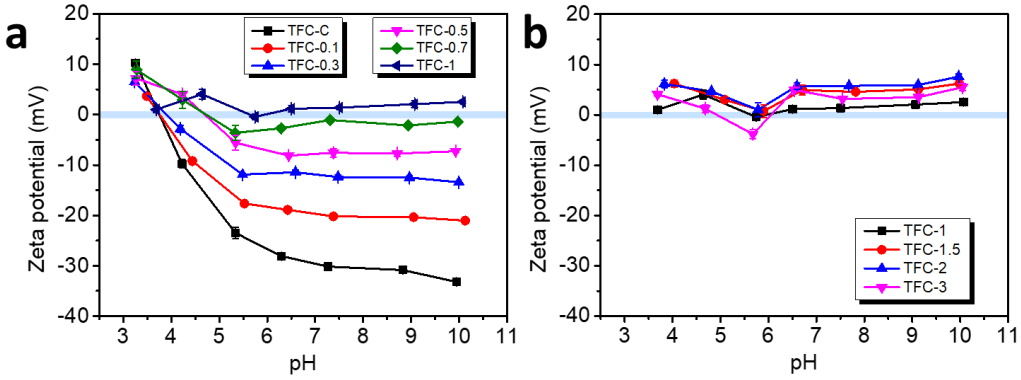

Figure 2.12. Zeta potential of the pristine TFC-C membrane and CNT-interlayered TFC membranes (TFC-x, where x is the amount [mL] of the CNT dispersion used for coating the PK substrate).

To further investigate the influence of the intercalation of CNT intermediate layer and discount the influence of the IP reaction conditions on the PA formation, the membrane substrate coated with 1 mL of the CNT dispersion (PK-CNT-1) was used as the substrate for IP reactions using different combinations of MPD and TMC concentrations. It is widely known that the negative surface charge of PA TFC membranes is mainly attributed to the unreacted carboxyl groups of TMC, thus, four new membranes were prepared with the PK-CNT-1 and different combinations of MPD and TMC concentrations during the IP process: (1) 0.4 wt% MPD and 0.02 wt% TMC (TFC-1 (0.4, (2) 1 wt% MPD and 0.05 wt% TMC, (3) 2 wt% MPD and 0.1 wt% TMC, and (4) 4 wt% MPD and 0.2 wt% TMC. The surface morphologies of these TFC membranes are exhibited in **Figure 2.13a**. When both MPD and TMC concentrations were divided by 5 (TFC-1 (0.4/0.02)) and 2 (TFC-1 (1/0.05)), the surface structure was observed to be similar with the TFC membrane prepared with the normal IP conditions (TFC-1 (2/0.1)). When both monomers were doubled in concentration (TFC-1 (4/0.2)),

there was an observed denser nodular PA structure different from the other TFC membranes. Despite the differences in the PA morphology of the TFC membranes, all membranes exhibited similar surface zeta potential measurements across the measurement pH range (**Figure 2.13b**). Despite in differences in the MPD and TMC monomer concentrations during the IP process, generally neutral to slightly positive surfaces were obtained when IP was conducted atop a PK membrane substrate coated with a CNT intermediate layer. **Figure 2.13c** shows the cross-linking degree of the TFC membranes. The TFC-1 (0.4/0.02), TFC-1 (1/0.05), and TFC-1 (2/0.1) membranes all showed similar cross-linking degrees of 0.60 to 0.67. Comparing these three, there was a noticeable increase as the amount of IP monomers, but the changes were only marginal. TFC-1 (4/0.2), on the other hand, exhibited the highest cross-linking degree of 0.79, which could be attributed to the facilitation of more PA formation when there were more reactants present during the reaction.

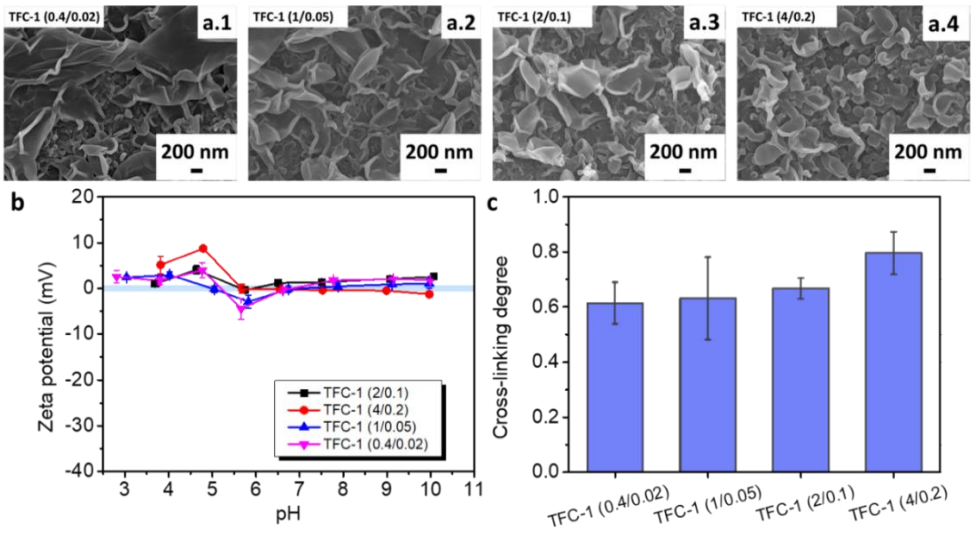

Figure 2.13. Characterization of TFC membranes prepared using PK membrane support coated with 1 mL CNT dispersion and different MPD and TMC concentrations during IP. (1) 0.4 wt% MPD and 0.02 wt% TMC, (2) 1 wt% MPD and 0.05 wt% TMC, (3) 2 wt% MPD and 0.1 wt% TMC (normal IP conditions), and (4) 4 wt% MPD and 0.2 wt% TMC; (a) Surface morphology, (b) zeta potential measurements over a pH range of 3 to 10, and (c) cross-linking degree. Other conditions during the IP process were held constant as the rest of this work.

All the membranes with CNT intermediate layer displayed less negative surface charges than the pristine membrane, as shown by zeta potential measurements (**Figure 2.12** and **Figure 2.13b**). Earlier studies which involved amine grafting on top of TFC membranes and secondary interfacial polymerization attributed the generally less negative charges of TFC membranes to the consumption of the carboxyl (−COO−) groups during the reaction with amine groups that occurred during the grafting and successive interfacial polymerization processes [198, 202, 203]. However, in the case of this work, no further modification was conducted on the PA layer, except for the intercalation of the CNT intermediate layer.

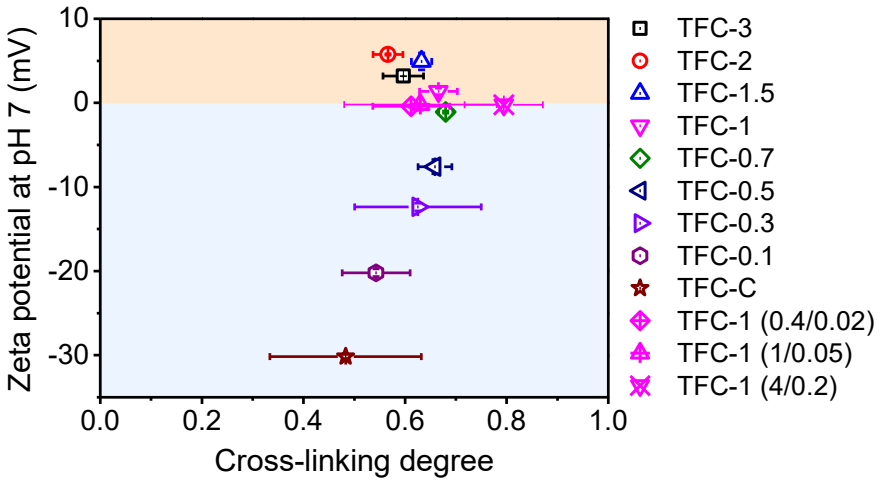

Figure 2.14. Correlation of the zeta potential at pH 7 and the cross-linking degree of the thin film composite membranes prepared in this work.

Figure 2.14 shows the correlation of the surface zeta potential measurements at pH 7 of the TFC membranes prepared in this work and the membranes' corresponding cross-linking degree values. It was observed that there was a clear correlation between the membranes' cross-linking degree and their charge densities. The pristine TFC membrane (TFC-C) was observed to have the lowest cross-linking and the most negatively-charged membrane surface, as well. When the CNT intermediate layer was introduced, there was an observed increase in cross-linking degree and decrease in negative surface charge, but only until the TFC membranes prepared with PK substrate coated with 1 mL CNT dispersion (TFC-1, TFC-1 (0.4/0.02), TFC-1 (1/0.05), and TFC

-1 (4/0.2)). For the membranes prepared with higher CNT coating amounts, lower cross-linking degrees were observed but the surface zeta potential of the membranes were all observed to be positive. It can be said that during the IP process, the CNT intermediate layer influenced the MPD storage and release, thus MPD's interaction with TMC, whose carboxyl groups provide the PA its characteristic negative charge upon hydrolysis, was also affected. Granted that the CNT intermediate layer could detrimentally affect the MPD absorption and storage, the heightened MPD release rate could allow more interaction between MPD and TMC, resulting in higher cross-linking degree and less presence of hydrolyzable carboxyl groups, effectively lowering the negative surface charge of the membrane.

Based on the aforementioned results, it is evident that the transition of PA morphology caused by the CNT interlayer significantly influences the PA structure and surface properties, as also demonstrated by earlier studies [138, 208]. Understanding the role of CNT interlayer in PA formation is of vital importance for achieving precise modulation of PA morphology, and this aspect will be thoroughly discussed in the following section.

2.3.3. New insights into the PA morphology transition

As disclosed in previous section, an interesting transition of the rough structures on PA was observed for the TFC membranes having different amount of CNT interlayers, which means that the CNT interlayer might have induced some competitive effects among several factors in shaping those rough features, which do not show a proportional change in PA morphology with increasing the CNT loading amount. Earlier studies have shown that IP process used in this work is MPD-diffusion controlled [210, 211]. It has also been shown that the PA morphology can be effectively regulated by manipulating the sustained supply or release rate of IP monomer [212-214]. Therefore, understanding the way of MPD storage and the release rate on various substrates is of vital importance to interpret the transition of PA morphology.

Based on this, the MPD storage capacity and release rate on different substrates were determined using a UV method widely reported in literature [141, 205, 215], and results

are shown in **Figure 2.15a**. The pristine PK substrate exhibited the highest MPD storage capacity of ~1.57 g/m^2 and the lowest MPD release rate of ~0.59 g L^{-1} min^{-1} (**Figure 2.15a**). This is because the pristine PK substrate exhibited an excellent surface hydrophilicity with surface pore size around 150 nm, the MPD solution could easy penetrate into a deeper position of PK, leading to a high storage capacity of MPD (**Figure 2.15b**). Similarly, due to the hydrogen bonding between the repeated carbonyl groups of the PK polymer and MPD molecules, the MPD molecules were less easy to release [207], resulting in a low MPD release rate. For the corresponding PA morphology, the control PA layer (TFC-C) showed a surface feature of nodular and ridge-and-valley structure which are typical characteristics for low MPD release case. Moreover, the TFC-C membrane exhibited a similar overall profile with the underlying PK substrate, suggesting that the PA formed along the fibrous structure of PK. This observation agreed with the earlier reported work attributing it to the deep PA intrusion in a microfiltration substrate with large pore size [138]. Although the PK substrate could provide sufficient MPD supply for the PA formation, the IP reaction was still forced to occur inside of the PK due to the reduced release tendency, resulting in a similar overall profile of PA with PK.

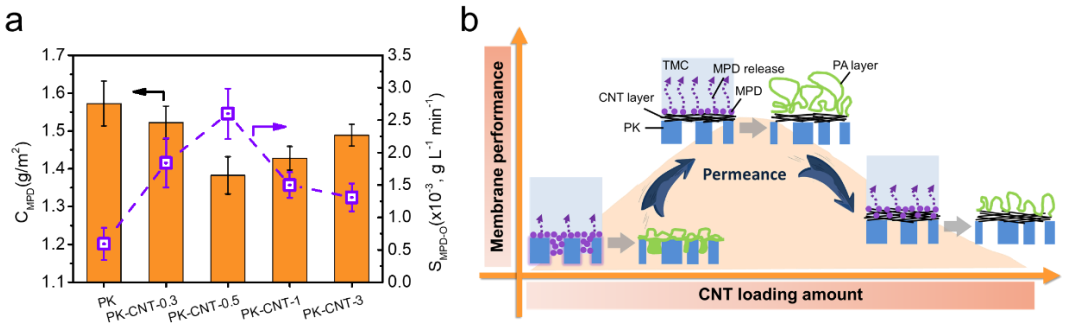

Figure 2.15 (a) MPD storage capacity (C_{MPD}) and release rate ($S_{MPD\text{-}O}$) on PK and PK-CNT substrates; (b) Mechanism of PA formation based on the MPD storage and release influenced by the CNT loading amount.

For the growing nodular and leaf-like structure on TFC-0.3 and TFC-0.5 membrane, it could be attributed to a reduced but still sufficient MPD supply and increased MPD

release rate during IP reaction which were shown in **Figure 2.15a**. As increasing the CNT loading amount up to 0.5, the MPD storage capacity decreased to around 1.38 g/m^2 and the release rate increased to ~2.60 $g\ L^{-1}\ min^{-1}$. During the CNT coating stage, the membrane surface became hydrophobic with reduced surface pore size, resulting in less penetration of MPD solution. Additionally, the increased CNT layer thickness weakened the influence of underlaying PK on the diffusion of MPD molecules, leading to a decrease in MPD storage capacity and an increase in MPD release rate (**Figure 2.15b**). From the point of view of IP reaction, although the MPD supply reduced, the higher release rate increased the encounter between MPD and TMC molecules, leading to a promotion of PA growth with the nodular and ridge-and-valley structure gradually becoming larger to ridge-and-valley and leaf-like structure. In particular, when the CNT loading amount reached 0.5, the multi-layered PA structure appeared (**Figure 2.8k**). The appearance of this multi-layered PA is mainly due to the sufficient MPD supply and the continuous growth of PA due to the penetration of MPD through the nascent PA film [212, 216]. This result also suggests that although a certain amount of CNT can lead to a decrease in MPD storage, it is still enough to sustain the IP reaction in a given time, generating a PA layer with abundant rough structures.

Conversely, further increasing the CNT loading amount, a retreat of leaf-like structure was observed for TFC-1 and TFC-3 with the reduction of surface roughness. Correspondingly, an increased MPD storage capacity and a decreased MPD release rate were obtained, as shown in **Figure 2.15a**. The reason for the turning points in MPD storage capacity and release rate is that the excessive CNT loading amount led to an over stacking between multiple CNT layers, which increased the specific surface area of the overall CNT interlayer and subsequently enhanced the adsorption of MPD aqueous solution (**Figure 2.15b**). It is because of the changes in MPD storage and release rate that the surface roughness values and structure of the PA were observed to vary with CNT loading amount in the intermediate layer.

It is worth noting that other classic explanations, such as confined nanobubbles foaming and heat-intensified interface instability, are also considered to play a part in shaping the rough feature of PA. However, the PA structure and morphology can never

be fully explained by only one of these conceptions, but instead as a synergy or competition of several factors. For example, ingenious experiments had confirmed the contribution of confined nanobubbles release on shaping the rough structure of PA with proposing a positive correlation between the nanobubbles release and the roughness. However, this explanation cannot match well with the changes of PA morphology caused by CNT interlayer in this work, because the nanobubbles release should be more confined at a thicker CNT interlayer and should result in rougher PA morphology. Hence, the initial stage of how MPD and TMC molecules encountered with each other before the nanobubbles forming was valued, a stage that must happen and cannot be ignored in any explanations. In summary, there are various methods for PA morphology regulation, but understanding the underlying mechanism still remains as a challenge

2.3.4. RO Performances of CNT-interlayered TFC membranes

The performance of the pristine and CNT-interlayered TFC membranes were tested in RO operation. Only TFC-0.5, TFC-1, and TFC-3 were compared with the pristine TFC-C membrane. **Figure 2.16** shows the pure water permeability (A) and NaCl rejection of the TFC membranes. All TFC membranes with CNT intermediate layer exhibited increased water permeability, in comparison with the pristine TFC membrane (TFC-C). The pristine TFC membrane demonstrated pure water permeability of 1.31 L m^{-2} h^{-1}/bar, and as an effect of the intercalation of the CNT intermediate layer, the A value became 1.60 (TFC-0.5), 2.43 (TFC-1), 1.56 (TFC-3) L m^{-2} h^{-1}/bar (**Figure 2.16a**). The increase in permeability is mainly attributed to the role of the CNT intermediate layer as a gutter layer, which shortens the transport distance within the PA selective layer, as well as a facilitator of the PA formation during IP, which resulted in PA selective layers with larger filtration area [60]. However, the higher CNT coating thickness of the TFC-3 membrane also resulted in higher transport resistance, which retarded water permeability. All TFC membranes exhibited outstanding NaCl rejection of over 97%, regardless of the presence or absence of the CNT intermediate layer (**Figure 2.16a**).

An application of less negatively-charged or positively-charged membranes is its

ability to retain and concentrate NH_4^+ in solution. It was previously established that, for NH_4^+ rejection and concentration, the surface charge and cross-linking degree of the membrane could play a crucial role [198]. Specifically, a less negatively-charged or positively-charged TFC membrane with less unreacted carboxyl groups might be more effective at rejecting NH_4^+ compared to the conventionally negatively charged pristine TFC membrane. Thus, the RO performance of the TFC membranes using 400 mg L^{-1} NH_4^+ from NH_4Cl as feed solution was evaluated and shown in **Figure 2.16b**. All TFC membranes exhibited similar permeance with the pure water permeability values. It is noticeable, however, that the TFC membranes with CNT intermediate layer have increased NH_4^+ rejection, particularly the neutral charged TFC-1 (95.2%) and positively-charged TFC-3 (96.0%).

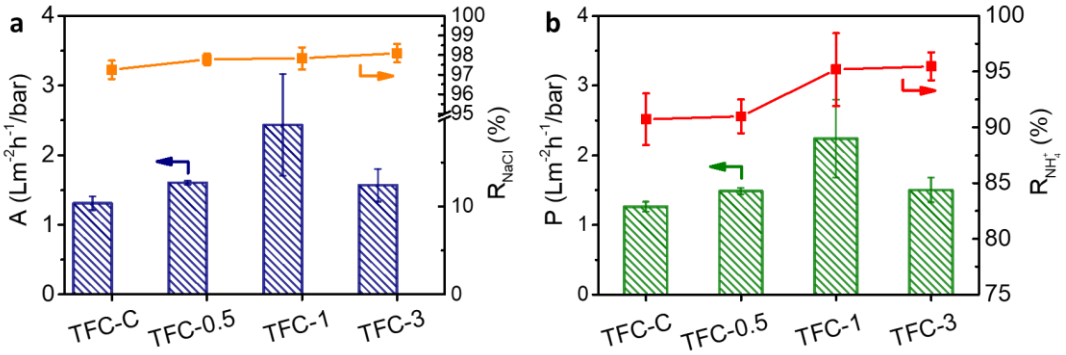

Figure 2.16. RO filtration performance of TFC membranes. (a) Pure water permeability (A) and NaCl rejection (R_{NaCl}) determined using deionized water and 2000 mg L^{-1} NaCl as feed solutions, respectively; (b) permeance (P) and NH_4^+ rejection (R_{NH4+}) determined using 400 mg L^{-1} NH_4^+ from NH_4Cl as feed solution.

2.3.5. Antifouling performances of CNT-interlayered TFC membranes

Regulation of the membrane surface charge has also been found as a useful method to improve the fouling resistance of membranes [197]. Previously, development of fouling-resistant membranes mainly focused on the surface hydrophilization of membranes [217-219]; however, fouling is regulated by other factors aside from the membrane surface hydrophilicity, such as surface charge and roughness. Thus, in this

work, the fouling propensity of the TFC membranes prepared in this work were evaluated using static adsorption and dynamic filtration.

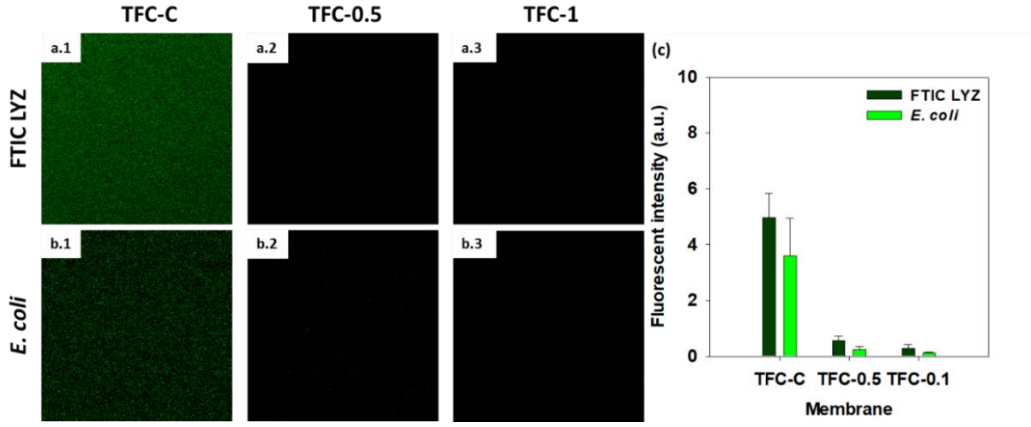

Figure 2.17. Confocal laser scanning microscope images of the TFC membranes after incubation in (a) fluorescently labeled isothiocyanate-conjugated lysozyme (FTIC LYZ) and (b) *E. coli*; (c) Fluorescent intensity values calculated using ImageJ software.

Static adsorption of positively-charged model protein foulant LYZ, was first conducted to demonstrate the fouling resistance of the TFC membranes. **Figure 2.17a.1-3** show the confocal laser scanning microscope (CLSM) images of the TFC, TFC-0.5, and TFC-1 membranes, respectively, after immersion in a PBS solution (pH 7.4) containing 20 mg L^{-1} fluorescent LYZ (FTIC LYZ). At pH 7.4, LYZ is positively-charged, thus it was somehow expected that the pristine TFC-C membrane suffered from the highest attachment of the fluorescent protein, compared with the TFC membranes with CNT intermediate layer (TFC-0.5 and TFC-1). The lower FTIC LYZ attachment on both TFC-0.5 (0.56 a.u.) and TFC-1 (0.30 a.u.) compared to TFC-C (4.98 a.u.) could be attributed to the less negative membrane surface charge (**Figure 2.17c**), resulting in weaker electrostatic attraction between the membrane surface and the positively-charged protein. Similar static adsorption behavior was observed for *E. coli*. **Figure 2.17b.1-3** show the CLSM images of the membranes after incubation in *E. coli*, and the corresponding fluorescent intensity values are shown in **Figure 2.17c**. The pristine TFC membrane showed the highest bacterial adhesion among all membranes (3.66 a.u.), while the neutral charged TFC-1 membrane (0.13 a.u.) hardly showed any

bacterial adhesion. The surface charge of the TFC-1 membrane is close to zero, thus there was no electrostatic attraction between the membrane and the charge-bearing *E. coli*.

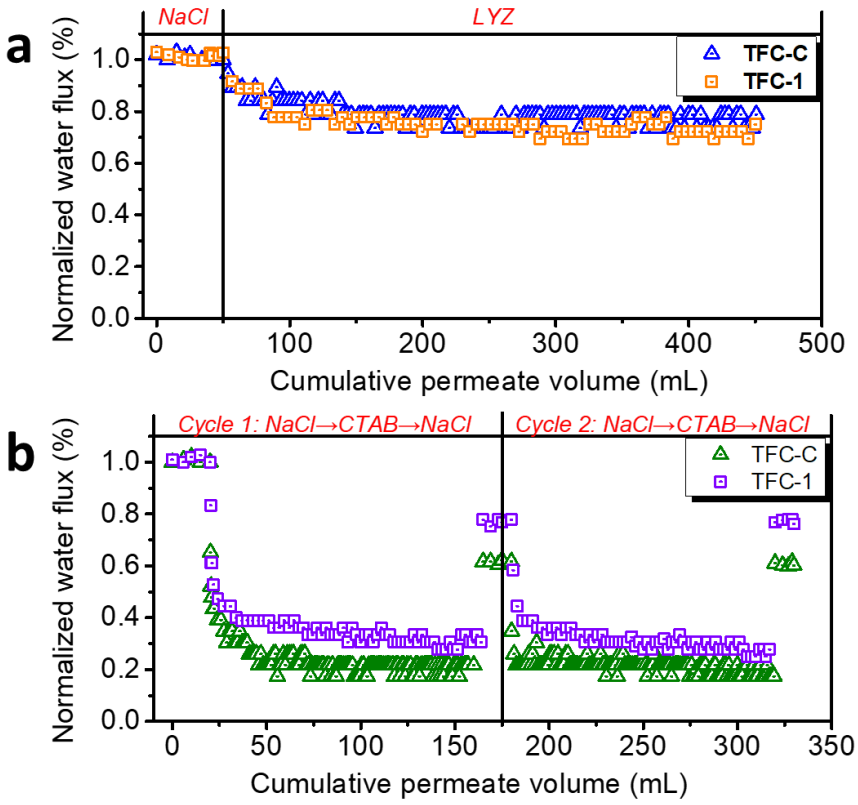

Figure 2.18. Dynamic filtration results of TFC-C and TFC-1 using model foulants (a) LYZ and (b) CTAB. 200 mg L^{-1} solutions of the model foulants were used as the feed solutions.

Dynamic fouling filtration was performed in this study using two positively-charged organic model foulants LYZ and surfactant CTAB to provide confirmation of the fouling control of the TFC membranes. The data shown in **Figure 2.18a** and **2.18b** correspond to the filtration results using feed solutions containing 200 mg L^{-1} of LYZ and CTAB, respectively. In **Figure 2.18a**, there was no discernable difference in the filtration performances of TFC-C and TFC-1 membranes. Both membranes experienced flux decline of around 20% until the end of the operation. This was different from the results of the static protein foulant adsorption results discussed earlier (**Figure 2.17a**). This could be attributed to the similar hydrophilic property of both

membranes, and the increased roughness of the TFC-1 (**Table 2.3**), which offset the absence of electrostatic attractions between the TFC-1 membrane surface and the protein brought about by the membrane's neutral charge [220]. Using a smaller positively charged surfactant molecule, CTAB, as the model foulant, dynamic filtration results with two filtration cycles were shown in **Figure 2.18b**. After replacing the feed solution from 2000 mg L^{-1} NaCl to 200 mg L^{-1} CTAB, both TFC-C and TFC-1 membranes experienced severe flux decline of 35% and 20% from the initial flux, respectively. Membrane performance further decreased to approximately 30% (TFC-1) and 20% (TFC-C) of their respective initial performances. Replacing the feed solution back to 2000 mg L^{-1} NaCl resulted in flux recovery to 75% and 60% of the initial flux of the TFC-C and TFC-1 membranes, respectively. Similar performance was observed during the second filtration cycle (**Figure 2.18b**).

2.4. Summary

In this work, CNT were successfully introduced to tailor the surface properties of PK substrate by forming a coating layer atop. Compared to other traditional modification methods, the coating of CNT layer is more flexible in adjusting the surface pore size from ~150 nm to ~20 nm. The hydrophilicity of PK surface changed from hydrophilic to slightly hydrophobic after coating CNT layer due to the reduced surface pore size and the hydrophobic nature of CNT. The CNT interlayer facilitated the PA formation by expediting the release of IP monomers, reducing the interaction between PK and the monomers. Nevertheless, excessive CNT loading could lead to the retreat of large leaf-like structures, which are essential for achieving high performance.

Moreover, the CNT interlayer was demonstrated to effectively regulate the surface charge of PA as it influenced the PA cross-linking. With a certain CNT interlayer thickness, the intercalated TFC membrane exhibited a neutral property under all pH condition, and this neutral characteristic did not change with changing the IP monomer concentrations. A correlation between the PA cross-linking degree and surface zeta potential measurement was drawn, proving that the CNT intermediate layer could not only regulate PA formation, but also the surface charge.

The performance of the membranes was tested in RO operation. The CNT-interlayered TFC membrane exhibited increased water permeability, while maintaining the NaCl selectivity, and increased selectivity and retention ability for NH_4^+, whose selectivity is typically influenced by surface charge and PA cross-linking degree. Static adhesion and dynamic filtration tests were performed to evaluate the TFC membranes' fouling control. After intercalation of the CNT intermediate layer, the TFC membrane showed less attachment of model foulants LYZ and *E. coli* due to less electrostatic attractions. Dynamic fouling filtration revealed that in actual RO operation, fouling is inevitable, but the CNT-interlayered TFC membrane exhibited better fouling resistance and performance recovery than the pristine TFC membrane.

Chapter 3 Organic solvent separation using carbon nanotube-interlayered thin film composite membrane

3.1. Introduction

Organic solvents are vital in industries like food processing, pharmaceuticals, and petrochemicals [78, 221-223]. They serve various purposes such as extraction, reactions, and separation processes. However, purifying the desired product and recovering the solvents present challenges for industries [5].

To improve efficiency, reduce waste, and minimize environmental impact, methods including distillation, extraction, adsorption, and membrane processes have been developed for solvent recovery and purification [224]. Among them, the pressure-driven membrane separation is an energy-efficient and environmentally-friendly approach with small footprint that enables substance separation without phase changes [225, 226]. It has shown promise for macromolecular product purification and solvent recovery.

Organic solvent nanofiltration (OSN) selectively separates larger solutes from organic solvents based on the size or other properties using membranes with specific pore sizes. As its use with organic solvents grows, there is a need for high-performance solvent-resistant membranes [227]. Conventional polymeric membranes used in water treatment are not suitable for organic solvent separation, creating a demand for the development of solvent-resistant membranes [75, 228, 229]. Thin-film composite (TFC) polyamide (PA) membrane, consisting of a substrate and PA selective layer, is one of the most popular membrane type used in membrane separation processes [62]. With using the solvent-resistant materials, the TFC membranes are possible to apply to OSN application.

Research works have been done to improve the TFC membrane performances. The carbon nanotube (CNT)-interlayered TFC membrane is one of the novel membrane

types that have been previously applied to OSN application [32, 58, 230]. However, these reported CNT-interlayered TFC membranes share a high molecular weight cut-off (MWCO) range from 250 to 300 g/mol, which limits their further application in separating molecules with molecular weight less than 200 g/mol. Thus, reducing the MWCO of CNT-interlayered TFC membrane in OSN is high needed for better functioning the CNT interlayer in permeance enhancement.

Previous work (Chapter 1) in this study has well investigated the function of CNT in facilitating the PA formation with high cross-linking degree. Thus, based on the previous work, the CNT-interlayered TFC membrane was further examined in OSN process for the removal of small molecules with molecular weight less than 200 g/mol. A series of triple-layered TFC membranes with CNT loading amount from 0 to 22.3 ug/cm^2 were prepared. The OSN performance of CNT-interlayered TFC membrane was fully investigated using dyes and drug molecules. The surface properties and chemical structure of PK substrate, CNT interlayer and PA selective layer were fully characterized. The long-term operation and solvent activation were performed to demonstrate the excellent separation capacity of TFC membrane.

3.2. Experimental

3.2.1. Materials

Polyketone (PK) polymer with a molecular weight of 200,000 g/mol was kindly supplied by Asahi Kasei Co., Ltd. (Japan). Single-walled carbon nanotubes (CNTs, length range: 5–30 μm, diameter: < 2 nm, 95%) was received from Aladdin Chemical Co., Ltd. (China). 1,3,5-benzenetricarbonyl trichloride (TMC, 99%) and M-phenylenediamine (MPD, 99%) were purchased from Sigma-Aldrich Co., Ltd. (Japan). Resorcinol, sodium dodecyl benzene sulfonate (SDBS), acetonitrile, methanol, acetone, ethanol, isopropanol and hexane were supplied by Fujifilm Wako Pure Chemical Co. Ltd. (Japan). Deionized (DI) water was obtained from water purification system manufactured by Merck Millipore Co., Ltd. (Germany). Ethylene glycol, 1,2-propanediol, glycerol (99.0%), D-(+)-glucose (＞ 98.0%), D-(+)- sucrose (＞ 99.0%)

were provided by Tokyo Chemical Industry (TCI) Co., Ltd. (Japan). The manufacture information and properties of the dyes used in this work were described in **Table 3.1**. All chemicals were used as received without further purification.

Table 3.1. Manufacture, molecular weight, chemical structure and charge property of the dyes and drug molecules used in this work.

Name	Manufacture	Mw (g/mol)	Chemical structure	Charge
4-Nitroaniline (4N)	Tokyo Chemical Industry (TCI)	138.1	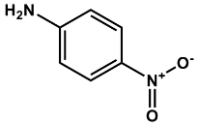	0
4-Hydroxyacetanilide (APAP)	Tokyo Chemical Industry (TCI)	151.2	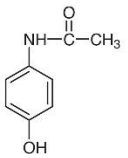	0
Sudan Orange G (SOG)	MP Biomedicals	214.2	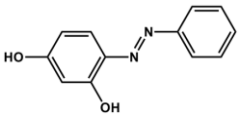	0
Chrysoidine G (CSG)	Sigma-Aldrich	248.7	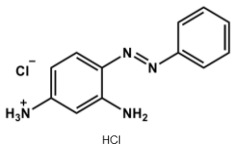	+
Acridine Orange (AO)	Fujifilm Wako Pure Chemical	265.4	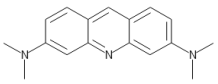	+
Basic Blue 17 (BB17)	Tokyo Chemical Industry (TCI)	305.8	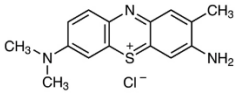	+
Methyl Orange (MO)	Tokyo Chemical Industry (TCI)	327.3	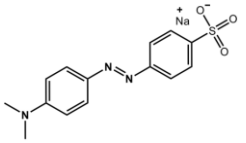	-
New Fuchsin (NF)	Tokyo Chemical Industry (TCI)	366.0	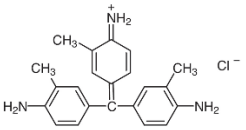	-
Curcumin (CCM)	Fujifilm Wako Pure Chemical	368.4	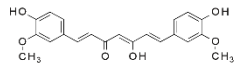	0

3.2.2. PK membrane casting

The home-made PK membrane fabricated by nonsolvent-induced phase separation (NIPS) [204] was used as the substrate in the work. Firstly, 10 wt% PK powder was dissolved in the mixture of resorcinol and DI water (35:65, wt%). The mixture was

stirred at 80℃ for at least 5 h to form a homogenous casting solution. After overnight degassing at 60℃, the PK solution was cast onto a clean glass plate with a casting gap of 400 μm. Then, the casting plate was immediately immersed into a precipitation bath of methanol/water (35:65, wt%) for 20 min before transferring into pure acetone and hexane and immersing for 20 min each to make sure the membrane was fully washed. Finally, the PK membrane was dried in the air and stored for further used.

3.2.3. Fabrication of the PK-CNT substrates and TFC membranes

To ensure the uniformity coverage of CNT layer, the CNT used in this work was dispersed in DI water with the help of SDBS surfactant before coating. Generally, 10 mg SWCNT and 100 mg SDBS were dispersed in 100 mL DI water. The mixture was dispersed using prob-sonication (SFX 250, BRANSON, Mexico) for 8 h before centrifuged at 10,000 rpm for 1 h. The supernatant with a concentration of 0.098±0.011 mg/mL was collected and used as the final CNT dispersion. The PK-CNT substrate was fabricated by filtrating a certain amount of CNT dispersion (0.1 ~ 3 mL CNT dispersion diluted to 80 mL using DI water before filtration) onto the PK membrane (effective membrane area: 12.56 cm^2) using vacuum filtration method. After filtration, the PK-CNT substrate was dried under 45℃ in an oven for at least 4 h before stored under room temperature for further use. The PK-CNT substrates were labelled as PK-CNT-*x* which *x* represents the corresponding volume of CNT dispersion during filtration. The corresponding loading amounts of CNT on the membrane surface can be checked in **Table 2.1** in Chapter 2.

The TFC membranes used in this work were fabricated through IP using MPD and TMC following the reported method. Briefly, the PK-CNT substrate was fixed on a glass plate with CNT side face to the air. Then, 2 wt% MPD aqueous solution was induced onto the CNT side. After prewetted for 2 min, the excess MPD solution was poured out and the underlying PK-CNT substrate was gently dried using an air brush with a pressure below 0.1 MPa. Subsequently, 0.1 wt% TMC solution in hexane was poured onto the CNT side to react with the MPD molecules for 1 min. After removing the excess TMC solution, the nascent TFC membrane was further cured at 60℃ for 10

min. The control sample was also fabricated following the same IP procedure except using the pristine PK membrane as substrate. The fabricated membranes having different CNT loading amount were labelled as TFC-*y* which *y* represents the CNT filtration amount during fabricating the CNT interlayer. Unless stated otherwise, all TFC membranes were fabricated with an MPD concentration of 2 wt%. All TFC membranes were preserved in DI water at 4℃ for further use.

3.2.4. Membrane characterization

The membrane surface morphologies were observed using field-emission scanning electron microscopy (FE-SEM, JSF-750F, JEOL, Japan) and atomic force microscopy (AFM, SPA-400, Hitachi, Japan). The *Image J* software was applied to analyze the surface pore size and porosity changes of PK membrane before and after CNT deposition based on SEM images, and the membrane surface roughness was analyzed by *Spisel* software based on AFM images. The cross-sectional structure of TFC membrane was observed using transmission electron microscopy (TEM, JEM-2100F, JEOL, Japan). The element composition was detected using X-ray photoelectron spectroscopy (XPS, JPS-9010MC, JEOL, Japan) with monochromatic Mg Kα excitation. Fourier transform infrared spectrometer (FTIR, Nicolet iS50, Thermo Fisher, USA) were applied to analyze the surface chemical composition. The overall pore size distribution was detected using a liquid-liquid displacement porometer (LLDP, LLP-1200A, Porous Material Inc, USA). The membrane was initially soaked in isopropanol prior to displaced by a specific testing liquid Galwick® (surface tension: 15.9 dynes/cm) in a pore size measurement. The membrane surface hydrophilicity was measured by a contact angle analyzer (WCA, DM-300; Kyowa, Japan) with a droplet volume of 2 μL. All samples were fully dried in an oven at 60℃ overnight before characterizations and all tests were performed at room temperature.

3.2.5. Evaluation of molecular weight cut-off (MWCO) of TFC membranes

The MWCO of TFC membranes were measured in two ways: one was tested in water phase with using sugar and other neutral molecules as solute, and the other was

evaluated in methanol solvent with dyes as solute. For the sugar one, according to the reported method [159, 225], ethanol (46.1g/mol), ethylene glycol (62.1 g/mol), 1,2-propanediol (76.1 g/mol), glycerol (92.1 g/mol), glucose (180.2 g/mol) and sucrose (342 g/mol) with feed concentration of 1000 mg/L in water were filtrated through the membrane at 5 bar. The concentration of solute in permeate was determined using a total organic carbon analyzer. (TOC, TOC-VCSH, Shimadzu, Japan). For the MWCO measured using dyes, several dye solutions with concentration of 50 mg/L in methanol were used as the feed, and were filtrated through membrane at 5 bar. The dye concentration was calculated based on the calibration curve of dye concentration versus absorbance determined by the UV-vis spectrophotometer. The physic-chemical properties of dyes used in this work were listed in **Table 3.1**.

3.2.6. OSN performance evaluation

The OSN test was performed in a cross-flow NF setup with an effective membrane filtration area of 7.065 cm^2 [60]. An equilibrium time of 1h under 6 bar was allowed before reaching to a stable permeance. The pure organic solvent permeance was tested for 1h with a cross-flow rate of 10 mL/min before switching the pure organic solvent to the corresponding dye solution with a concentration of 50 mg/L as the feed. The permeate was collected and its weight gain was recorded by an electronic balance interfaced with a laptop. The solvent permeance (P, L m^{-2} h^{-1}/bar, LMH/bar) and dye rejection (R, %) could be calculated based on the following equations:

$$P = \frac{M}{S \times t \times \rho \times p} \tag{3-1}$$

where M (g) is the weight gain of permeate within a certain testing period; S (m^2) is the effective membrane area; t (h) represents the filtration time; ρ (g/L) is the density of permeate; p (bar) is the operation pressure which is fixed at 5 bar during the testing.

$$R = \left(1 - \frac{C_p}{C_f}\right) \times 100\% \tag{3-2}$$

where C_p and C_f are the dye concentrations of permeate and feed solution, respectively.

3.2.7. Dimethylformamide (DFM) activiation

To evaluate the chemical stability of the TFC membranes, solvent activation was

conducted in this work. Due to the polar nature of the PA layer, dimethylformamide (DMF), a polar aprotic solvent widely used in pharmaceutical and chemical industries, was chosen as the activating solvent. The pristine (TFC-C) and CNT-interlayered (TFC-0.5) TFC membranes were immersed in DMF for 10 min at room temperature. After the DMF exposure, the membrane performance was evaluated and compared with non-solvent activated membranes.

3.2.8. Long-term stability evaluation

The stability of the best-performing TFC membrane was also evaluated during a long-term filtration. 50 mg/L curcumin (CCM) in methanol was used as the feed, and the testing conditions were similar as the earlier tests.

3.3. Results and discussions

3.3.1. Characterization of PK and PK-CNT substrates

The PK and PK-CNT substrates were successfully prepared using nonsolvent-induced phase separation and filtration deposition methods, as shown by the morphology of the PK-based membrane substrates imaged using FE-SEM, as shown in **Figure 3.1**.

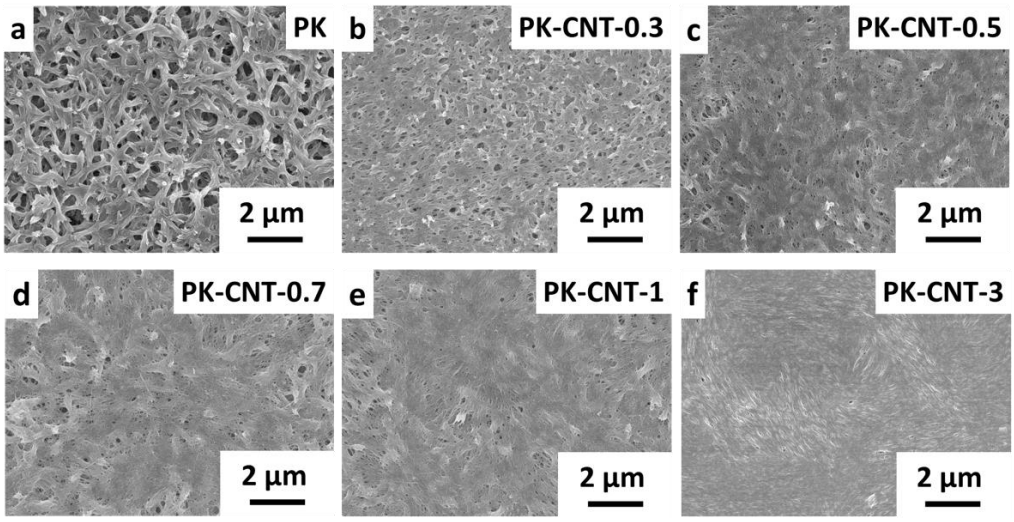

Figure 3.1. SEM surface morphology of PK and PK-CNT substrates.

It could be seen from these figures that as the amount of the CNT coating solution

increased, the coverage of the CNT layer on top of the PK substrate increased as well. The increased coverage was characterized by the decrease in the number of visible pores on the membrane substrate surface, with the PK substrate coated with 3 mL of CNT dispersion (PK-CNT-3) having no distinguishable pores. It is quite noticeable from the FE-SEM images that a continuous CNT network was visible atop the PK substrate when the loading amount was at least 0.5 mL (PK-CNT-0.5).

Table 3.2. Properties of PK and PK-CNT substrates.

Membrane substrate	CNT loading amount (μg cm^{-2})	Root-mean-square roughness (nm)	Water contact angle (°) [a]	Surface porosity (%) [b]
PK	0	89.6±12.4	N/A	21.9±0.8
PK-CNT-0.3	2.23	49.5±3.3	83.7±2.1	23.1±1.5
PK-CNT-0.5	3.71	41.4±3.9	93.0±4.1	24.1±1.2
PK-CNT-1	7.43	34.4±2.7	88.4±5.5	18.4±2.8
PK-CNT-3	22.3	32.3±6.5	87.4±4.1	7.5±2.2

[a] Water contact was measured after the water droplet was in contact with membrane for 15 s.

[b] Surface porosity values were determined by using *ImageJ* software based on SEM images.

Other properties such as amount CNT loading amount (μg cm^{-2}), root mean square roughness, water contact angle, and surface porosity are shown in **Table 3.2**. The surface porosity analyses were conducted using computerized quantitative image analysis of SEM images. Interestingly, both PK and PK-CNT substrates exhibited very similar surface porosity percentages, ranging from 21.9 to 24.1%, except the PK-CNT-3. This suggests that the CNT layer effectively reduced the pore size without compromising the surface porosity. Unlike the intercalation of intermediate layers using nanoparticles or 2D nanosheets which might lead to pore clogging, CNT, with their large aspect ratio, were able to form a porous network through disordered stacking, preserving the high surface porosity of the substrate. However, too much loading amount also led to a sharp decrease in surface porosity (~7.5% for PK-CNT-3) because of the stacking between multiple CNT layers. It is worthy to mention that the surface characteristics of small pores and high porosity have been shown to be advantageous

for the IP reaction by storing and releasing IP monomers uniformly. Hence, it is reasonable to assume that these surface features continue to positively influence the subsequent IP reaction.

The chemical composition of PK and PK-CNT substrates were analyzed by using XPS, and spectra were shown in **Figure 3.2**. In the wide-scan XPS spectra (**Figure 3.2a**), all samples gave rise to strong peaks at 284.5 and 533.5 eV, corresponding to the binding energy of C 1s and O 1s respectively. Besides, the intensity of C 1s peak increased with increasing the CNT loading amount, while the O 1s peak decreased accordingly (**Figure 3.2f** shows the C/O ratio values). Considering PK is the main source for providing oxygen element, this tendency indicates that the PK surface was gradually covered by CNT layer, turning its surface property closer to the property of CNT.

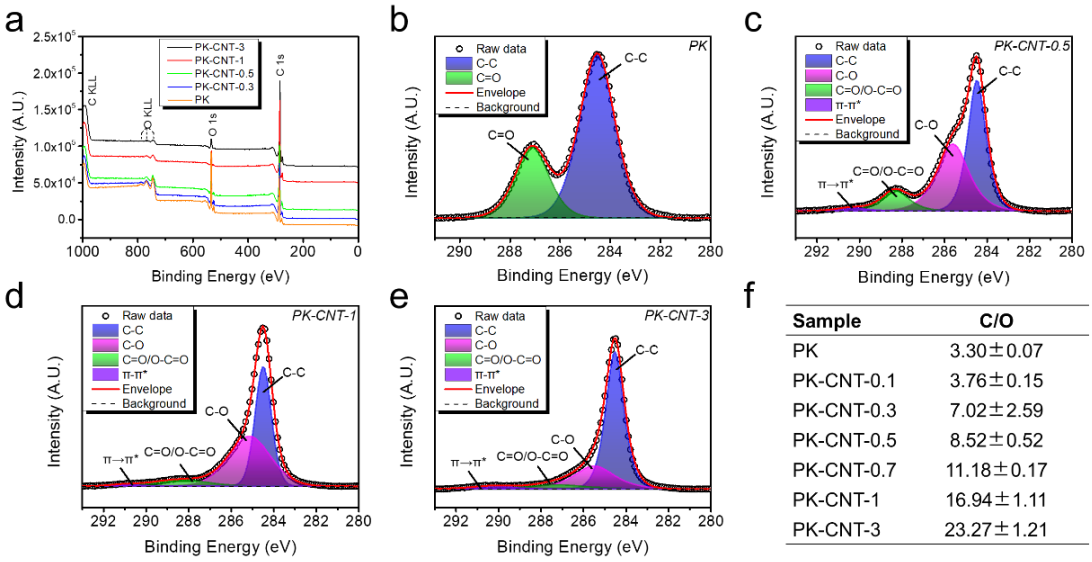

Sample	C/O
PK	3.30±0.07
PK-CNT-0.1	3.76±0.15
PK-CNT-0.3	7.02±2.59
PK-CNT-0.5	8.52±0.52
PK-CNT-0.7	11.18±0.17
PK-CNT-1	16.94±1.11
PK-CNT-3	23.27±1.21

Figure 3.2. (a) Wide-scan XPS spectra of PK and PK-CNT substrates; High-resolution deconvolution peaks of C 1s spectra of PK (b), PK-CNT-0.5 (c), PK-CNT-1 (d) and PK-CNT-3 (e); (f) C/O ratio of PK and PK-CNT substrates.

To further figure out the chemical composition of the membrane surface, high-resolution deconvolution of C 1s peaks was conducted for PK and PK-CNT substrates (**Figure 3.2b-e**). All the deconvoluted spectra showed a main peak at 284.5 eV which is attributed to the sp^3-hybridized carbon in C-C bond and the sp^2-hybridized carbon in

graphitic structure [231, 232]. Peak at 287.1 eV in PK spectra (**Figure 3.2b**) is attributed to the carbonyl (C=O) bond in the PK molecular chain. After depositing CNT layer atop, peaks at binding energy of 285.6, 288.5 eV attributed to the sp^3-hybridized carbon atoms at the CNT surface occurred (**Figure 3.2c-e**). These carbon atoms directly bond to functional groups such as hydroxyl groups (C-OH at 285.6 eV) and carboxylic acid (O-C=O at 288.5 eV, overlapped with C=O) groups [231-233], whose existence is attributed to CNT defects. With increasing CNT loading amount, the thickness of CNT layer became large, making the C=O bond in PK hard to detect, resulting in a decreased area of C=O bond. Similarly, the amount of defects on CNT surface lessened with increasing CNT loading amount, leading to a reduced area of C-O bond for the case of PK-CNT substrates. The XPS results confirm that the coated CNT layer gradually changed the chemical composition of PK surface, making it closer to the property of CNT surface.

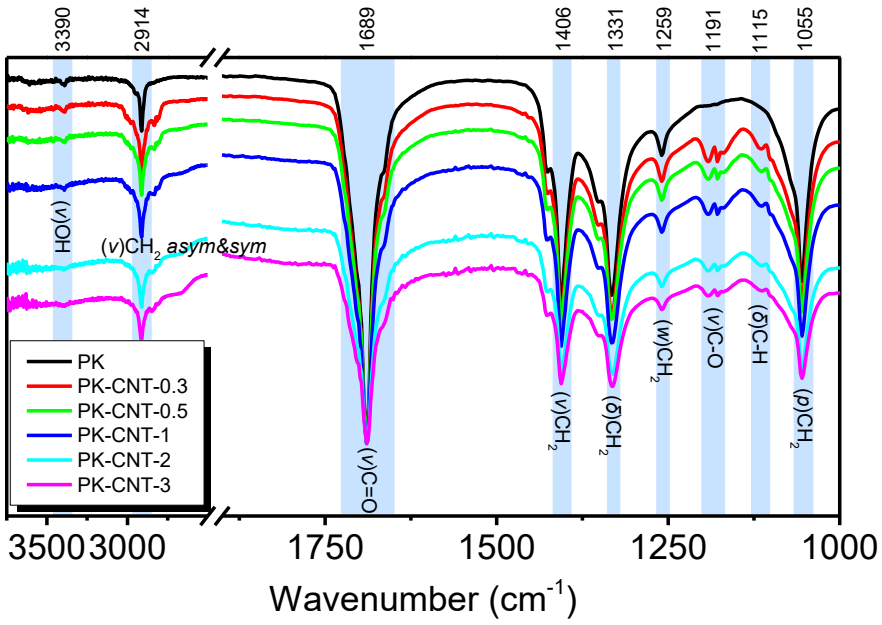

Figure 3.3. FTIR spectra of PK and PK-CNT substrates with CNT loading amount varied from 0.3 to 3. Variation types are reported in parentheses: *ν*: stretching; *δ*: bending; *w*: wagging; *ρ*: rocking; *asym*: antisymmetric mode; *sym*: symmetric.

The FTIR characterization were performed and results are shown in **Figure 3.3**. In the spectra of PK, a strong characteristic peak was found at 1689 cm^{-1} which

corresponds to the stretching of carbonyl (C=O) bond [234]. Other characteristic peaks appeared at 1406, 1331, 1259 and 1055 cm^{-1} correspond to the stretching, bending, wagging, and rocking attributed to CH_2 group, respectively. The peaks at 2914 and 3390 cm^{-1} respectively corresponded to the stretching of CH_2 and the stretching of OH because of keto–enol tautomerism. This result indicates that the PK substrate was successfully prepared through NIPS method without changing its original chemical structure.

The deposition of CNT layer led to lower intensities of the C=O bond at 1689 cm^{-1} and the CH_2 group at 2914, 1406, 1331, 1259 and 1055 cm^{-1}, while new peaks occurred in the series of PK-CNT spectra at 1191 and 1115 cm^{-1}, corresponding to the stretching of C-O bond (XPS data provided strong evidences) and the blending of the C-H bond on benzene ring. This result leads to conclude that the chemical structure of CNT was well-maintained during the deposition process.

3.3.2. Characterization of CNT-interlayered TFC membrane

First, to verify the occurrence of IP reaction, and to understand the chemical structure of the as-prepared PA layer, FTIR analyses were conducted and peaks were assigned referring to the possible molecular structure of polyamide [37]. In **Figure 3.4**, several characteristic peaks of polyamide were identified and labeled accordingly. A comparison of the spectra of substrate (refer to **Figure 3.3**) with those of TFC membranes revealed four unique peaks of PA layer appeared at 3309, 1608, 1539 and 1489 cm^{-1}. The peak at 3309 cm^{-1} was attributed to the stretching (v) of N-H bond [235]. The peak at 1608 cm^{-1} was associated with aromatic amide, and had been previously attributed to the deformation (d) vibration of N-H bond [236] and the ring stretching of C=C bond [37, 237, 238]. The peak at 1539 cm^{-1} was identified as the amide II bond in the amide group (-CONH-), which was an overlap of the bending (δ) of N-H bond and the stretching of C-N bond [239-241]. The amide I band (stretching of N-C=O) was identified at 1663 cm^{-1} [237, 239, 241] where an enhanced intensity was observed. The peak at 1489 cm^{-1} was assigned to the bending of -OH from the carboxylic acid groups (-COOH) which hydrolyzed from the unreacted acid chloride groups [35]. The

enhanced intensity of the stretching of C-O bond at 1190 cm^{-1} (overlapped with the C-O bond on CNT surface, refer to **Figure 3.3**) also confirmed the existence of -COOH group on the membrane surface. The FTIR results indicate that despite the surface properties of substrates have changed, a PA layer can smoothly generate. However, due to the complex overlapping between peaks, further quantitative analysis was still difficult.

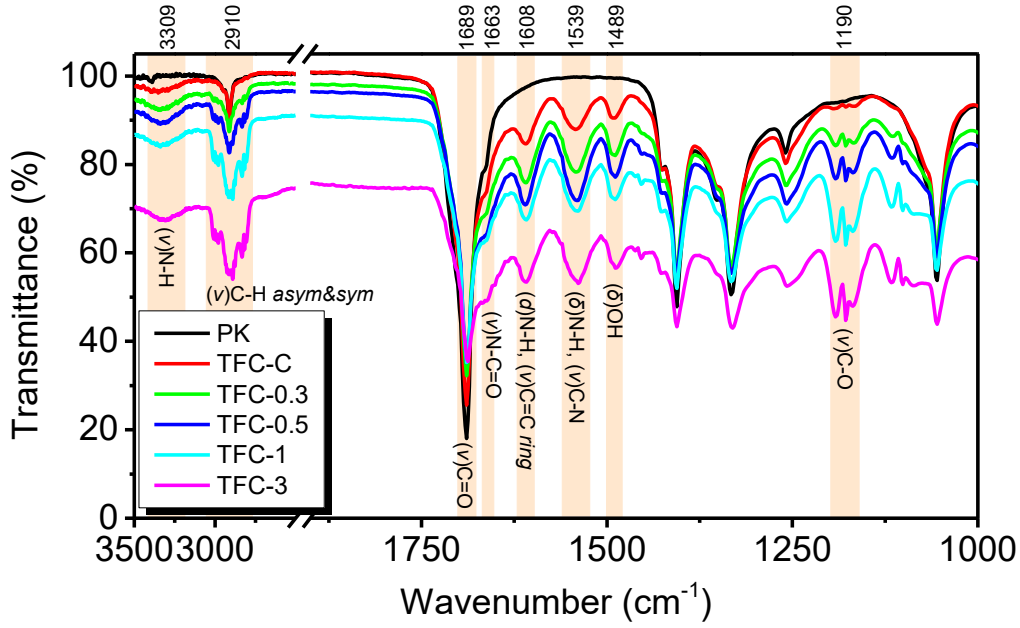

Figure 3.4. FTIR spectra of TFC PA membranes with CNT loading amount varied from 0.3 to 3. Variation types are reported in parentheses: *v*: stretching; *δ*: bending; *asym*: antisymmetric; *sym*: symmetric.

The influence of the CNT intermediate layer on the surface morphology of the PA selective layer of the TFC membranes are shown in **Figure 3.5**. The pristine TFC membrane (TFC-C) showed the typical ridge-and-valley and nodular structures characteristic of the PA layer (**Figure 3.5a**). However, upon the introduction of the CNT intermediate layer, it could be noticed that the ridge-and-valley structures evolved into larger leaf-like structures, and the nodular structures gradually turned into ridge-and-valley structures. The PA leaf-like structures could also be observed to overlap with each other, resulting in an apparent multi-layered structure. This change in PA structure was further corroborated by the cross-sectional FE-SEM and TEM images (**Figure 3.5f-**

o), which showed an increase in the apparent thickness of the PA layer due to the formation of multi-layered leaf-like structures. This phenomenon was observed from the morphological images of the membranes whose intermediate layers were prepared with CNT dispersion volumes lower than 1 mL. The membranes whose intermediate layers were prepared using higher CNT dispersion amounts (TFC-1 and TFC-3) showed a reduction in leaf-like structures and another emergence of nodular structures (**Figure 3.5e, j** and **o**). The formation mechanism of these PA structural phenomena was explained in detail in Chapter 2.

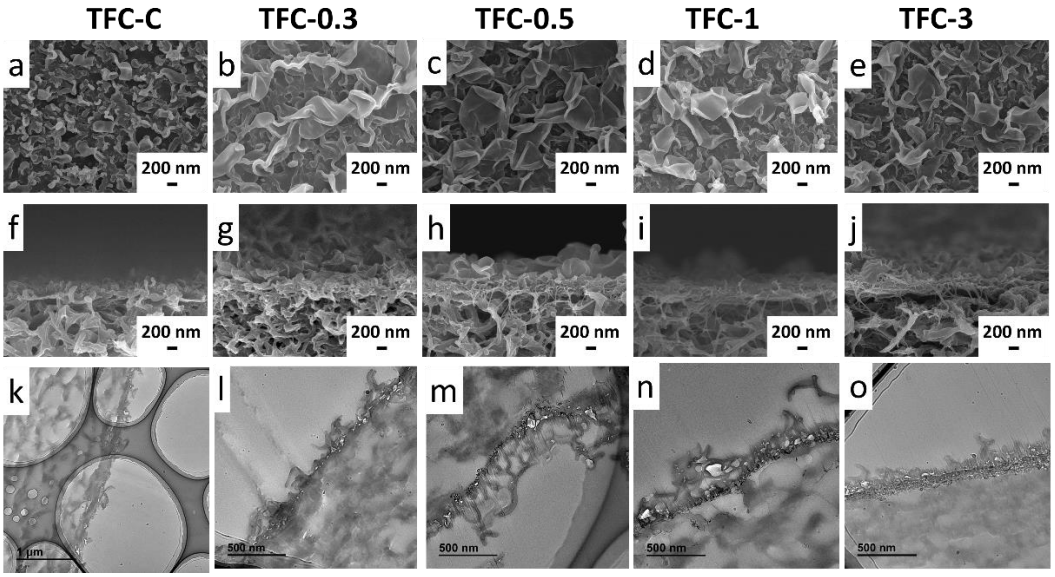

Figure 3.5. Surface and cross-sectional SEM images of pristine TFC-C membrane (a, f, and k) and CNT-interlayered TFC membranes (b, g and l for TFC-0.3; c, h and m for TFC-0.5; d, i and n for TFC-1; e, j and o for TFC-3).

Other surface properties of TFC membranes were listed in **Table 3.3**. The WCA values for all TFC membranes were around 70°. However, upon closer examination, a trend of first decreasing and then increasing WCA was observed at the turning point of the TFC-0.7 membrane. It has been demonstrated that the hydrophilicity of PA is highly related to its chemical composition and cross-linking degree. Thus, XPS characterizations was conducted to analysis the element composition and cross-linking degree of the PA layer. The cross-linking degree was calculated according to a reported

method [242], and results were listed in **Table 3.3**. The initial increase in the cross-linking degree from ~0.48 (TFC-C membrane) to ~0.68 (TFC-0.7 membrane) indicated that fewer carboxyl groups remained on the surface, theoretically leading to an increase in WCA. However, according to the Wenzel model, an increase in roughness for hydrophilic surface can result in a more hydrophilic property [243], and this effect could counteract the increase in WCA. As a result, the two opposite tendencies eventually led to little change in the WCA. Similar situations were also observed for the TFC-1 and TFC-3 membranes, where the decreased surface roughness and cross-linking degree resulted in a relatively stable WCA.

Table 3.3. Surface properties of the fabricated TFC membranes.

Membrane	Root-mean-square roughness (nm)	Water contact angle (°) [a]	Cross-linking degree
TFC-C	93.2±1.2	73.0±2.4	0.48±0.15
TFC-0.3	150±9	66.0±1.5	0.63±0.12
TFC-0.5	172±8	67.3±2.2	0.66±0.03
TFC-0.7	145±9	70.6±2.4	0.68±0.01
TFC-1	135±4	72.1±1.8	0.67±0.04
TFC-3	80.2±14	76.6±2.1	0.60±0.04

[a] Water contact was measured after the water droplet was in contact with membrane for 15 s.

3.3.3. OSN performances of the TFC membranes

To demonstrate the influence of the CNT interlayer and PA structure on the separation performance, The OSN performances of the TFC membranes were investigated. Methanol permeance values and rejections of several dyes were plotted against different CNT loading amounts (**Figure 3.6a**). The methanol permeance gradually increased from 1.61 L m^{-2} h^{-1}/bar to 5.34 L m^{-2} h^{-1}/bar as the CNT loading amount increased from 0 to 0.5, and then slightly decreased with further increases in loading amount. Notably, this significant increase in permeance did not come at the expense of rejection loss, as demonstrated by the MO and SOG rejection remained above 99.5% and 96.5%, respectively. According to the typical solvent transport model for PA films reported in Livingston's work [31], the relationship between the solvent permeances and the

solvent property combinations ($\frac{\delta}{\eta\, d^2}$, where δ is the Hansen solubility parameter of polar portion, η is solvent viscosity, and d is the molecular diameter) of the TFC-C and the optimal sample TFC-0.5 was linear (**Figure 3.6b**), indicating that the membranes are defect-free, and their transport properties fit well with the typical transport model.

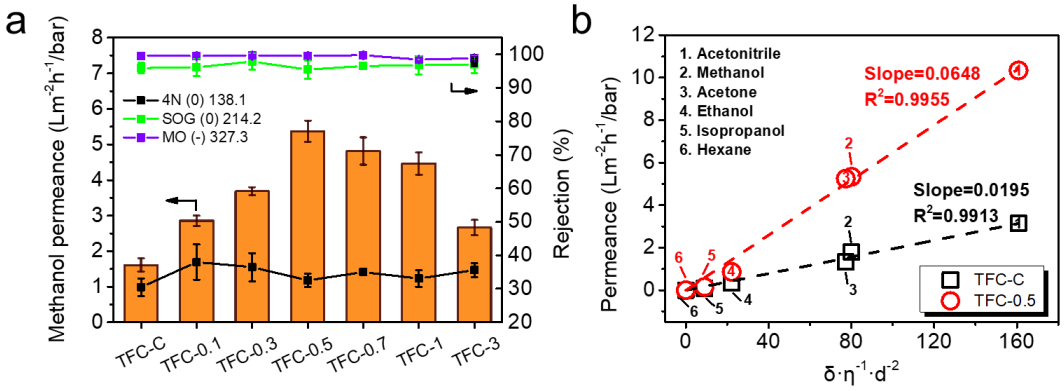

Figure 3.6. (a) Dye rejection performances of the TFC membranes having different CNT loading amount; (b) Plot of the solvent permeances against solvent properties.

The enhanced membrane performance can be attributed to both the CNT interlayer effect and the optimized PA structure resulting from the CNT layer. The gutter layer effect of the CNT interlayer, well-documented in the literature [135, 136], is one of the effective reasons for the permeance enhancement, as it facilitates solvent transport horizontally and shortens the transport distance within the less permeable PA layer. Additionally, the presence of the CNT interlayer alleviates PA intrusion into the substrate, leading to reduced resistance during solvent transport [138-140]. However, the extent of permeance enhancement is limited by the thickness of CNT layer, as an increase in the interlayer thickness leads to monotonic increase in transport resistance in the vertical direction. For example, in this study, the CNT layer reached its thinnest thickness and lowest transport resistance at a CNT loading amount of 0.5, resulting in the maximum gutter effect on permeance enhancement for the TFC-0.5 membrane. Beyond this point, further increases in the CNT loading amount led to decreased permeance due to the trade-off between the transport resistance in horizontal versus vertical direction [135]. The solvent permeance of the TFC-3 membrane was

approximately 50% lower than that of TFC-0.5, although it was still nearly 1.6 times more permeable than the control TFC-C membrane. Another reason for the increased permeance is the larger filtration area of PA layer resulting from the transition of PA morphology. As discussed earlier, the surface roughness of the PA layer increased during the transition from nodular to ridge-and-valley, and then to large leaf-like characteristics, providing a higher filtration area and resulting in a higher permeance of the TFC membrane. However, the excessive loading amount of CNT led to a large loss of large leaf-like PA structures and a relatively lower permeance for TFC-1 and TFC-3 compared to TFC-0.5.

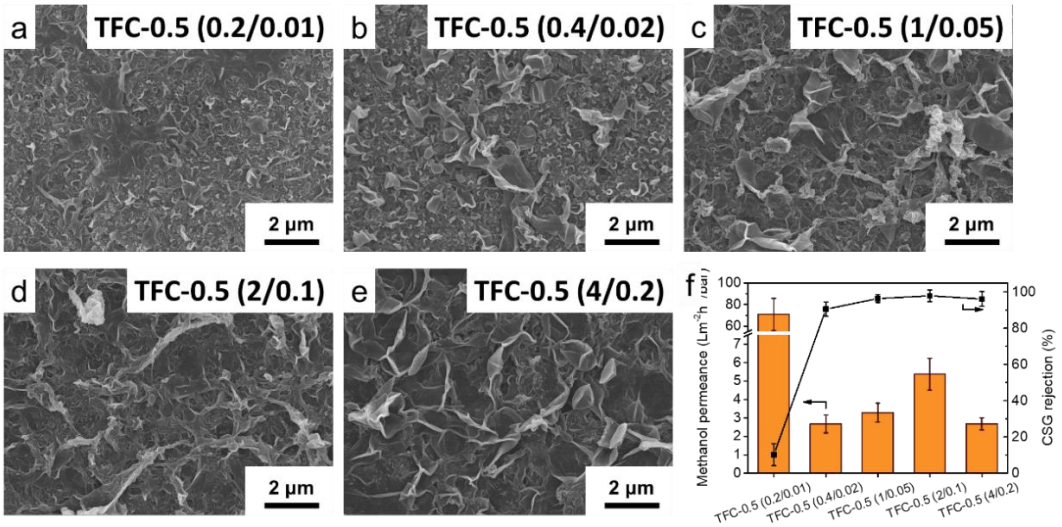

Figure 3.7. (a-e) Surface morphologies of TFC-0.5 samples prepared using different MPD/TMC combinations (The number after TFC-0.5 represents the MPD concentration used); (f) Effect of MPD concentration on performance of TFC-0.5 membrane.

The membrane performance of the TFC membrane with a CNT loading amount of 0.5 was further optimized by varying the MPD concentrations (from 0.2 to 4 wt%, with a fixed concentration ratio of MPD/TMC at 2/0.1). **Figure 3.7f** illustrates the influence of MPD and TMC concentration on membrane performance. A low MPD concentration of 0.2 wt% did not provide enough monomer content to ensure sufficient MPD supply during the IP reaction, resulting in defects in the generated PA film and unfavorable dye rejection values (less than 10% for positively-charged CSG dye). Increasing the MPD

concentration led to an enhanced IP reaction, forming a cross-linked PA film and increasing the rejections from ~90.5% to ~98.0%. Additionally, the increase in membrane permeance was attributed to the formation of large leaf-like PA structures, providing more filtration area during solvent transport (**Figure 3.7a-e** shows the morphologies of TFC-0.5 samples prepared using different MPD concentrations). However, excessive MPD concentration resulted in a PA layer with a much higher cross-linking degree (0.80±0.08), leading to reduced membrane permeance at the MPD concentration of 4 wt%. Therefore, the optimal TFC membrane fabrication condition was determined with using 2 wt% MPD and 0.1 wt% TMC.

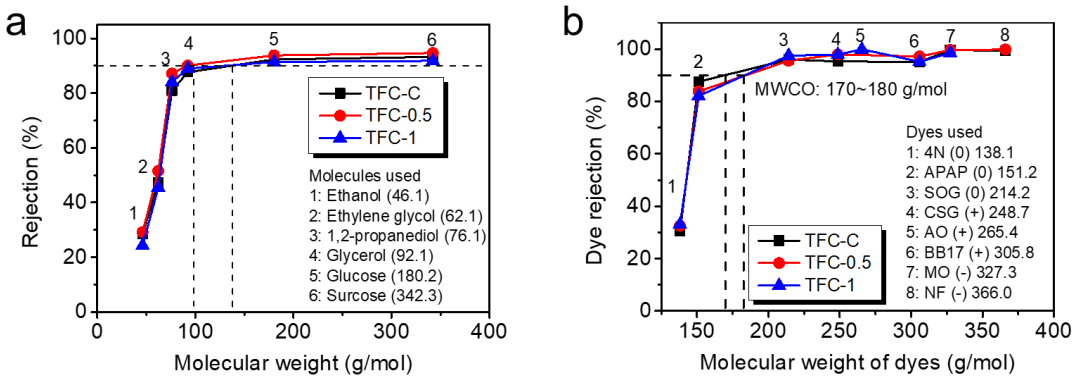

Figure 3.8 MWCO profile of TFC-C, TFC-0.5 and TFC-1 detected using sugar and other molecules in water phase (1000 mg/L) (a), and using dyes in methanol (50 mg/L) (b).

The molecular weight cut-off (MWCO) of the TFC-C, TFC-0.5, and TFC-1 membranes were estimated from the rejection of neutral sugar and other molecules in water phase (**Figure 3.8a**). Another MWCO evaluation was conducted using dyes with different charge properties in methanol solvent, as sugars are known to be insoluble in methanol, and the results are given in **Figure 3.8b**. The rejection values increased with the increase of molecular weight (**Figure 3.8a**), indicating that the TFC membranes are quite dense. From the rejection values, the MWCO of three TFC membranes varied in a narrow range from 98 to 138 g/mol, with the MWCO of TFC-0.5 (~98 g/mol) being slightly lower than the other two TFC membranes (~138 g/mol). However, all TFC membranes had low rejection (~30%) of 4-nitroaniline (4N) molecule in methanol

(**Figure 3.6a**), even though its molecular weight (4N: 138.1 g/mol) was quite close to the membrane's MWCO. This disagreement in MWCO values could be attributed to the use of different solvents during the two MWCO measurements (**Figure 3.6b**), and the different behaviors of the membrane surface when in contact with different solvents, i.e., methanol and water [60]. Despite this, all results demonstrate that the TFC membranes owned dense PA layers, and the advantage of having a dense PA layer and a small MWCO is particularly beneficial for OSN applications, especially for large-scale applications such as Max-Dewax process [229].

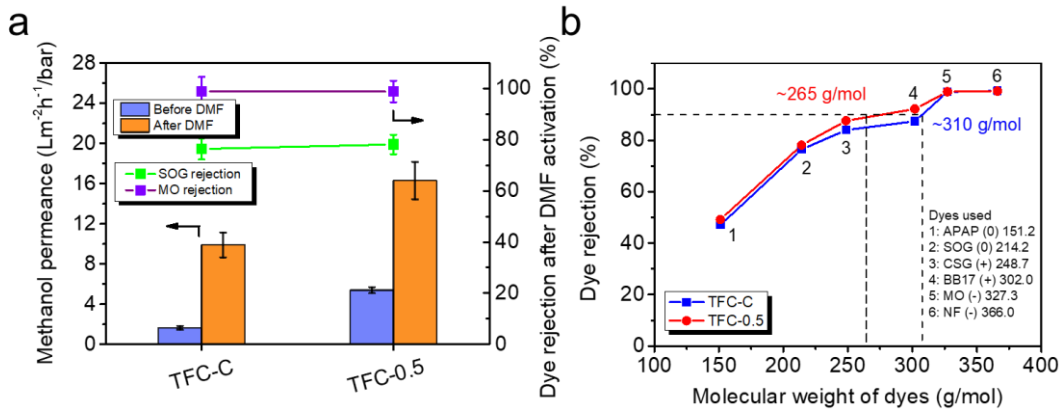

Figure 3.9. (a) Dye rejection performances and (b) MWCO profile of TFC-C and TFC-0.5 detected using dyes in methanol (50 mg/L) after 10-min DMF activation. See **Table 3.1** for the detail information of dyes and drug molecules used in this work.

The methanol permeance and rejection against MO and SOG of TFC-C and TFC-0.5 membranes before and after solvent activation were presented in **Figure 3.9**. As shown in **Figure 3.9a**, after exposure to DMF, there was a significant (approximately 3 to 4 times) increase in the methanol permeance for both membranes. Comparing the dye rejection values of the membranes before and after solvent activation, it was observed that the SOG rejection decreased from approximately 95% to approximately 80% for both membranes. While SOG rejection decreased, the rejection of both TFC-C and TFC-0.5 membranes against MO was maintained close to 99%, similar with the MO rejection values before DMF activation. To further illustrate this observed change limited to SOG rejection only, the MWCO values of the two membranes were

determined by using dyes in methanol, and results were shown in **Figure 3.9b**. Prior to DMF activation, the TFC-C and TFC-0.5 membranes had MWCO values between 170-180 g/mol (**Figure 3.8b)**; after DMF activation, the MWCO increased to 310 and 265 g/mol for TFC-C and TFC-0.5, respectively (**Figure 3.9b**). As reported in earlier solvent activation studies for PA membranes, solvent activation bring about changes in the PA microstructure which would more likely impact the rejection of smaller chemical species [244], such as SOG in this case. The notable changes in MWCO values could be attributed to the solvent-induced swelling, enlarged pore volume, and irreversible structure change of the PA matrix after solvent activation [245].

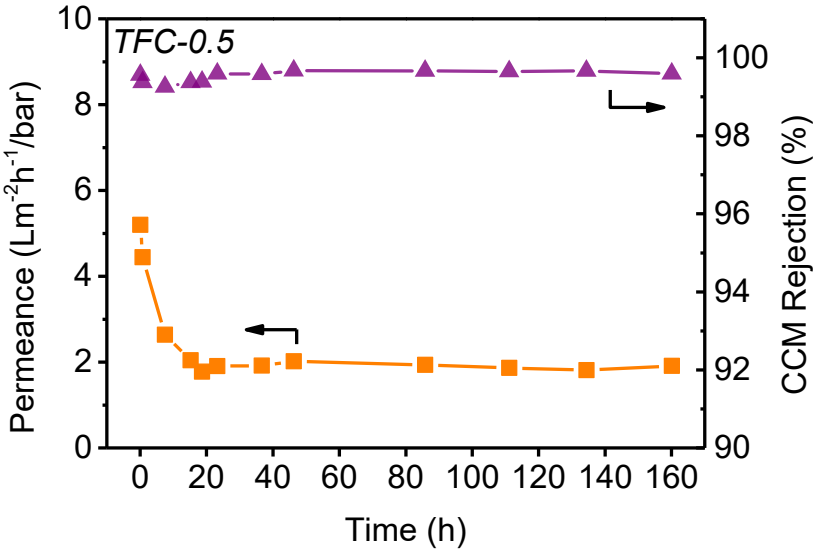

Figure 3.10. Long-term stability of the optimal TFC-0.5 membrane over a 7-day operation. Feed solution: 50 mg/L curcumin (CCM) in methanol. Flow rate: 10 mL/min.

The long-term stability of the optimal TFC-0.5 membrane was tested over a 160-h (approximately 7-d) operation using 50 mg/L curcumin (CCM) in methanol as the feed (**Figure 3.10**). CCM is chosen as a model solute for OSN in this work since it is widely used as an ingredient in dietary supplements, as well as an additive for cosmetics, food flavoring, and coloring. After the initial permeance decline observed at the onset of the operation attributed to membrane compaction, stable permeance at 2.01 L m^{-2} h^{-1}/ bar was observed until the end of the filtration. The rejection of CCM was observed to be stable at over 99.2% throughout the operation. These data show the stability of the

membrane during filtration with organic solvents over an extended period of time, as well as the applicability of the optimal CNT-interlayered TFC membrane (TFC-0.5) for separation of bioactive substances, such as CCM, from organic solvent solutions.

3.4. Summary

In this work, CNTs were coated on top of PK membrane substrates prior to PA selective layer formation via IP. The CNT coating amount was varied, and the effects of the CNT coating amount were investigated. The presence of the CNT intermediate layer brought about changes in the PA structure, depending on the CNT coating amount. At lower CNT coating amounts (> 1 mL CNT dispersion volume), multi-layered, large leaf-like structures of PA were observed, as opposed to the typical ridge-and-valley and nodular structures of the pristine TFC membrane. Moreover, the CNT-interlayered TFC membrane was successfully applied for OSN application. The presence of the CNT interlayer was able to regulate the MWCO of the TFC membrane, allowing it to selectively retain smaller molecules such as dyes and sugars, even in organic solvent environments. OSN tests revealed that the optimal membrane displayed a methanol permeance of 5.34 L m^{-2} h^{-1}/bar with an extremely MWCO of 170-180 g/mol. These results were attributed to the reduced PA intrusion, enlarged PA filtration area, and the gutter layer effect brought about by the CNT interlayer. Furthermore, the CNT interlayer was shown to have high tolerance against selected organic solvents

Chapter 4 Molecular separation of organic solvent mixtures using carbon nanotube-interlayered thin film composite membrane

4.1. Introduction

Organic solvents are widely used as raw materials or reaction media for chemical synthesis, and a huge amount of organic solvent mixtures is generated during the production of chemicals. Compared with the non-environmentally friendly solvent incineration [7, 8], separating these solvent mixtures is of great importance for product purification, solvent recovery, and sustainable production [5]. Therefore, facilities for chemical separation of organic liquids have become one of the standard configurations in modern industries, such as petrochemical, pharmaceutical, and food processing industries.

Currently, industries rely heavily on evaporation and distillation for separating solvent mixtures [6, 246]. However, these conventional energy-intensive separation approaches account for 10–15% of the world's energy consumption [6], which could leave a large carbon footprint. Distillation also faces a big challenge in separating azeotropes due to the similar boiling point of each component. All these limitations motivate engineers and scientists to explore new environmentally-benign alternative separation technologies.

Membrane separation technology has exhibited advantages like small footprint, high integration, and less energy consumption, thus making it a potential alternative technology for solvent separation and recovery [226]. Considering the small molecular dimension (less than 1 nm) and the inconspicuous differences between solvent molecules, organic solvent reverse osmosis (OSRO) can separate these compounds as it equips a highly dense membrane for sieving without any phase change during the separation process. However, the OSRO membrane development is still in its infancy

because of the rigorous requirements on chemical-resistance and separation capability. Thus, the development of high-performance OSRO membrane with precise molecule distinguishing capability and permeability has become a particularly attractive topic of interest in recent.

Great efforts have been done on the fabrication of OSRO membranes. The cellulose acetate (CA) membrane was first applied in OSRO process for separating the alcohol/aromatic hydrocarbon mixtures [64, 65]. During the last decade, membranes made from polyacrylonitrile (PAN) [66], cellulose acetate butyrate (CAB) [67], polyethylene (PE) [68], perfluorodioxole copolymer [69-71], silica-zirconia [72], organosilica [73], polyamide-imide Torlon® [74], polydimethylsiloxane (PDMS) [75], and metal oxides/polymer of intrinsic microporosity 1 (AlO_x/PIM-1) [76] were developed. There has been an advent of new materials and fabrication methods for OSRO membrane development to allow applications for harsher solvent environments. However, these membranes still suffer from insufficient separation performance or large-scale fabrication. For example, the thermoplastic polyamide-imide Torlon®-based membrane [74] has a molecular weight cut-off (MWCO) of 185 g/mol which means there is a limitation on separating the solvents with smaller molecular size, such as alcohol/alkane mixtures. The organosilica membrane [73] showed an excellent separation performance to 10 wt% toluene in methanol (M90T10) with a separation factor of 9 (toluene rejection: ~89%) and a permeance of 0.01 L m^{-2} h^{-1}/bar under the operation pressure of 3MPa, thanks to its thick and compact separation layer. However, the reported fabrication process of organosilica membrane is quite complex, since it requires repeated coating of α-Al_2O_3, SiO_2-ZrO_2 sol and bis(triethoxysilyl)acetylene (BTESA) polymer for several times and curing under 200~500℃. Thus, novel and easy-to-fabricate OSRO membranes are highly desired.

Recently, with the use of solvent-resistant materials as substrate, the concept of well-commercialized thin-film composite (TFC) polyamide (PA) membrane fabricated using interfacial polymerization (IP) has shown its potential in the OSRO process [61, 77, 78]. Liu et al. [61] reported a polyketone (PK)-based TFC PA membrane used in OSRO process for separating aliphatic alcohols, aliphatic alkanes, and aromatic compounds

from methanol. Superior separation performances and long-term stability were achieved for M90T10 mixture with separation factor of 8.4 under operation pressure of 3 MPa. It is noteworthy that the permeance of the PK TFC PA membrane was 0.17 L m^{-2} h^{-1}/bar. The permeance of this membrane is still considered low, which could limit its separation efficiency when used in real OSRO applications. Thus, investigating the permeance enhancement of OSRO membrane is as important as fabricating a dense OSRO membrane to fully understand the transport mechanism in OSRO process.

Carbon nanotube (CNT) interlayer intercalation has been demonstrated as an effective way to enhance the membrane performance from the perspectives of gutter layer effect [134-136], substrate surface property regulation [137, 138], and IP reaction facilitation [58]. In previous chapter, the cross-linked CNT-interlayered TFC membrane were used as the separation layer material for OSN process. However, the effectiveness of CNT interlayer on membrane performance enhancement for organic solvent separation has not been examined yet. Furthermore, the transport mechanism of organic solvents has still not been fully elucidated as that for salt ions or macromolecules.

Hence, the target of this work is to enhance the permeance of TFC PA OSRO membrane with no or minimal compromise in rejection. Since the CNT-interlayered TFC membrane has been well investigated in previous two works with enhanced performances demonstrated. Thus, in this work, a highly cross-linked tripe-layered TFC membrane was fabricated with using polydopamine (PDA)-modified CNT as the interlayer. The membrane performance was further examined in OSRO process. The separation performances of three kinds of solvent combinations (methanol/toluene, methanol/MTBE, and acetonitrile/toluene) were compared, and the membrane-mixture interactions were analyzed based on Hansen solubility parameters (HSP) theory to elucidate the organic solvent separation mechanism. This work could provide insights on the design and fabrication of high-performance OSRO membrane also the understanding of solvent separation mechanism.

4.2. Experimental

4.2.1. Materials

Polyketone (PK) polymer (200,000 g/mol) was kindly supplied by Asahi Kasei Co., Ltd. (Japan). Polyester (PET) nonwoven fabric (90 HP) purchased from Awa Seishi Co., Ltd. (Japan) was used as PK membrane support. Single-walled carbon nanotubes (CNT, length range: 5–30 μm, diameter: <2 nm, 95%) was purchased from Aladdin Chemical Co., Ltd. (China). 1,3,5-benzenetricarbonyl trichloride (TMC, 99%), m-phenylenediamine (MPD, 99%), sodium dodecylbenzene sulfonate (SDBS), and dopamine hydrochloride (DOPA) were purchased from Sigma-Aldrich Co., Ltd. (Japan). Resorcinol and several organic solvents (e.g., acetonitrile, methanol, acetone, tetrahydrofuran (THF), ethanol, methyl tert-butyl ether (MTBE), 1-Methyl-2-pyrrolidinone (NMP), 1-propanol, toluene) and HCl-tris buffer (1 M, pH 7.5) were obtained from Fujifilm Wako Pure Chemical Co. Ltd. (Japan). Deionized (DI) water was supplied by water purification system manufactured by Merck Millipore Co., Ltd. (Germany). All chemicals were used as received.

4.2.2. Fabrication of CNT-coated PK substrate

The PK substrate was fabricated through conventional nonsolvent-induced phase separation (NIPS) [204]. Firstly, 14 wt% PK powder was dissolved in the mixture of resorcinol and DI water (35:65, wt%) at 80℃. The mixture was stirred at least 5 h to form a homogenous casting solution. After overnight degassing at 60℃, the PK solution was cast onto a non-woven fabric with a casting gap of 400 μm. The casting plate was immediately immersed into a coagulation bath of methanol/water (20:80, wt%) for 20 min. Then, the formed membrane was fixed using a stainless-steel frame and was sequentially immersed into pure acetone and hexane for 20 min each to make sure the membrane was fully washed. Finally, the obtained PK membrane was labelled as PK14, and was dried in the air and stored for further used.

4.2.3. Fabrication of CNT-coated PK substrate

Before coating CNT onto PK substrate, the CNT was modified using polydopamine (PDA) following the reported method [208]. Generally, 10 mg CNT and 100 mg SDBS were dispersed in 100 mL DI water upon 8 h probe-sonication before centrifuged at 10,000 rpm for 1 h. Then, 10 mg dopamine (DOPA) and 10 mL HCl-Tris buffer (0.1M, pH 7.5) were added into the supernatant and stirred for 12 h at 40°C. After re-centrifugation at 10,000 rpm for 30 min, the PDA-modified CNT (CNTd) dispersion with a concentration of 0.183 ± 0.058 mg/mL was obtained.

The CNT-coated PK substrate was fabricated using spray-coating method. Briefly, 30 mL of CNTd dispersion was sprayed onto the surface of PK14 substrate using an airbrush (LPH-50-S9-04, Anest Iwata, Japan) at 0.1 MPa with a spraying distance of 30 cm. The 34 × 34 cm^2 movement area of the airbrush was larger than the effective membrane area (13 × 18 cm^2) to ensure that the membrane surface could be fully covered. The as-prepared CNT-coated PK substrates (labelled as PK14-CNTd) were further dried at 60°C for 0.5 h and stored at room temperature.

4.2.4. Fabrication of CNT-interlayered TFC membrane

The fabrication process of CNT-interlayered TFC membrane (TFC-CNTd-PA) was depicted in **Figure 4.1**.

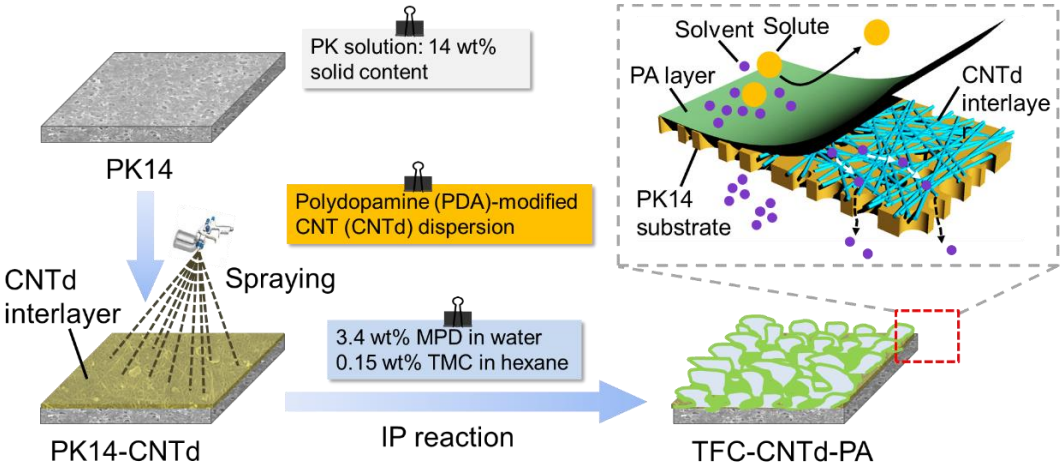

Figure 4.1. Schematic diagram of CNT-interlayered TFC membrane fabrication.

The TFC membrane having CNTd interlayer was fabricated through interfacial polymerization using MPD and TMC following the reported method [208]. Basically, the CNT side of PK14-CNTd substrate was prewetted by 3.4 wt% MPD aqueous solution for 2 min before removing the excess MPD solution by a rubber roller. Then, 0.15 wt% TMC solution in hexane was poured onto the MPD-impregnated side for 1 min. After pouring out the excess TMC solution, the nascent membrane was further cured at 60℃ for 10 min. The resultant membrane was preserved in DI water at 4℃ before testing and characterization.

4.2.5. Membrane characterization

Surface morphologies were observed by field-emission scanning electron microscopy (FE-SEM, JSF-750F, JEOL, Japan), atomic force microscopy (AFM, SPA-400, Hitachi, Japan), and transmission electron microscopy (TEM, JEM-2100F, JEOL, Japan). The surface roughness was analyzed by *Spisel* software based on AFM images. The average surface pore size and porosity were analyzed using *ImageJ* software based on the bright and contrast differences of pore- and non-pore structures in SEM images. The porosity (ε) is defined as the area ratio of pore area and total area. The membrane surface pore size distribution was measured from analysis of at least 300 pores as identified by *ImageJ* software. The bulk membrane pore size distribution and average pore size were determined using a liquid-liquid porometer (LLP-1200A, Porous Material, USA). Isopropanol and Galwick which offered by manufacture were used as wetting and displacement solvent. The element composition of PA layer was detected using X-ray photoelectron spectroscopy with monochromatic Al Kα excitation (XPS, JPS-9010MC, JEOL, Japan). The membrane surface hydrophilicity was measured using a contact angle analyzer (WCA, DM-300, Kyowa, Japan) with a droplet volume of 2 μL. The surface charge of PK14-CNTd substrate was detected using a solid zeta potential analyzer (SurPASS 3, Anton Paar GmbH, Austria) in a pH range from 3 to 10. All samples were fully dried in an oven at 60℃ overnight before characterizations and all tests were performed at room temperature.

4.2.6. OSRO performance measurement

The OSRO separation performance of TFC membrane was evaluated in a cross-flow OSRO setup with an effective membrane filtration area of 7.065 cm^2 [130]. Before testing, the TFC membrane was pre-compacted in pure methanol under 3 MPa for at least 4 h until a stable methanol permeance was reached. Then, the pure methanol permeance was measured under the same pressure with a cross-flow rate of 9.9 mL/min. After that, the permeance and rejection of solvent mixture were measured by switching the pure methanol to the solvent mixture as feed solution. The permeate was collected and its weight gain was recorded by an electronic balance. The permeance (P, L m^{-2} h^{-1}/bar) can be calculated based on the following Eq. (4-1):

$$P = \frac{M}{S \times t \times \rho \times \Delta p} \tag{4-1}$$

where M (g) is the mass of permeate; S (m^2) is the effective membrane area; t (h) represents the filtration time, ρ (g/L) is the density of permeate, and Δp is the applied pressure on the feed side.

Next, binary solvent mixtures were tested in this work, wherein the component with higher amount was considered as solvent and the other was solute. For example, solvent mixture of "A*x*B*y*" means that the mixture is composed of component A (solvent) and component B (solute) which take a proportion of x wt% and y wt% ($x>y$), respectively. The composition of permeate and feed solution were determined using gas chromatography (GC, GC-2014, Shimadzu, Japan). Based on this conception, the solute rejection (R, %) and separation factor (α) can be calculated using Eq. (4-2) and Eq. (4-3):

$$R = \left(1 - \frac{C_{solute}^{permeate}}{C_{solute}^{feed}}\right) \times 100\% \tag{4-2}$$

$$\alpha = \frac{[C_{solvent}/C_{solute}]^{permeate}}{[C_{solvent}/C_{solute}]^{feed}} \tag{4-3}$$

where $C_{solute}^{permeate}$ and C_{solute}^{feed} are solute concentrations in permeate and feed solution, respectively. $C_{solvent}$ having superscripts *permeate* or *feed* represent the concentrations of solvent component in permeate and feed solution, correspondingly. It should be noted that the separation factor larger than 1 indicating that the solvent is preferentially

penetrating through the membrane.

4.2.7. CNT leakage measurement

The potential leakage of CNTd during organic solvent filtration was investigated. The leakage experiment was conducted using a cross-flow OSRO setup using pure methanol as the feed under the operating pressure of 5 MPa. The permeate side was reflowed to the feed solution to make sure that any possible leaked CNTd remained in the system. After continuously running for 6 days, the permeate was collected, and the existence of CNTd was detected by a UV–vis spectrophotometer (Shimadzu, UV-2700, Japan) at 262 nm [247].

4.2.8. Hansen solubility parameters (HSP) calculation

In HSP theory, the solubility parameter (δ) of one substance was divided into three components: δ_D, δ_P and δ_H, which represents the cohesion energy density of dispersion (E_D), polarity (E_P) and hydrogen-bonding (E_H), respectively. Through comparing the similarity of HSP values of two substances (e.g., solvent-solvent, solvent-polymer), the affinity between the two components could be estimated. Based on this, the HSP theory was applied to investigate the interaction between the solvent mixture and the membrane, and to further understand the organic solvent separation mechanism. According to the Hansen's handbook [248], the HSP values of solvent mixture can be calculated such that the HSP of the mixture is the volume-weighted average of the HSP of the components, as described in Eq. (4-4) and Eq. (4-5):

$$\delta_{blend} = \left(\varphi_{comp1} \times \sigma_{comp1}\right) + \left(\varphi_{comp2} \times \sigma_{comp2}\right) \quad (4\text{-}4)$$

$$\sigma_{comp1} = \frac{\left(\frac{Wt.Fraction}{Density}\right)_1}{\left(\frac{Wt.Fraction}{Density}\right)_1 + \left(\frac{Wt.Fraction}{Density}\right)_2} \quad (4\text{-}5)$$

where δ_{blend} ($MPa^{0.5}$) represents one of the three HSP portion of solvent mixture; φ ($MPa^{0.5}$) represents the corresponding HSP portion of component 1 and component 2; σ is the volume fraction of component 1 and component 2. A detailed example of calculation was given in the *discussion* section of Supporting Information.

For a given two-component (solvent-solvent, solvent-polymer) system, the affinity

or interaction between them can be estimated using the HSP distance (R_a), as follows:

$$R_a = \sqrt{4(\delta_{D,m} - \delta_{D,s})^2 + (\delta_{P,m} - \delta_{P,s})^2 + (\delta_{H,m} - \delta_{H,s})^2} \quad (4\text{-}6)$$

where the δ_D, δ_P and δ_H represent the dispersion, polar and hydrogen bonding solubility parameter respectively; and the subscripts *m* and *s* refer to the membrane and solvent, respectively.

4.2.9. Dynamic long-term stability evaluation

Dynamic long-term separation tests were performed to check the membrane stability and recovery during continuous operation. Before evaluating the separation performance, the membrane was pre-compacted under 3 MPa for 3 days using pure methanol as the feed. After reaching stable pure methanol permeance, the feed solution was changed to the solvent mixture with 10 wt% solute content, and the filtration experiment was conducted at the same operation pressure. The filtration was operated for 30 days, during which the feed solution was kept constant. The permeance recovery tests were performed as soon as the 30-day operation finished by changing the feed solution to pure methanol. The mixture permeance during long-term separation and the recovered pure methanol permeance were normalized by the compacted methanol permeance to determine the degree of permeance decline and recovery.

4.3. Results and discussions

4.3.1. Effects of CNTd interlayer on PK surface properties

Since the substrate could impart significant changes on PA formation, the structure and properties of PK14 substrate before and after CNTd network deposition were fully characterized and results were shown in **Figure 4.2**. The pristine PK14 substrate had a typical fiber-like structure (**Figure 4.2a** and **d**) similar with the previous work [131, 132, 249]. After depositing CNTd, a contiguous network was formed which almost fully covered the original PK14 surface feature, leaving few large surface pores (**Figure 4.2b**). The cross-sectional SEM image (**Figure 4.2e**) gives a clearer view of the CNTd network which leeched on to the fibrous structure of PK14 substrate. It should be noted

that the CNTd used in this work were modified using PDA. The specific interaction for creating a continuous and stable CNTd network is considered to be the remarkable adhesion ability of PDA molecules through covalent binding [250-252]. During the spray-coating process, the CNTd are randomly deposited and interlaced with each other. The PDA outer layer provides a sticking point for the overlapping parts of CNTd and connects them through further oxidative polymerization of catechol groups [252, 253], resulting in a continuous and stable network of CNTd. On the other hand, the PDA also provides a superior adhesion for CNTd interlayer to PK14 substrate through covalent coupling [254], ensuring the stability of CNTd interlayer during the filtration process.

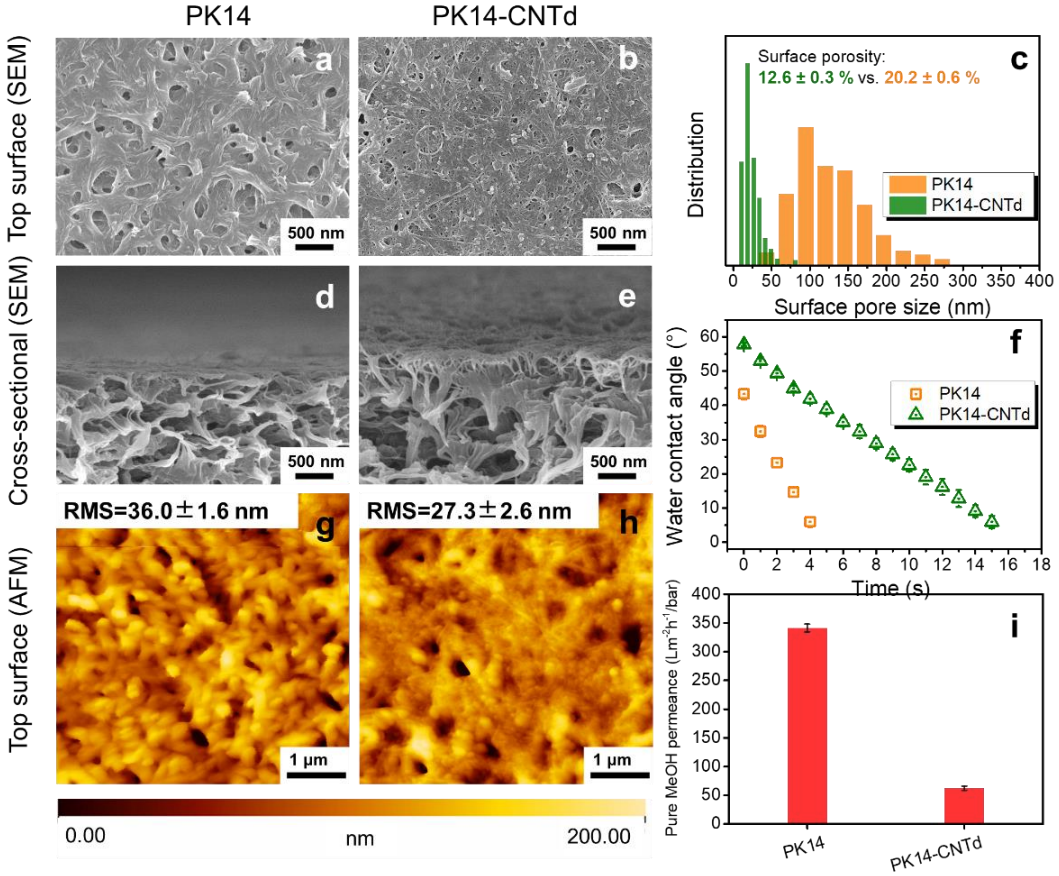

Figure 4.2. Surface and cross-sectional morphologies of (a, d, g) PK14 and (b, e, h) PK14-CNTd substrates, and the corresponding (c) surface pore size and porosity analyzed by Image J software, (f) water contact angle, and (i) pure methanol permeance.

The AFM results (**Figure 4.2g** and **h**) show that the RMS (root-mean-square) surface roughness decreased from ~36.0 nm to ~27.3 nm after deposition of the CNTd network,

which also confirms that the finer and interlaced CNTd covered the original surface feature of PK14 surface and made the surface smoother. It is noteworthy that the surface hydrophilicity changed reasonably after depositing CNTd as a result of the decreased surface roughness (**Figure 4.2f**). These changes in hydrophilicity and surface roughness could play a positive role in controlling the release of MPD molecule during the IP reaction and forming a defect free PA nanofilm as studied in previous Chapter 2.

To further quantify the variation, the surface porosity and surface pore size distribution of PK14 and PK14-CNTd substrate were statistically analyzed based on the SEM images (**Figure 4.2c**). Compared to the pristine PK14 substrate, the surface porosity of PK14-CNTd substrate decreased from ~20.2% to ~12.6% because of the existence of CNTd network, and the average surface pore size of PK14-CNTd substrate decreased from ~127 nm to ~24 nm also with a narrower pore size distribution (**Figure 4.2c**). Meanwhile, the pure methanol permeance of PK14-CNTd substrate also verified the integrity and density of CNTd network, as it dropped to 61.6 ± 3.8 L m^{-2} h^{-1}/bar compared to the pristine PK14 substrate whose pure methanol permeance was 340.9 ± 6.8 L m^{-2} h^{-1}/bar (**Figure 4.2i**). The decrease in pure methanol permeance is mainly because of the reduced pore size. Typically, the water transport through a membrane can be described by the Hagen-Poiseuille equation (Eq. (4-7)) in which the water permeance is proportional to the radius and the membrane porosity [12].

$$J_w = \frac{\varepsilon r_p^2 \Delta P}{8\eta\tau l_m} \tag{4-7}$$

where J_w is the water flux, ε the membrane porosity, r_p the pore radius, η the viscosity of water, τ the tortuosity of the membrane, and l_m the thickness of the rejection layer. In this case, due to no solute retention involved in pure methanol permeance testing, this water transport model can also be applied to methanol transport which means for the PK14-CNTd substrate, the smaller membrane pore size led to the lower methanol permeance.

4.3.2. Changes on PA structure and properties having CNTd interlayer

Figure 4.3 gives the surface morphologies of the PA layer formed on PK14 substrate and PK14-CNTd substrate, respectively. Typical leaf-like structures were formed for

both two PA layers and the sizes of TFC-CNTd-PA layer were much larger than TFC-PA layer (**Figure 4.3a** and **e**). The apparent thicknesses of PA layer estimated based on cross-sectional SEM images (**Figure 4.3b** and **f**) were ~286 nm and ~495 nm for TFC-PA and TFC-CNTd-PA, respectively, as evidenced by the Z-height differences determined using AFM (**Figure 4.3d** and **h**).

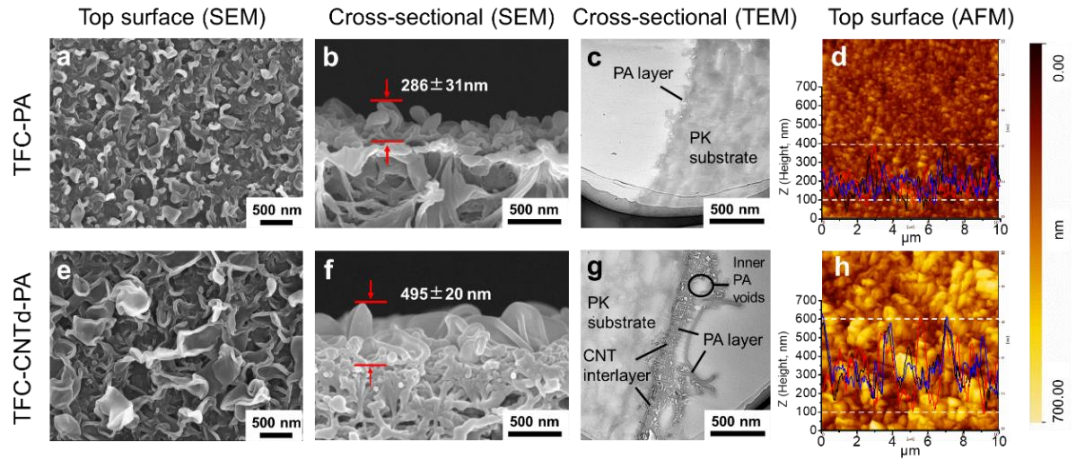

Figure 4.3. The surface and cross-section SEM, TEM and AFM images of TFC-PA (a, b, c and d) and TFC-CNTd-PA (e, f, g and h) membrane.

Compared to the TFC-PA membrane (**Figure 4.3c**), the CNTd interlayer (black boundary) in TFC-CNTd-PA membrane (**Figure 4.3g**) can be clearly distinguished between the PA layer and PK14 substrate in TEM images, and its thickness was estimated around 40 nm. It can also be seen that there were many small white parts in the PA layer of TFC-CNTd-PA membrane (**Figure 4.3g**) than that in TFC-PA membrane (**Figure 4.3c**). These parts can be considered as the inner voids of PA layer which could be attributed to the formation of large leaf-like structure. It is precisely because of the increase of inner voids that the specific area of PA (*S* ratio in **Table 4.1**) was greatly increased without adding further transport resistance. Thus, the larger leaf-like structure of polyamide layer formed on PK-CNTd substrate will also beneficial to provide high permeance for solvents.

The formation of crumpled leaf-like structure has been well established in literature, which is a relatively mature feature of MPD-based PA nanofilm prepared with high

monomer concentration [211]. The influence of the CNTd interlayer on PA formation regulation is the synergistic effect of the following: Firstly, the intercalation of CNTd layer homogenized the distribution of MPD monomer, facilitating the IP reaction to occur more on the surface of CNTd layer rather than the interior of the PK14 pores [138]. Specifically, the reduced pore size and lower hydrophilicity after depositing CNTd network lessened the intrusion of MPD into the inner side of PK, allowing more MPD monomers to be stored in the CNTd network instead of the PK14 substrate. Upon introducing the TMC monomer, the IP reaction happened immediately on the surface and along the CNTd network. Additionally, the 2D planar structure of the CNTd effectively blocks the penetration of the MPD solution into the PK14 substrate due to the capillary force and thus restrains the growth of PA into the micropores of PK, subsequently reducing the mass transport resistance during separation process [139]. Secondly, the significant changes on PA morphology were also the result of heat-intensified IP reaction during the PA formation [31]. The heat generation during IP reaction increases the local temperature of aqueous-organic interface, causing instabilities in hexane phase according to the temperature-dependent Rayleigh-Benard convection [31, 255], which leads to an irregular diffusion of MPD molecules into TMC phase then reacting to form polyamide. With prolonged reaction time, the TMC molecules react with oligomer fragments and link them together, eventually forming a continuous and more crumpled PA nanofilm [23]. However, for TFC-CNTd-PA membrane having a CNTd interlayer with much smaller pore size, this heat-intensified interface instability was enhanced as the CNTd layer containing thin water layer is not a good heat sink compared to the PK14 substrate containing thick water layer and large pore size [31]. In this situation, the heat generated will be conducted more to the hexane phase, and partially change the partition coefficient of MPD in hexane [22, 23]. Part of MPD molecules diffuse into a deeper position of the hexane phase then form acylated polyamide oligomers, and finally form a PA layer with greater apparent thickness and leaf-like structures. This regional-enhanced diffusion phenomenon of MPD molecules also resulted in greater surface roughness (RMS roughness) and specific area (*S* ratio) (**Table 4.1**).

Other surface properties of PA layer are listed in **Table 4.1**. It is worthy to mention that the TFC-CNTd-PA membrane exhibited a higher cross-linking degree (0.93±0.07) than TFC-PA membrane (0.62±0.10). Generally, higher cross-linking degree of PA means that less carboxyl groups remained on the PA surface [200], which could generate different interactions with solvent molecules during organic solvent separation.

Table 4.1. Surface properties of polyamide layer.

Sample	Water contact angle (°)	Zeta potential (pH=7, mV)	Cross-linking degree [a]	RMS roughness (nm) [b]	S ratio [c]
TFC-PA	70.2 ± 3.6	-18.7 ± 1.4	0.62 ± 0.10	57.2 ± 3.8	1.44 ± 0.01
TFC-CNTd-PA	93.8 ± 3.0	4.5 ± 1.6	0.93 ± 0.07	141.5 ± 9.5	1.63 ± 0.04

[a] Cross-linking degree (n) was calculated based on the equation: $\frac{N}{O} = \frac{3n+2(1-n)}{3n+4(1-n)}$. The detail elemental composition was listed in **Table 4.2**.

[b] RMS (Root-mean-square) roughness and *S* ratio were obtained based on AFM images.

[c] S ratio: the ratio of scanned surface area to the projected area.

Table 4.2. Elemental compositions of the fabricated TFC OSRO membrane detected by XPS.

Membrane	Element content (%)			Element ratio	Cross-linking degree
	C	N	O	N/O	
TFC-PA	72.95±1.31	11.81±0.78	15.25±0.78	0.78±0.05	0.62±0.10
TFC-CNTd-PA	72.95±0.76	13.23±0.43	13.82±0.54	0.96±0.04	0.93±0.07

4.3.3. OSRO performance evaluation and underlying mechanism of CNTd interlayer

4.3.3.1. Validation of CNTd interlayer on permeance enhancement

Before evaluating the OSRO separation performance, single-component organic solvent filtration tests were performed to assess the affinity of membrane to different organic solvents. It should be noted that all membrane filtration and separation tests were performed after at least 4-h membrane pre-compaction in pure methanol under 3 MPa (**Figure 4.4a**). Prior to applying to solvent separation, the fabricated TFC membranes were tested in water RO desalination process to confirm the absence of defects. The TFC-CNTd-PA membrane demonstrated an enhanced rejection rate of 98.4%

for NaCl, with the water permeance of 1.72 L m^{-2} h^{-1}/bar (**Figure 4.4b**), confirming the effect of CNTd interlayer on improving permeance without compromising rejection. These results are consistent with the previous studies on CNTd interlayer that attributed the improved separation performances in aqueous RO process to the increased PA cross-linking degree, larger filtration area, and the gutter layer effect of CNTd interlayer [135, 136, 138, 139].

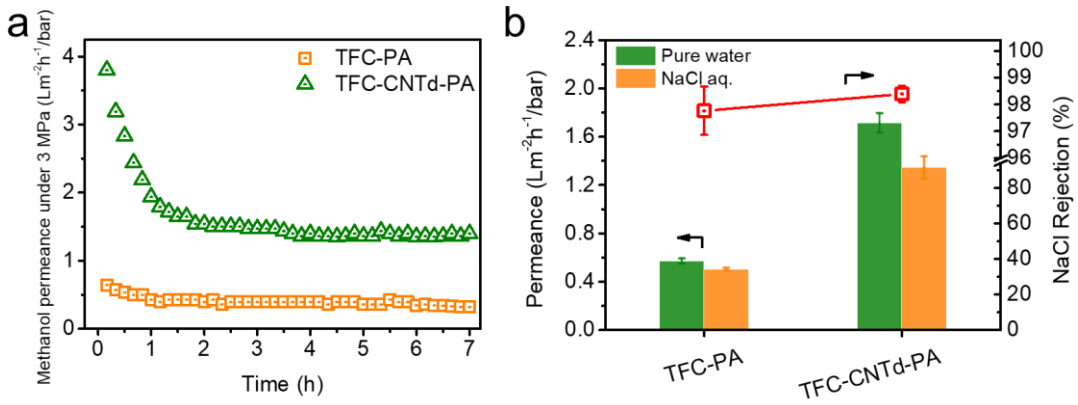

Figure 4.4. (a) Pre-compaction stage of TFC-PA and TFC-CNTd-PA membrane at 3 MPa; (b) Water RO performance of TFC-PA and TFC-CNTd-PA membrane.

Figure 4.5 shows the OSRO performances of TFC membranes. The pure solvent permeances of both two TFC membranes are linearly related to the solvent properties and fitted well with the typical solvent transport model [31] (**Figure 4.5**), which ascribed the pure solvent permeance to three intrinsic parameters of organic solvents as described in Eq. (4-8):

$$Permeance = K\frac{\delta_p}{\eta d_m^2} \quad (4\text{-}8)$$

where K is a constant of PA layer, and δ_p ($MPa^{0.5}$), η (Pa S) and d_m (nm) represent the Hansen solubility parameter of polar portion, viscosity, and molar diameter of the solvents. Due to the polar nature of the PA layer [256, 257], both TFC membranes tend to be preferentially permeable to solvents having small molar diameter, low viscosity, and high polarity, such as acetonitrile, methanol, and acetone (**Table 4.3**). Nevertheless, the TFC-CNTd-PA membrane showed an enhanced permeability than the TFC-PA membrane. For example, the methanol permeance has increased four times higher from

0.32 L m^{-2} h^{-1}/bar to 1.39 L m^{-2} h^{-1}/bar due to the intercalation of CNTd interlayer. These significant changes in membrane permeance could be owed to the synergy of CNTd gutter layer effect, larger PA filtration area and less PA intrusion into the substrate. Since the intercalation of an interlayer has become a popular way to improve membrane performance, the gutter layer effect has been widely discussed in several CNTd interlayer related works. The gutter layer effect on permeance enhancement was comprehensively studied and confirmed from both transport modeling and experiments [135, 136]. In general, a highly permeable interlayer can facilitate the water transport in the transverse direction, thereby minimizing the transport distance within the low-permeability polyamide film [135]. In this work, the permeance enhancement is generally applicable for different mixtures, indicating that the gutter layer effect was not influenced by the solvent property. On the other hand, the large PA filtration area and less PA intrusion into substrate were also essential factors that contributed to high permeance.

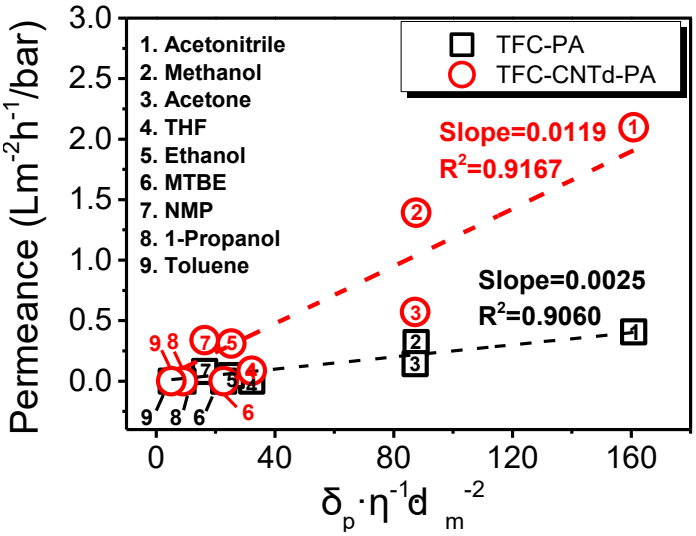

Figure 4.5. Relationship of pure solvent permeances with solvent properties.

Table 4.3. Properties of organic solvents used in this work.

Solvent	δ_D [a]	δ_P [a]	δ_H [a]	δ [b]	Density (ρ) at 20℃ (g/cm^3) [a]	Viscosity (η) at 20℃ (cP) [a]	Molecular weight (g/mol)	Molar volume (V_m) (cm^3/mol) [a]	Molar diameter (d_m) (nm) [c]
Acetonitrile	15.3	18.0	6.1	24.4	0.79	0.37	41.05	52.6	0.55
Methanol	14.7	12.3	22.3	29.4	0.79	0.59	32.04	40.7	0.51
Acetone	15.5	10.4	7.0	20.0	0.79	0.35	58.08	74.0	0.62
THF	16.8	5.7	8.0	19.5	0.89	0.55	72.11	81.7	0.62
Ethanol	15.8	8.8	19.4	26.5	0.79	1.22	46.07	58.5	0.57
MTBE	14.8	4.3	5.0	16.2	0.74 [d]	0.36	88.15	119.8	0.72
NMP	18.0	12.3	7.2	23.0	1.03	1.67	99.13	96.5	0.67
1-Propanol	16.0	6.8	17.4	24.6	0.80	1.95	60.10	75.2	0.62
Toluene	18.0	1.4	2.0	18.2	0.87	0.59	92.14	106.8	0.70
PA layer [e]	18.0	11.9	7.9	23.0	N/A	N/A	N/A	N/A	N/A

[a] HSP values, density, viscosity and molar volume data of solvents are taken from the Hansen solubility parameters: a user's handbook [248].

[b] The total HSP value (δ) is calculated form [248]: $\delta^2 = {\delta_D}^2 + {\delta_P}^2 + {\delta_H}^2$.

[c] The molar diameter (d_m) was calculated using molar volume (V_m) of the solvent molecule based on [31, 258]: $d_m = 2 \times ({}^{3V_m}/_{4\pi N_A})^{1/3}$; where N_A is the Avogardo's number.

[d] Data obtained from Reference [259].

[e] HSP data of PA are taken from Aharoni, S. M.'s work [256].

For solvent separation, another key factor that should be considered is the interaction between the selective layer and organic solvents. Considering the polar property of polyamide layer, the separation of polar/non-polar and polar/less-polar solvent combinations was chosen. Herein, three different solvent mixtures related to the practical application were screened out [223, 260, 261]: methanol/toluene (M/T), methanol/methyl tert-butyl ether (M/MTBE) and acetonitrile/toluene (ACN/T) as the feed solutions based on the following reasons: (1) Methanol and toluene are extensively used as raw materials for the synthesis of styrene or p-xylene in fine chemical industry [223, 260, 262, 263]. A huge amount of waste streams containing methanol and toluene were generated during the production process and separating these mixtures is necessary for the sustainable production. (2) MTBE is adopted as an alternative of tetraethyl lead to improve antiknock of gasoline [73, 261, 264]. The production of MTBE requires methanol and isobutylene as raw material with excess methanol being used for higher yield [261]. Thus, the removal of unreacted methanol from reactor product is of high demand before blending MTBE into the gasoline pool. (3) Acetonitrile/toluene mixtures usually serve as the reaction media for polymer synthesis, such as the synthesis of molecularly imprinted polymers (MIPs) [265, 266]. The separation of acetonitrile and toluene is also a pertinent procedure for sustainable production. Moreover, there is a huge difference of polarity between acetonitrile and toluene. which offers a chance to understand the separation performance from the perspective of membrane-mixture interaction, instead of the well-known point of view that the polarity difference dominates the separation.

Considering the fabricated TFC membranes had a preference to penetrate the polar solvents with small molecular size, in this work methanol and acetonitrile served as solvents, while toluene and MTBE were used as solutes that should be rejected by the membrane. The TFC-CNTd-PA membrane exhibited significantly higher permeances (2 to 4 times higher) for all three mixtures under all solute concentrations (**Figure 4.6**). For example, the permeance of TFC-CNTd-PA membrane reached to 0.64 L m^{-2} h^{-1}/bar in comparison with 0.22 L m^{-2} h^{-1} /bar for TFC-PA membrane when 5 wt% toluene in methanol (M95T5) was used (**Figure 4.6b**). Similar permeance enhancements were

also observed for M/MTBE and ACN/T mixtures, validating the effectiveness of CNTd interlayer in improving the membrane permeances [135, 138].

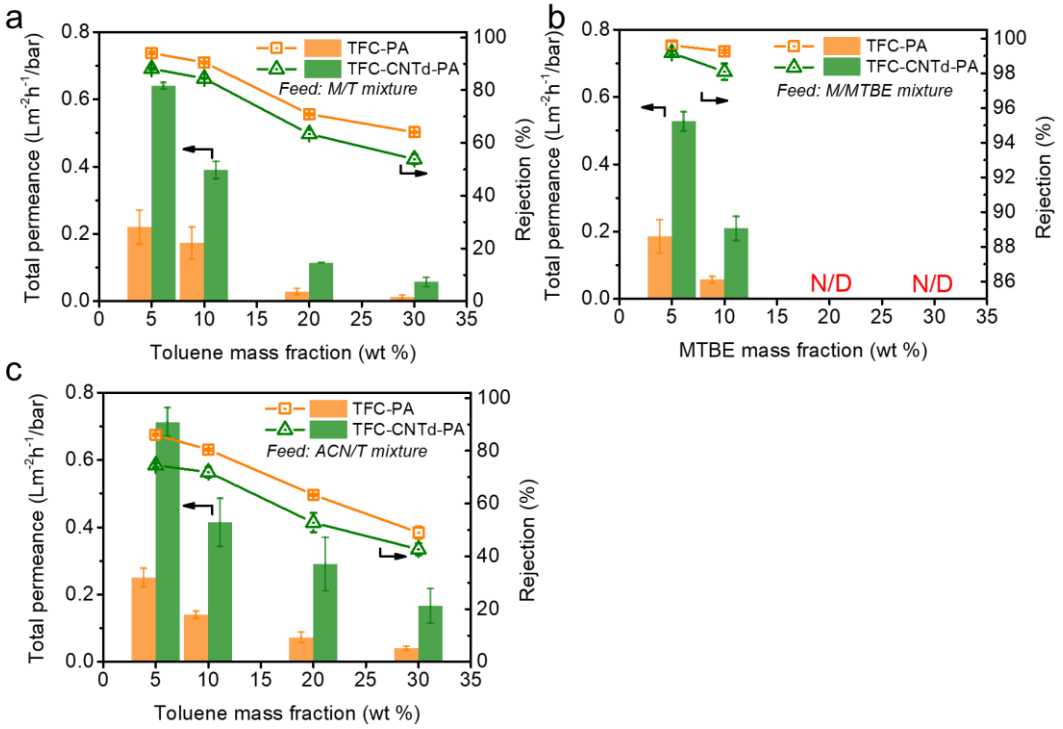

Figure 4.6. Solvent separation performances of TFC-PA and TFC-CNTd-PA membrane using (a) methanol/toluene (M/T) mixture, (b) methanol/methyl tert-butyl ether (M/MTBE) mixture, and (c) acetonitrile/toluene (ACN/T) mixture with solute concentration from 5 wt% to 30 wt%.

Additionally, the membrane permeances decreased as the solute concentration increased because of the increased osmotic pressure [61]. It should be noted that neither of the two TFC membranes showed any permeances when more than 20 wt% MTBE in methanol was used. it is believed that the lack of permeance for the M/MTBE mixture with high solute content is because the osmotic pressure of M/MTBE mixture with over 20 wt% MTBE content is too high (shown in **Table 4.4**, 6 MPa and 11 MPa for 20 wt% and 30 wt% MTBE in methanol respectively, calculated according to earlier works [73, 75]) to generate effective driving pressure under the operation pressure of 3 MPa, leading to no permeances for both two TFC membranes.

Table 4.4. Calculated osmotic pressure of different organic solvent mixtures.

Organic solvent mixtures	Solute component	Solute mass fraction (wt%)	Calculated osmotic pressure (MPa) [a]
Methanol/Toluene (M/T)	Toluene	5	1.05
		10	2.09
		20	4.09
		30	6.01
Methanol/MTBE (M/MTBE)	MTBE	5	1.10
		10	2.34
		20	5.89
		30	10.98
Acetonitrile/Toluene (ACN/T)	Toluene	5	1.09
		10	2.31
		20	5.15
		30	8.68

[a] The osmotic pressure was calculated based on the method reported in literature [73].

4.3.3.2. Understanding the solute rejection based on the membrane-solvent interaction

Comparing the solute rejection of TFC-PA and TFC-CNTd-PA membranes, the latter exhibited compromised rejection towards all three mixtures. Moreover, both the TFC-PA and TFC-CNTd-PA membranes showed different separation performances when different solvent mixtures were used, but the rejection performance of both membranes followed this order: M/MTBE > M/T > ACN/T. These differences show that the solute rejection is not only related to the affinity of one single solvent component to the membrane, but also to the nature of solvent mixture. In this case, it is believed that these differences in rejection are the result of the two simultaneously-occurring interactions involving the membrane: membrane-organic solvent mixture interaction, and preferential adsorption of PA layer, as depicted in **Figure 4.7**.

The first is the interaction of the organic solvent mixture with the membrane. The co-solvent effect [267], a well-known phenomenon for solvent screening in material production and processing industries, is commonly employed by combining multiple organic solvents to dissolve materials which could not be easily dissolved by the individual solvents [268]. Similarly, when the polymeric TFC membrane comes in contact the organic solvent mixture, it may be hypothesized that co-solvent effect may provide a different interaction between the membrane and the solvent mixture, from the

interactions between the membrane and the individual mixture components.

The second interaction is the selective adsorption depending on the specific surface properties of the PA selective layer. Considering the polarity of PA molecular chain and the molecular size of solvent and solute component, the PA layer has a preference to adsorb the polar solvent component with small molecular size (e.g., methanol or acetonitrile) and reject the non-polar solute component with larger size (e.g., toluene or MTBE), thus organic solvent separation occurs. The preferential adsorption is heavily dependent on the surface properties of the selective layer, particularly its functional groups [223, 269]. The higher the number of polar functional groups present on the membrane surface, the higher its affinity to polar solvents, facilitating the easier adsorption and diffusion. It is noteworthy that, despite the clear differences in polarity and size of the mixture components, membrane rejection was not 100% since it was possible that solute (component present in lower amount) molecules were able to go through the membrane along with the solvent molecules due to the co-solvent effect and the membrane-mixture interaction.

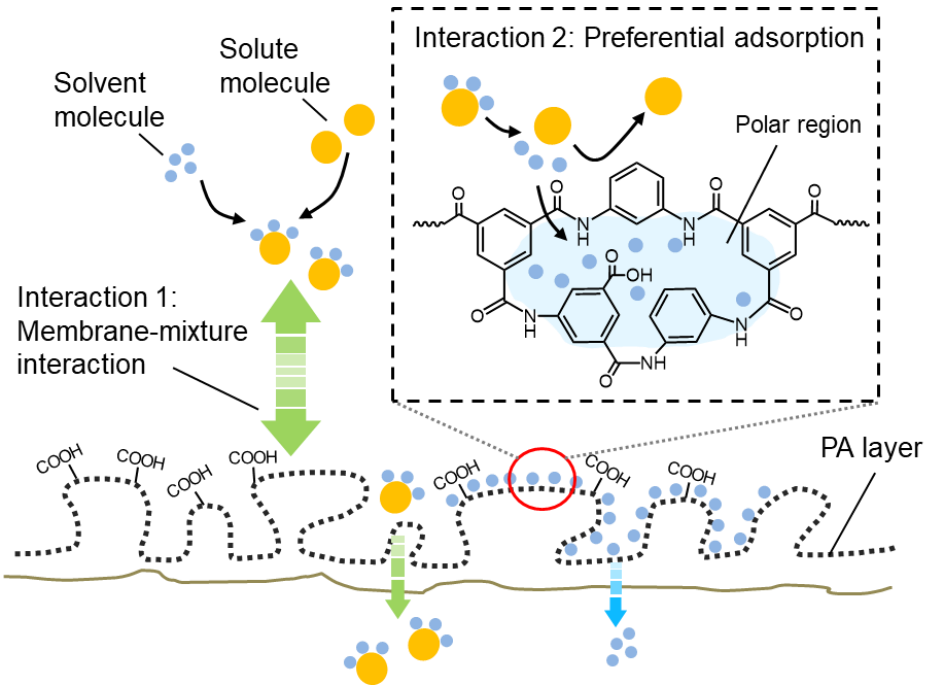

Figure 4.7. Schematic diagram of the proposed separation mechanism of organic solvent mixtures.

Since both the TFC-PA and TFC-CNTd-PA membrane followed the same trend in terms of separation performance (M/MTBE > M/T > ACN/T), this order was first ascribed to the membrane-mixture interaction. For a more concrete comparison, the HSP values of solvent mixtures and the HSP distances (Ra) between membrane and solvent mixtures were determined. Instead of representing the HSP in a classical 3D Hansen spherical workspace [248], a Teas plot or ternary HSP diagram was applied to locate the contribution of dispersion, polarity and hydrogen bonding portion in three axes [270, 271] (**Figure 4.8a**). The ternary HSP diagram allows to observe when one portion is predominant over the others and visually compare how close the HSP of two molecules in a 2D way, as well as to estimate the interactions between the molecules.

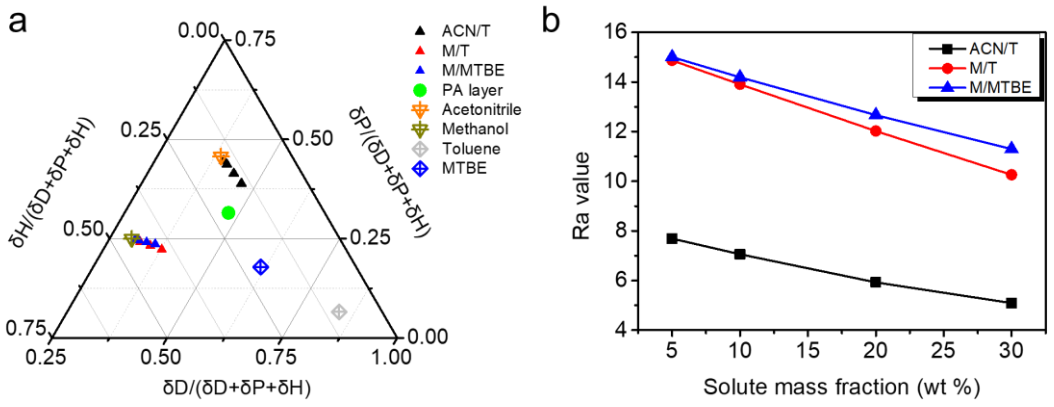

Figure 4.8. (a) HSP values of solvents and of membrane shown in a ternary diagram; and (b) Ra value between the solvent mixture and PA layer at different compositions. Detailed description of HSP values and Ra calculation can be found in Supporting Information (**Table 4.3**).

In **Figure 4.8a**, acetonitrile is closer to the PA layer compared to methanol. When mixing acetonitrile and toluene at certain concentrations, the resulting ACN/T mixtures (black solid triangle) appear closer to the PA layer (green solid dot). For a more specific comparison in distance change, the Ra between every mixture and the PA layer was calculated to estimate the interactions (**Figure 4.8b**). The ACN/T mixture has a significantly smaller Ra than those of the other two mixtures at certain concentrations, implying a stronger interaction with PA layer when acetonitrile is mixed with toluene.

Although the PA layer has a preferential adsorption to acetonitrile (closer to PA in ternary HSP diagram) than methanol, and reject toluene, the rejection was still compromised for separating ACN/T mixture because more acetonitrile and toluene would dissolve into the PA molecular chain as a mixture than the M/T mixture did. For TFC-CNTd-PA membrane, because fewer polar functional groups (i.e., carboxyl groups) remained on the basis of high cross-linking degree of PA layer (**Table 4.1**), this less polar surface feature could lead to a compromised adsorption for acetonitrile and enhanced interaction with toluene [74, 78]. Thus, the toluene rejection during the filtration of ACN/T mixture was observed to decrease.

Similar situation also happened to TFC-PA and TFC-CNTd-PA membrane for separating M/T and M/MTBE mixtures. Despite methanol and MTBE being close to PA layer in the ternary HSP diagram, larger Ra values were obtained once these two were mixed, which means that the co-solvent effect of M/MTBE mixtures has little effect on PA layer, and thus proving to be difficult for solvent mixture to diffuse into the PA layer. It should also be noted that the Ra values of M/MTBE mixtures were similar with those of M/T mixtures. Considering that MTBE is a less polar organic solvent and closer to the PA layer in the ternary HSP diagram than toluene, it should be able to have more interaction with the PA layer then affecting the preferential adsorption of methanol. However, given that the MTBE has a larger molecular size than toluene (**Table 4.3**), it is difficult for MTBE to diffuse into the PA layer, resulting in a higher MTBE rejection than toluene. For the TFC-CNTd-PA membrane, the surface with lower polarity would generally increase the interaction with the less polar solute component, resulting in lower rejection as compared to TFC-PA membrane. In addition, all Ra values decreased with increasing solute concentration, explaining the tendency of decreased rejection rate of solute component for all mixtures. Nevertheless, the TFC-CNTd-PA membrane demonstrated superior separation performance with permeances three times higher (~0.53 L m^{-2} h^{-1}/bar) than that of the TFC-PA membrane (~0.18 L m^{-2} h^{-1}/bar), while maintaining a rejection of 99.2% when using 5 wt% MTBE in methanol (M95MTBE5) (**Figure 4.6b**). The corresponding separation factor was calculated to be over 125, which is the highest value reported for polymer-based membranes using non-

pervaporation process when M95MTBE5 was used as the feed under an operating pressure of 3MPa.

In the case of pure solvents, strong interaction generally implies high membrane permeance. However, for solvent mixtures, the generated osmotic pressure cannot be ignored when considering the influence of interaction on membrane permeance. In this case, the membrane-mixture interaction primarily influenced the solute rejection, while the decrease in mixture permeance with increased interaction force and solute concentration was mainly due to the increased osmotic pressure, as explained previously. This is because the effective driving force which influences permeance on a large scale, was affected more by the osmotic pressure than by the interaction force. More importantly, this proposed separation mechanism allows to understand at least one thing, that is, in addition to the essential criterion of polarity differences, another key factor that should be considered is the membrane-mixture interaction when generalizing the membrane to other solvent mixture separation.

4.3.4. Filtration and long-term stability of the CNT-interlayered TFC membrane in OSRO process

The stability and durability of the membrane guarantee the separation performance during long-term operation. Herein, the filtration stability of TFC-CNTd-PA membrane was fully studied from four aspects: separation performances under different pressures, CNTd leakage, dynamic long-term stability and the membrane fouling observation.

It has been shown in many research works that the OSRO membrane must withstand high operating pressures to drive separation of solvent mixtures with a wide range of compositions. For this purpose, the membrane stability and recovery were first evaluated under different operating pressures. Before measurement, the pre-compaction stage was prolonged to 3 days under 3 MPa to make sure that the membrane was fully compacted. The measurement started with 5 MPa and ended with 2 MPa, and then raising the pressure again. Each pressure stage was measured for 10-h, and the average flux was recorded as the final flux of each stage as shown in **Figure 4.9a**. The methanol flux was linear with the operating pressure over the pressure range of 2-5 MPa,

indicating that the membrane was quite stable and recoverable in these operations. Furthermore, the solvent separation performances under different pressures were also measured to demonstrate the superior mechanical strength and function of PA selective layer under high pressure. As shown in **Figure 4.9b**, due to the osmotic pressure of the feed solution (M90MTBE10), the membrane permeance was not constant but slightly increased with the pressure. Considering that the rejections were similar, the separation factor (SF) was used here to make a clearer comparison of separation performance under different pressures. The SF increased to 179 under 5 MPa, three times higher than that under 3 MPa. The pressure-dependent separation performance has been previously reported and investigated in other OSRO works [61, 70]. All these results confirmed the excellent mechanical strength and stability of TFC-CNTd-PA membrane, making the membrane applicable at high operating pressures.

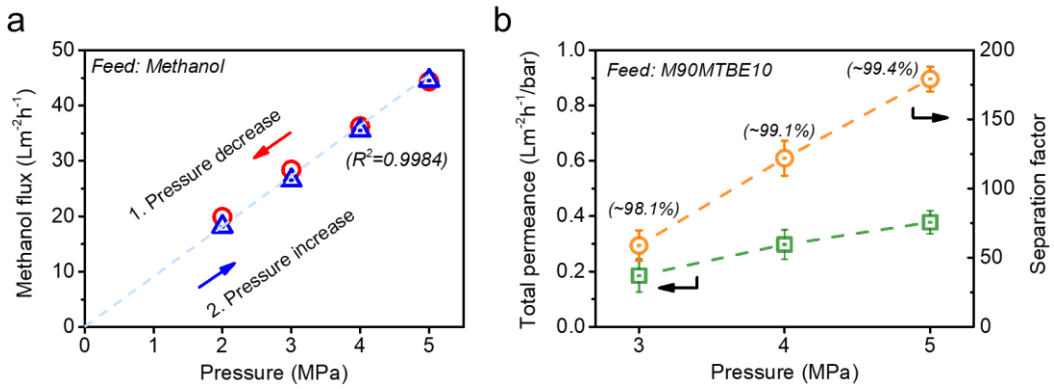

Figure 4.9. (a) Methanol flux as a function of pressure. The pressure initially decreased from 5 to 2 MPa and subsequently increased from 2 to 5 MPa; (b) permeance and separation factors for M90MTBE10 at different operating pressures.

The leaking issue of nanomaterials has always been a critical issue, especially when nanomaterials are expected to remain on the surface and function. However, the CNTd were sandwiched between the highly cross-linked PA and PK14 support layers, which gives the low possibility of leakage. Given that the pressure was unidirectionally applied on the PA layer during operation, the only possible way for CNTd leakage was through the PK14 support layer to the permeate. By comparing the UV absorption spectrum of permeate and the CNTd dispersion in methanol, no obvious absorption

peak was found in permeate spectrum (**Figure 4.10**), indicating that there was scarcely any CNTd leakage during the solvent treatment. Aside from this, most of the CNTd were embedded in the PA layer as a reinforcement material, further lowering the mobility of CNTd.

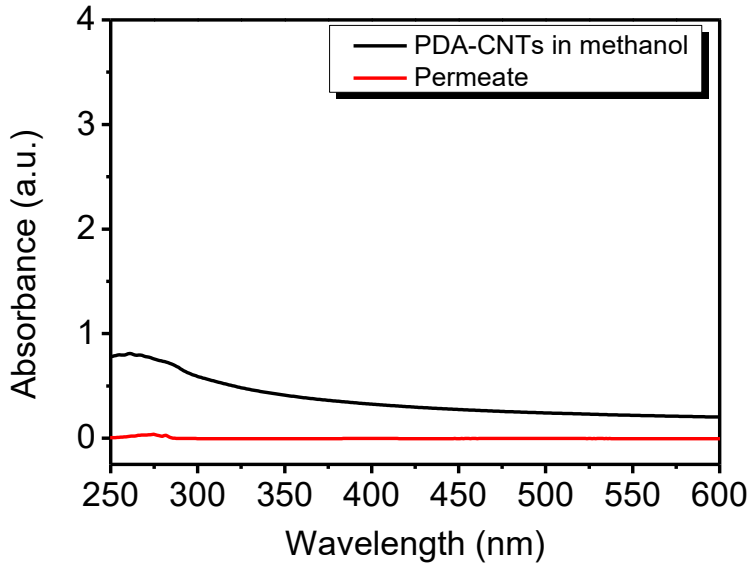

Figure 4.10. UV absorption spectrums of permeate and the CNTd dispersion in methanol.

Finally, the dynamic long-term stability of TFC-CNTd-PA membrane was evaluated using 10 wt% toluene or MTBE in methanol or acetonitrile (M90T10, M90MTBE10 and ACN90T10) as the feed solution **(Figure 4.11a**). The membrane exhibited stable permeance and rejection values over 30-day separation process for all three mixtures. The initial permeance decline ratios (see **Figure 4.11b**, 58.4%, 80.6% and 50.8% for M90T10, M90MTBE10 and ACN90T10) when changing the feed to mixtures were due to the osmotic pressure of feed solution and the membrane affinity to different solvent mixtures. For example, the ACN90T10 mixture has a higher affinity to membrane (lower Ra value in **Figure 4.8b**) than the other two, resulting in the lowest permeance decline despite of the similar osmotic pressure of the three.

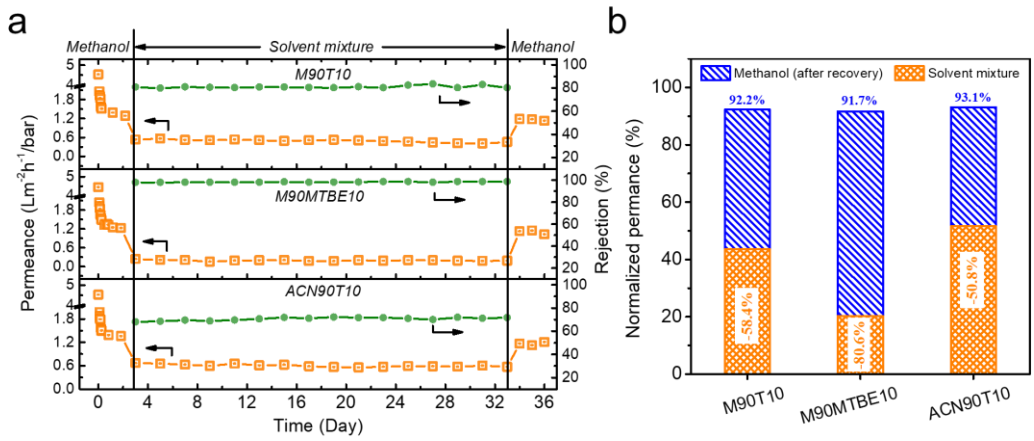

Figure 4.11. (a) Long-term stability of TFC-CNTd-PA membrane tested under 3 MPa with M90T10, M90MTBE10 and ACN90T10 as the feed respectively, and (b) normalized permeance profiles and the corresponding permeance recovery profiles after long-term testing.

Permeance recovery tests demonstrated that the TFC-CNTd-PA membrane could recover up to ~92% of the compacted methanol permeance after 30-day long-term separation testing (**Figure 4.11b**). To further determine whether the ~8% permeance loss was caused by membrane fouling, the surface morphology of the tested membrane was further checked using SEM. No significant differences on the surface morphology were observed after long-term testing, demonstrating that no fouling or damages occurred during the separation process (**Figure 4.12**). The non-fouling tendency is reasonable because the target of OSRO is to achieve the solvent separation on a much smaller molecular scale than that of macromolecular substances. Therefore, the ~8% permeance loss can be attributed to the slow and continuous compaction. To sum up, results suggest that the TFC-CNTd-PA membrane was able to withstand the harsh solvent environment and operation condition in long-term OSRO separation process.

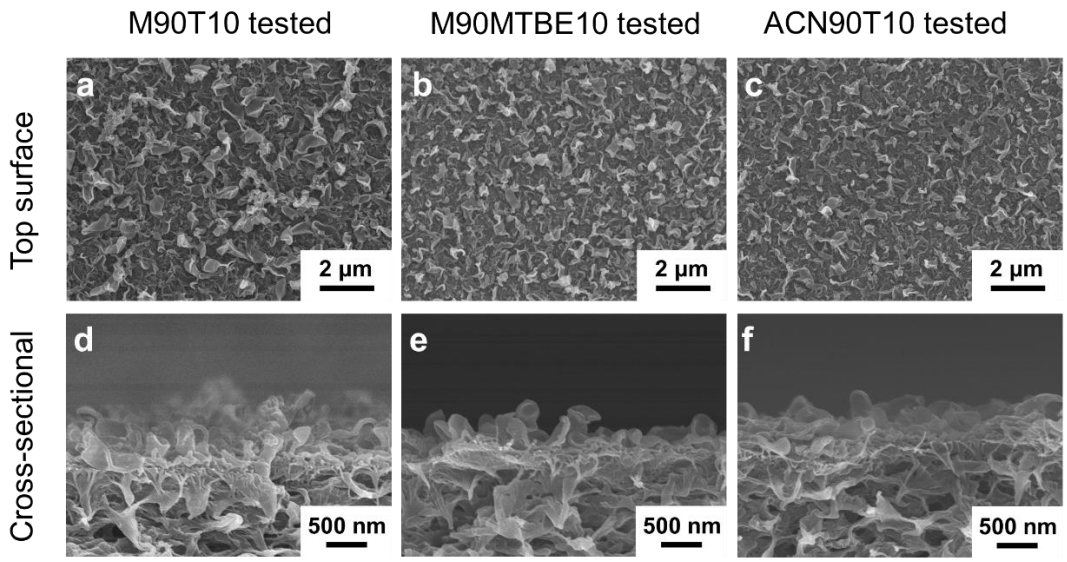

Figure 4.12. The surface and cross-sectional morphology of TFC-CNTd-PA membrane after 36-day long-term stability testing using (a, d) M90T10, (b, e) M90MTBE10, and (c, f) ACN90T10.

4.3.5. Performance comparison with reported OSRO membranes

To better elucidate the OSRO performance of TFC-CNTd-PA membrane, membrane performances were compared with reported ones on the basis of same treated solvent mixtures, namely M90T10, M90MTBE10 and ACN90T10. **Figure 4.13a** comprehensively summarized the total permeance versus separation factor of OSRO membranes with M90T10 as the feed under a constant pressure of 3 MPa, and **Figure 4.13b** showed the pressure-dependent data with M90MTBE10 or ACN90T10 as the feed [61, 73, 77, 225, 272]. One of the common features that can be seen from all three groups is that the TFC-CNTd-PA membrane exhibited quite high total permeance values compared with other OSRO membranes having a highly dense and thick selective layer and requiring complicated fabrication method. This highly permeable property is a convincing validation of the function of CNTd interlayer in permeance enhancement. However, for the CNT-interlayered TFC membrane, breaking the "trade-off" effect of OSRO seems not as easy as it does in water desalination process, due to the unique separation mechanism of OSRO. That causes a relatively lower SF in

performance comparisons. Nevertheless, the concentration- and pressure-dependent separation mechanism offer a promising alternative to overcome this drawback. For example, higher operating pressure could be applied to simultaneously obtain a high SF and permeance (e.g., M90MTBE10 group in **Figure 4.13b**). Also, multi-stage series OSRO process could be applied to increase the purity of product as each stage of separation is concentration-dependent. In short, although the membrane did not show the best separation performances in comparison with earlier reported OSRO membranes, it still gives valuable information on OSRO separation mechanism, membrane design, and OSRO operation conditions, which may provide useful guidelines and information for future works.

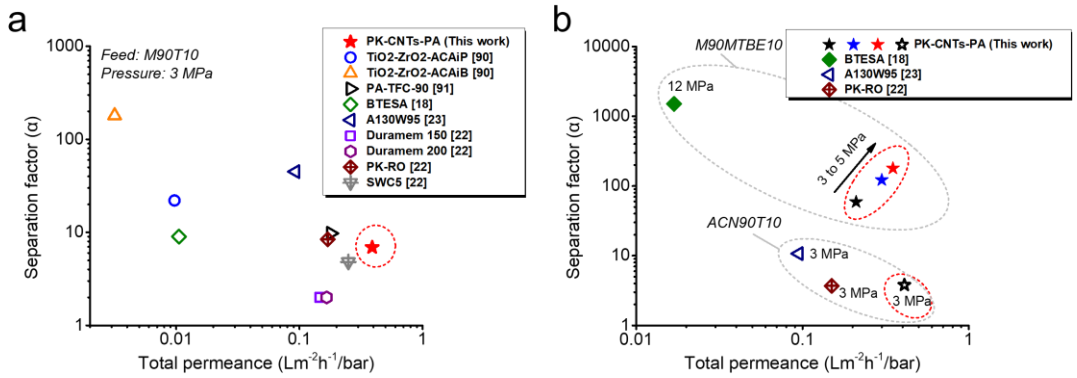

Figure 4.13. Performance comparison of TFC-CNTd-PA membrane with the state-of-the-art OSRO membranes using (a) M90T10, (b) M90MTBE10 and ACN90T10 mixtures.

4.4. Summary

In this work, a three-layered CNT-interlayered TFC membrane was applied for the first time in OSRO process, and the role of CNT interlayer was investigated in terms of regulating PA formation and enhancing membrane permeance. Results proved that by intercalating the CNTd layer, a highly cross-linked PA layer with a large filtration area was formed. The membrane permeance was significantly increased (3-4 times higher) after introducing CNTd interlayer, which can be attributed to the large filtration area of PA layer and the gutter layer of CNTd network. The TFC-CNTd-PA membrane exhibited satisfactory separation performance under different pressures and excellent

long-term stability. However, a slight decrease in rejection accompanied the permeance enhancement despite the denser PA structure and enhanced NaCl rejection observed in water RO process, which could be attributed to the less polar surface feature as a result of high cross-linking degree of PA layer. Moreover, the membrane-mixture interaction was first proposed and considered as one of the factors that affecting the rejection. Even if a huge polarity difference exists between two components, the mixture of the two might have a strong interaction with the membrane, resulting in a lower separation performance. It should be noted that there still some unsolved problems regarding to the separation mechanism and membrane design, which are worthy to be investigated in the future.

Chapter 5 Conclusions

In this dissertation, a high emphasis has been placed on the function of CNT intercalation on modifying the TFC PA membrane from the perspective of high-quality PA generation and PA surface property regulation. First, through adjusting CNT interlayer thickness, the IP monomer release was regulated, which successfully led to a transition on PA morphology. Second, the problem of high MWCO for CNT-interlayered TFC membrane was solved, and the resultant membrane with extremely low MWCO of 170-180 g/mol was successfully fabricated. In the process, the influence of CNT interlayer on surface charge of TFC membrane was investigated. A neutral TFC membrane was obtained by adjusting the CNT interlayer thickness which was correlative with the PA cross-linking degree. Enhanced antifouling performance was achieved due to the neutral surface property of CNT-interlayered TFC membrane. Additionally, the CNT-interlayered TFC membrane was applied for OSN application, and was shown to be able to separate a variety of solutes in organic solvent systems due to the low MWCO value. Notably, the CNT-interlayered TFC PA membrane was demonstrated to be able to separate solvents in OSRO process for the first time, further proving the function of CNT interlayer on membrane performance enhancement. Overall, this study demonstrates the CNT-dependent regulation to the property and performance of TFC membrane, such capabilities could aid in the development of next-generation TFC membranes.

References

[1] J. Liu, H. Yang, S.N. Gosling, M. Kummu, M. Florke, S. Pfister, N. Hanasaki, Y. Wada, X. Zhang, C. Zheng, J. Alcamo, T. Oki, Water scarcity assessments in the past, present and future, Earth's future, 5 (2017) 545-559.
[2] I.A. Shiklomanov, The world's water resources, in: Proceedings of the international symposium to commemorate, Unesco Paris, France, 1991, pp. 93-126.
[3] P.H. Gleick, Global freshwater resources: soft-path solutions for the 21st century, Science, 302 (2003) 1524-1528.
[4] Z.W. Kundzewicz, L.J. Mata, N. Arnell, P. Doll, P. Kabat, B. Jimenez, K. Miller, T. Oki, S. Zekai, I. Shiklomanov, Freshwater resources and their management, (2007).
[5] R.P. Lively, D.S. Sholl, From water to organics in membrane separations, Nature materials, 16 (2017) 276-279.
[6] D.S. Sholl, R.P. Lively, Seven chemical separations to change the world, Nature, 532 (2016) 435-437.
[7] O. Jankowitsch, L. Cavin, U. Fischer, K. Hungerbühler, Environmental and Economic Assessment of Waste Treatment Alternatives Under Uncertainty, Process Safety and Environmental Protection, 79 (2001) 304-314.
[8] P. Luis, A. Amelio, S. Vreysen, V. Calabro, B. Van der Bruggen, Life cycle assessment of alternatives for waste-solvent valorization: batch and continuous distillation vs incineration, The International Journal of Life Cycle Assessment, 18 (2012) 1048-1061.
[9] A.G. Fane, R. Wang, M.X. Hu, Synthetic membranes for water purification: status and future, Angewandte Chemie, 54 (2015) 3368-3386.
[10] J.L. Humphrey, G.E. Keller, Separation process technology, McGraw-Hill New York, 1997.
[11] K. Tang, P. Bai, J. Zhang, Y. Huo, Separation of Methanol-Toluene Azeotropic Mixture by Extractive Distillation, Asian Journal of Chemistry, 25 (2013) 3321-3326.
[12] A. Fane, C. Tang, R. Wang, Membrane technology for water: microfiltration, ultrafiltration, nanofiltration, and reverse osmosis, Treatise on water science, 4 (2011) 301-335.
[13] B.S. Lalia, V. Kochkodan, R. Hashaikeh, N. Hilal, A review on membrane fabrication: Structure, properties and performance relationship, Desalination, 326 (2013) 77-95.
[14] M.R. Esfahani, S.A. Aktij, Z. Dabaghian, M.D. Firouzjaei, A. Rahimpour, J. Eke, I.C. Escobar, M. Abolhassani, L.F. Greenlee, A.R. Esfahani, A. Sadmani, N. Koutahzadeh, Nanocomposite membranes for water separation and purification: Fabrication, modification, and applications, Separation and Purification Technology, 213 (2019) 465-499.
[15] X. Wei, C. Haire, Biaxially oriented microporous membrane, in, Google Patents, 2014.
[16] R. Gopal, S. Kaur, Z. Ma, C. Chan, S. Ramakrishna, T. Matsuura, Electrospun

nanofibrous filtration membrane, Journal of Membrane Science, 281 (2006) 581-586.
[17] A. Frenot, I.S. Chronakis, Polymer nanofibers assembled by electrospinning, Current Opinion in Colloid & Interface Science, 8 (2003) 64-75.
[18] A. Fane, C. Fell, A review of fouling and fouling control in ultrafiltration, Desalination, 62 (1987) 117-136.
[19] Y. Liu, J. Wang, Y. Wang, H. Zhu, X. Xu, T. Liu, Y. Hu, High-flux robust PSf-b-PEG nanofiltration membrane for the precise separation of dyes and salts, Chemical Engineering Journal, 405 (2021) 127051.
[20] N. Wang, T. Wang, Y. Hu, Tailoring Membrane Surface Properties and Ultrafiltration Performances via the Self-Assembly of Polyethylene Glycol-block-Polysulfone-block-Polyethylene Glycol Block Copolymer upon Thermal and Solvent Annealing, ACS applied materials & interfaces, 9 (2017) 31018-31030.
[21] K.P. Lee, T.C. Arnot, D. Mattia, A review of reverse osmosis membrane materials for desalination—Development to date and future potential, Journal of Membrane Science, 370 (2011) 1-22.
[22] E.L. WITTBECKER, P.W. MORGAN, Interfacial Polycondensation, Journal of Polymer Science, 40 (1959) 289-297.
[23] P.W. Morgan, S.L. Kwolek, Interfacial polycondensation. II. Fundamentals of polymer formation at liquid interfaces, Journal of Polymer Science, 40 (1959) 299-327.
[24] N.Y. Yip, A. Tiraferri, W.A. Phillip, J.D. Schiffman, M. Elimelech, High Performance Thin-Film Composite Forward Osmosis Membrane, Environmental science & technology, 44 (2010) 3812-3818.
[25] H.B. Park, J. Kamcev, L.M. Robeson, M. Elimelech, B.D. Freeman, Maximizing the right stuff: The trade-off between membrane permeability and selectivity, Science, 356 (2017) eaab0530.
[26] X. Zhou, Z. Wang, R. Epsztein, C. Zhan, W. Li, J.D. Fortner, T.A. Pham, J.-H. Kim, M. Elimelech, Intrapore energy barriers govern ion transport and selectivity of desalination membranes, Science advances, 6 (2020) eabd9045.
[27] A. Tiraferri, N.Y. Yip, W.A. Phillip, J.D. Schiffman, M. Elimelech, Relating performance of thin-film composite forward osmosis membranes to support layer formation and structure, Journal of Membrane Science, 367 (2011) 340-352.
[28] A.L. Ahmad, A.A. Abdulkarim, B.S. Ooi, S. Ismail, Recent development in additives modifications of polyethersulfone membrane for flux enhancement, Chemical Engineering Journal, 223 (2013) 246-267.
[29] Q. Wang, X. Gao, Z. Ma, J. Wang, X. Wang, Y. Yang, C. Gao, Combined water flux enhancement of PES-based TFC membranes in ultrasonic-assisted forward osmosis processes, Journal of Industrial and Engineering Chemistry, 64 (2018) 266-275.
[30] H.-E. Kwon, S.J. Kwon, S.-J. Park, M.G. Shin, S.-H. Park, M.S. Park, H. Park, J.-H. Lee, High performance polyacrylonitrile-supported forward osmosis membranes prepared via aromatic solvent-based interfacial polymerization, Separation and Purification Technology, 212 (2019) 449-457.

[31] S. Karan, Z. Jiang, A.G. Livingston, Sub–10 nm polyamide nanofilms with ultrafast solvent transport for molecular separation, Science, 348 (2015) 1347-1351.
[32] Z. Zhou, D. Lu, X. Li, L.M. Rehman, A. Roy, Z. Lai, Fabrication of highly permeable polyamide membranes with large “leaf-like” surface nanostructures on inorganic supports for organic solvent nanofiltration, Journal of Membrane Science, 601 (2020) 117932.
[33] W.-J. Lau, G.-S. Lai, J. Li, S. Gray, Y. Hu, N. Misdan, P.-S. Goh, T. Matsuura, I.W. Azelee, A.F. Ismail, Development of microporous substrates of polyamide thin film composite membranes for pressure-driven and osmotically-driven membrane processes: A review, Journal of Industrial and Engineering Chemistry, 77 (2019) 25-59.
[34] J. Li, M. Wei, Y. Wang, Substrate matters: The influences of substrate layers on the performances of thin-film composite reverse osmosis membranes, Chinese Journal of Chemical Engineering, 25 (2017) 1676-1684.
[35] P.S. Singh, S. Joshi, J. Trivedi, C. Devmurari, A.P. Rao, P. Ghosh, Probing the structural variations of thin film composite RO membranes obtained by coating polyamide over polysulfone membranes of different pore dimensions, Journal of membrane science, 278 (2006) 19-25.
[36] X. Lu, M. Elimelech, Fabrication of desalination membranes by interfacial polymerization: history, current efforts, and future directions, Chemical Society reviews, 50 (2021) 6290-6307.
[37] C.Y. Tang, Y.-N. Kwon, J.O. Leckie, Effect of membrane chemistry and coating layer on physiochemical properties of thin film composite polyamide RO and NF membranes: I. FTIR and XPS characterization of polyamide and coating layer chemistry, Desalination, 242 (2009) 149-167.
[38] C. Fritzmann, J. Löwenberg, T. Wintgens, T. Melin, State-of-the-art of reverse osmosis desalination, Desalination, 216 (2007) 1-76.
[39] J.E. Cadotte, Evolution of composite reverse osmosis membranes, Materials science of synthetic membranes, (1985) 273-294.
[40] J.E. Cadotte, Interfacially synthesized reverse osmosis membrane, in, Google Patents, 1981.
[41] R.W. Baker, Membrane technology and applications, John Wiley & Sons, 2012.
[42] E. Güler, C. Kaya, N. Kabay, M. Arda, Boron removal from seawater: State-of-the-art review, Desalination, 356 (2015) 85-93.
[43] M. Kurihara, Current Status and Future Trend of Dominant Commercial Reverse Osmosis Membranes, Membranes, 11 (2021).
[44] M.A. Alghoul, P. Poovanaesvaran, K. Sopian, M.Y. Sulaiman, Review of brackish water reverse osmosis (BWRO) system designs, Renewable and Sustainable Energy Reviews, 13 (2009) 2661-2667.
[45] E. Curcio, G.D. Profio, E. Fontananova, E. Drioli, 13 - Membrane technologies for seawater desalination and brackish water treatment, in: A. Basile, A. Cassano, N.K. Rastogi (Eds.) Advances in Membrane Technologies for Water Treatment, Woodhead Publishing, Oxford, 2015, pp. 411-441.

[46] T.J. Larson, G. Leitner, Desalting seawater and brackish water: a cost update, Desalination, 30 (1979) 525-539.
[47] P. Glueckstern, Y. Kantor, Seawater vs. brackish water desalting: Technology, operating problems and overall economics, Desalination, 44 (1983) 51-60.
[48] R.J. Petersen, Composite reverse osmosis and nanofiltration membranes, Journal of Membrane Science, 83 (1993) 81-150.
[49] E.M. Vrijenhoek, J.J. Waypa, Arsenic removal from drinking water by a "loose" nanofiltration membrane, Desalination, 130 (2000) 265-277.
[50] W.-J. Lau, A.F. Ismail, Polymeric nanofiltration membranes for textile dye wastewater treatment: Preparation, performance evaluation, transport modelling, and fouling control — a review, Desalination, 245 (2009) 321-348.
[51] M.F. Jimenez-Solomon, Q. Song, K.E. Jelfs, M. Munoz-Ibanez, A.G. Livingston, Polymer nanofilms with enhanced microporosity by interfacial polymerization, Nature materials, 15 (2016) 760-767.
[52] W. Fu, Y. Huang, L. Deng, J. Sun, S.-L. Li, Y. Hu, Ultra-thin microporous membranes based on macrocyclic pillar[n]arene for efficient organic solvent nanofiltration, Journal of Membrane Science, 655 (2022) 120583.
[53] W. Fu, W. Zhang, H. Chen, S.-L. Li, W. Shi, Y. Hu, A high-flux organic solvent nanofiltration membrane with binaphthol-based rigid-flexible microporous structures, Journal of Materials Chemistry A, 9 (2021) 7180-7189.
[54] C. Han, Q. Liu, Q. Xia, Y. Wang, Facilely cyclization-modified PAN nanofiber substrate of thin film composite membrane for ultrafast polar solvent separation, Journal of Membrane Science, 641 (2022) 119911.
[55] A. Yao, D. Hua, Z.F. Gao, J. Pan, A.-R. Ibrahim, D. Zheng, Y. Hong, Y. Liu, G. Zhan, Fabrication of organic solvent nanofiltration membrane using commercial PVDF substrate via interfacial polymerization on top of metal-organic frameworks interlayer, Journal of Membrane Science, 652 (2022) 120465.
[56] A. Yao, D. Hua, Y. Hong, J. Pan, X. Cheng, K.B. Tan, G. Zhan, Using Cu-TCPP Nanosheets as Interlayers for High-Performance Organic Solvent Nanofiltration Membranes, ACS Applied Nano Materials, 5 (2022) 18718-18729.
[57] V.N. Francis, J.Y. Chong, G. Yang, L. Che, R. Wang, Robust polyamide-PTFE hollow fibre membranes for harsh organic solvent nanofiltration, Chemical Engineering Journal, 452 (2023) 139333.
[58] Y. Lu, Z. Wang, W. Fang, Y. Zhu, Y. Zhang, J. Jin, Polyamide Thin Films Grown on PD/SWCNT-Interlayered-PTFE Microfiltration Membranes for High-Permeance Organic Solvent Nanofiltration, Industrial & Engineering Chemistry Research, 59 (2020) 22533-22540.
[59] Q. Shen, Y. Lin, P. Zhang, J. Segawa, Y. Jia, T. Istirokhatun, X. Cao, K. Guan, H. Matsuyama, Development of ultrathin polyamide nanofilm with enhanced inner-pore interconnectivity via graphene quantum dots-assembly intercalation for high-performance organic solvent nanofiltration, Journal of Membrane Science, 635 (2021) 119498.

[60] L. Deng, R.R. Gonzales, W. Fu, G. Xu, R. Takagi, Q. Song, S. Zhou, H. Matsuyama, Organic solvent separation using carbon nanotube-interlayered thin film composite membrane, Chemical Engineering Journal, 473 (2023) 145197.
[61] C. Liu, R. Takagi, T. Shintani, L. Cheng, K.L. Tung, H. Matsuyama, Organic Liquid Mixture Separation Using an Aliphatic Polyketone-Supported Polyamide Organic Solvent Reverse Osmosis (OSRO) Membrane, ACS applied materials & interfaces, 12 (2020) 7586-7594.
[62] Y. Li, Z. Guo, S. Li, B. Van der Bruggen, Interfacially Polymerized Thin-Film Composite Membranes for Organic Solvent Nanofiltration, Advanced Materials Interfaces, 8 (2020) 2001671.
[63] S. Loeb, S. Sourirajan, Sea Water Demineralization by Means of an Osmotic Membrane, in: Saline Water Conversion—II, AMERICAN CHEMICAL SOCIETY, 1963, pp. 117-132.
[64] S. Sourirajan, Separation of Hydrocarbon Liquids by Flow Under Pressure Through Porous Membranes, Nature, 203 (1964) 1348-1349.
[65] J. Kopecek, Performance of porous cellulose acetate membranes for the reverse osmosis separation of mixtures of organic liquids, Industrial & Engineering Chemistry Process Design and Development, 9 (1970) 5-12.
[66] W.J. Adam, B. Luke, P. Meares, The separation of mixtures of organic liquids by hyperfiltration, Journal of Membrane Science, 13 (1983) 127-149.
[67] Y. Fang, S. Sourirajan, T. Matsuura, Reverse osmosis separation of binary organic mixtures using cellulose acetate butyrate and aromatic polyamide membranes, Journal of Applied Polymer Science, 44 (1992) 1959-1969.
[68] B. Farnand, H. Sawatzky, Preferential Adsorption and Selective Permeation of Alcohol/Hydrocarbon Mixtures in Reverse Osmosis, Separation Science and Technology, 23 (1988) 1667-1681.
[69] J. Chau, P. Basak, K.K. Sirkar, Reverse osmosis separation of particular organic solvent mixtures by a perfluorodioxole copolymer membrane, Journal of Membrane Science, 563 (2018) 541-551.
[70] J. Chau, K.K. Sirkar, Organic solvent mixture separation during reverse osmosis and nanofiltration by a perfluorodioxole copolymer membrane, Journal of Membrane Science, 618 (2021) 118663.
[71] C. Liu, L. Cheng, T. Shintani, H. Matsuyama, AF2400/polyketone composite organic solvent reverse osmosis membrane for organic liquid separation, Journal of Membrane Science, 628 (2021) 119270.
[72] T. Tsuru, M. Miyawaki, T. Yoshioka, M. Asaeda, Reverse osmosis of nonaqueous solutions through porous silica-zirconia membranes, AIChE Journal, 52 (2006) 522-531.
[73] G. Dong, H. Nagasawa, L. Yu, M. Guo, M. Kanezashi, T. Yoshioka, T. Tsuru, Energy-efficient separation of organic liquids using organosilica membranes via a reverse osmosis route, Journal of Membrane Science, 597 (2020) 117758.
[74] H.Y. Jang, J.R. Johnson, Y. Ma, R. Mathias, D.A. Bhandari, R.P. Lively, Torlon®

hollow fiber membranes for organic solvent reverse osmosis separation of complex aromatic hydrocarbon mixtures, AIChE Journal, 65 (2019) e16757.
[75] R.R. Gonzales, N. Kato, H. Awaji, H. Matsuyama, Development of polydimethylsiloxane composite membrane for organic solvent separation, Separation and Purification Technology, 285 (2022) 120369.
[76] E.K. McGuinness, F. Zhang, Y. Ma, R.P. Lively, M.D. Losego, Vapor Phase Infiltration of Metal Oxides into Nanoporous Polymers for Organic Solvent Separation Membranes, Chemistry of Materials, 31 (2019) 5509-5518.
[77] C. Liu, R. Takagi, D. Saeki, L. Cheng, T. Shintani, T. Yasui, H. Matsuyama, Highly improved organic solvent reverse osmosis (OSRO) membrane for organic liquid mixture separation by simple heat treatment, Journal of Membrane Science, 618 (2021) 118710.
[78] W. Kushida, R.R. Gonzales, T. Shintani, A. Matsuoka, K. Nakagawa, T. Yoshioka, H. Matsuyama, Organic solvent mixture separation using fluorine-incorporated thin film composite reverse osmosis membrane, Journal of Materials Chemistry A, 10 (2022) 4146-4156.
[79] L. Ren, J. Chen, C. Wang, Q. Lu, J. Han, H. Wu, Triptycene based polyamide thin film composite membrane for high nanofiltration performance, Journal of the Taiwan Institute of Chemical Engineers, 101 (2019) 119-126.
[80] J.-b. Jin, D.-q. Liu, D.-d. Zhang, Y.-h. Yin, X.-y. Zhao, Y.-f. Zhang, Preparation of thin-film composite nanofiltration membranes with improved antifouling property and flux using 2,2′-oxybis-ethylamine, Desalination, 355 (2015) 141-146.
[81] K.H. Jung, H.J. Kim, M.H. Kim, H. Seo, J.-C. Lee, Superamphiphilic zwitterionic block copolymer surfactant-assisted fabrication of polyamide thin-film composite membrane with highly enhanced desalination performance, Journal of Membrane Science, 618 (2021) 118677.
[82] Y.R. He, J.T. Liu, G. Han, T.S. Chung, Novel thin-film composite nanofiltration membranes consisting of a zwitterionic co-polymer for selenium and arsenic removal, Journal of Membrane Science, 555 (2018) 299-306.
[83] Q.-F. An, W.-D. Sun, Q. Zhao, Y.-L. Ji, C.-J. Gao, Study on a novel nanofiltration membrane prepared by interfacial polymerization with zwitterionic amine monomers, Journal of Membrane Science, 431 (2013) 171-179.
[84] M.F. Jimenez Solomon, Y. Bhole, A.G. Livingston, High flux hydrophobic membranes for organic solvent nanofiltration (OSN)—Interfacial polymerization, surface modification and solvent activation, Journal of Membrane Science, 434 (2013) 193-203.
[85] J.Y. Sum, A.L. Ahmad, B.S. Ooi, Synthesis of thin film composite membrane using mixed dendritic poly(amidoamine) and void filling piperazine monomers, Journal of Membrane Science, 466 (2014) 183-191.
[86] S.L. Li, G. Chang, Y. Huang, K. Kinooka, Y. Chen, W. Fu, G. Gong, T. Yoshioka, N.B. McKeown, Y. Hu, 2,2'-Biphenol-based Ultrathin Microporous Nanofilms for Highly Efficient Molecular Sieving Separation, Angewandte Chemie, (2022).

[87] Z. Ali, B.S. Ghanem, Y. Wang, F. Pacheco, W. Ogieglo, H. Vovusha, G. Genduso, U. Schwingenschlogl, Y. Han, I. Pinnau, Finely Tuned Submicroporous Thin-Film Molecular Sieve Membranes for Highly Efficient Fluid Separations, Advanced materials, 32 (2020) e2001132.
[88] P.H.H. Duong, D.H. Anjum, K.-V. Peinemann, S.P. Nunes, Thin porphyrin composite membranes with enhanced organic solvent transport, Journal of Membrane Science, 563 (2018) 684-693.
[89] Q. Zhao, Y. Liu, Macrocycle crosslinked mesoporous polymers for ultrafast separation of organic dyes, Chemical Communications, 54 (2018) 7362-7365.
[90] T. Huang, T. Puspasari, S.P. Nunes, K.V. Peinemann, Ultrathin 2D-Layered Cyclodextrin Membranes for High- Performance Organic Solvent Nanofiltration, Advanced Functional Materials, 30 (2019).
[91] J. Liu, D. Hua, Y. Zhang, S. Japip, T.S. Chung, Precise Molecular Sieving Architectures with Janus Pathways for Both Polar and Nonpolar Molecules, Adv Mater, 30 (2018).
[92] L.F. Villalobos, T. Huang, K.V. Peinemann, Cyclodextrin Films with Fast Solvent Transport and Shape-Selective Permeability, Adv Mater, 29 (2017).
[93] S. Xiong, D.Y. Zhang, S. Mei, J. Liu, Y.S. Shi, Y. Wang, Thin film composite membranes containing intrinsic CD cavities in the selective layer, Journal of Membrane Science, 551 (2018) 294-304.
[94] Z. Zhai, C. Jiang, N. Zhao, W. Dong, P. Li, H. Sun, Q.J. Niu, Polyarylate membrane constructed from porous organic cage for high-performance organic solvent nanofiltration, Journal of Membrane Science, 595 (2020) 117505.
[95] Z. Yang, L. Li, C. Jiang, N. Zhao, S. Zhang, Y. Guo, Y. Chen, S. Xue, C. Ji, S. Zhao, R.R. Gonzales, H. Matsuyama, J. Xia, Q.J. Niu, Tailored thin film nanocomposite membrane incorporated with Noria for simultaneously overcoming the permeability-selectivity trade-off and the membrane fouling in nanofiltration process, Journal of Membrane Science, 640 (2021) 119863.
[96] M. Wang, W. Dong, Y. Guo, Z. Zhai, Z. Feng, Y. Hou, P. Li, Q.J. Niu, Positively charged nanofiltration membranes mediated by a facile polyethyleneimine-Noria interlayer deposition strategy, Desalination, 513 (2021) 114836.
[97] G. Zhu, M. Bao, Z. Liu, C. Gao, Preparation of spherical mesoporous aminopropyl-functionalized MCM-41 and its application in polyamide thin film nanocomposite reverse osmosis membranes, Desalination and Water Treatment, 57 (2016) 25411-25420.
[98] N. Akther, Y. Kawabata, S. Lim, T. Yoshioka, S. Phuntsho, H. Matsuyama, H.K. Shon, Effect of graphene oxide quantum dots on the interfacial polymerization of a thin-film nanocomposite forward osmosis membrane: An experimental and molecular dynamics study, Journal of Membrane Science, 630 (2021) 119309.
[99] L. Jin, Z. Wang, S. Zheng, B. Mi, Polyamide-crosslinked graphene oxide membrane for forward osmosis, Journal of Membrane Science, 545 (2018) 11-18.
[100] L. Ahmadian-Alam, H. Mahdavi, Fabrication of a novel hybrid poly(amide-co-

arylate)/MOF thin film membranes for organic solvent nanofiltration: optimization of membrane separation performance, Microporous and Mesoporous Materials, 328 (2021) 111443.
[101] Y. Liang, Y. Zhu, C. Liu, K.R. Lee, W.S. Hung, Z. Wang, Y. Li, M. Elimelech, J. Jin, S. Lin, Polyamide nanofiltration membrane with highly uniform sub-nanometre pores for sub-1 A precision separation, Nature Communications, 11 (2020) 2015.
[102] Y. Zhang, X. Miao, G. Pan, H. Shi, H. Yan, J. Xu, M. Guo, S. Li, Y. Zhang, Y. Liu, Highly improved permeation property of thin-film-composite polyamide membrane for water desalination, Journal of Polymer Research, 24 (2016).
[103] D. Ankoliya, B. Mehta, H. Raval, Advances in surface modification techniques of reverse osmosis membrane over the years, Separation Science and Technology, 54 (2018) 293-310.
[104] A. Venault, H.S. Yang, Y.C. Chiang, B.S. Lee, R.C. Ruaan, Y. Chang, Bacterial resistance control on mineral surfaces of hydroxyapatite and human teeth via surface charge-driven antifouling coatings, ACS applied materials & interfaces, 6 (2014) 3201-3210.
[105] L. Deng, S. Li, Y. Qin, L. Zhang, H. Chen, Z. Chang, Y. Hu, Fabrication of antifouling thin-film composite nanofiltration membrane via surface grafting of polyethyleneimine followed by zwitterionic modification, Journal of Membrane Science, 619 (2021) 118564.
[106] Y.-F. Mi, Q. Zhao, Y.-L. Ji, Q.-F. An, C.-J. Gao, A novel route for surface zwitterionic functionalization of polyamide nanofiltration membranes with improved performance, Journal of Membrane Science, 490 (2015) 311-320.
[107] Y. Hu, K. Lu, F. Yan, Y. Shi, P. Yu, S. Yu, S. Li, C. Gao, Enhancing the performance of aromatic polyamide reverse osmosis membrane by surface modification via covalent attachment of polyvinyl alcohol (PVA), Journal of Membrane Science, 501 (2016) 209-219.
[108] Q. Li, X. Pan, Z. Qu, X. Zhao, Y. Jin, H. Dai, B. Yang, X. Wang, Understanding the dependence of contact angles of commercially RO membranes on external conditions and surface features, Desalination, 309 (2013) 38-45.
[109] S. Belfer, R. Fainchtain, Y. Purinson, O. Kedem, Surface characterization by FTIR-ATR spectroscopy of polyethersulfone membranes-unmodified, modified and protein fouled, Journal of Membrane Science, 172 (2000) 113-124.
[110] N.H. Lin, M.-m. Kim, G.T. Lewis, Y. Cohen, Polymer surface nano-structuring of reverse osmosis membranes for fouling resistance and improved flux performance, Journal of Materials Chemistry, 20 (2010) 4642-4652.
[111] B.D. McCloskey, H.B. Park, H. Ju, B.W. Rowe, D.J. Miller, B.D. Freeman, A bioinspired fouling-resistant surface modification for water purification membranes, Journal of Membrane Science, 413-414 (2012) 82-90.
[112] H. Guo, Z. Yao, J. Wang, Z. Yang, X. Ma, C.Y. Tang, Polydopamine coating on a thin film composite forward osmosis membrane for enhanced mass transport and antifouling performance, Journal of Membrane Science, 551 (2018) 234-242.

[113] H. Karkhanechi, R. Takagi, H. Matsuyama, Biofouling resistance of reverse osmosis membrane modified with polydopamine, Desalination, 336 (2014) 87-96.
[114] E.M. Van Wagner, A.C. Sagle, M.M. Sharma, Y.-H. La, B.D. Freeman, Surface modification of commercial polyamide desalination membranes using poly(ethylene glycol) diglycidyl ether to enhance membrane fouling resistance, Journal of Membrane Science, 367 (2011) 273-287.
[115] S. Zhang, G. Qiu, Y.P. Ting, T.-S. Chung, Silver–PEGylated dendrimer nanocomposite coating for anti-fouling thin film composite membranes for water treatment, Colloids and Surfaces A: Physicochemical and Engineering Aspects, 436 (2013) 207-214.
[116] G. Kang, M. Liu, B. Lin, Y. Cao, Q. Yuan, A novel method of surface modification on thin-film composite reverse osmosis membrane by grafting poly(ethylene glycol), Polymer, 48 (2007) 1165-1170.
[117] Y. Zhou, S. Yu, C. Gao, X. Feng, Surface modification of thin film composite polyamide membranes by electrostatic self deposition of polycations for improved fouling resistance, Separation and Purification Technology, 66 (2009) 287-294.
[118] Y.-C. Chiang, Y.-Z. Hsub, R.-C. Ruaan, C.-J. Chuang, K.-L. Tung, Nanofiltration membranes synthesized from hyperbranched polyethyleneimine, Journal of Membrane Science, 326 (2009) 19-26.
[119] H. Mahdavi, M.T. Hosseinzade, T. Shahalizade, A. Kamyabi, A polyamide thin-film composite membrane modified by Michael addition grafting of hyperbranched poly(amine ester), Journal of Polymer Research, 24 (2017) 109.
[120] Z. Liu, X. An, C. Dong, S. Zheng, B. Mi, Y. Hu, Modification of thin film composite polyamide membranes with 3D hyperbranched polyglycerol for simultaneous improvement in their filtration performance and antifouling properties, Journal of Materials Chemistry A, 5 (2017) 23190-23197.
[121] X. Bao, Q. Wu, W. Shi, W. Wang, H. Yu, Z. Zhu, X. Zhang, Z. Zhang, R. Zhang, F. Cui, Polyamidoamine dendrimer grafted forward osmosis membrane with superior ammonia selectivity and robust antifouling capacity for domestic wastewater concentration, Water research, 153 (2019) 1-10.
[122] A. Sarkar, P.I. Carver, T. Zhang, A. Merrington, K.J. Bruza, J.L. Rousseau, S.E. Keinath, P.R. Dvornic, Dendrimer-based coatings for surface modification of polyamide reverse osmosis membranes, Journal of Membrane Science, 349 (2010) 421-428.
[123] C. Van Goethem, R. Verbeke, S. Hermans, R. Bernstein, I.F.J. Vankelecom, Controlled positioning of MOFs in interfacially polymerized thin-film nanocomposites, Journal of Materials Chemistry A, 4 (2016) 16368-16376.
[124] Y. Qian, H. Li, J. Lu, D. Lu, H. Jin, Z. Xia, Z. Yao, J. Wang, L. Zhang, C.Y. Tang, Inhibiting Polyamide Intrusion of Thin Film Composite Membranes: Strategies and Environmental Implications, Environmental science & technology, 57 (2023) 10860-10869.
[125] R. Dai, Z. Yang, Z. Qiu, L. Long, C.Y. Tang, Z. Wang, Distinct impact of substrate

hydrophilicity on performance and structure of TFC NF and RO polyamide membranes, Journal of Membrane Science, 662 (2022) 120966.
[126] E.-S. Kim, Y.J. Kim, Q. Yu, B. Deng, Preparation and characterization of polyamide thin-film composite (TFC) membranes on plasma-modified polyvinylidene fluoride (PVDF), Journal of Membrane Science, 344 (2009) 71-81.
[127] H.I. Kim, S.S. Kim, Plasma treatment of polypropylene and polysulfone supports for thin film composite reverse osmosis membrane, Journal of Membrane Science, 286 (2006) 193-201.
[128] H.I. Kim, S.S. Kim, Fabrication of reverse osmosis membrane via low temperature plasma polymerization, Journal of Membrane Science, 190 (2001) 21-33.
[129] S.-H. Park, S.J. Kwon, M.G. Shin, M.S. Park, J.S. Lee, C.H. Park, H. Park, J.-H. Lee, Polyethylene-supported high performance reverse osmosis membranes with enhanced mechanical and chemical durability, Desalination, 436 (2018) 28-38.
[130] Q. Shen, Y. Lin, T. Ueda, P. Zhang, Y. Jia, T. Istirokhatun, Q. Song, K. Guan, T. Yoshioka, H. Matsuyama, The underlying mechanism insights into support polydopamine decoration toward ultrathin polyamide membranes for high-performance reverse osmosis, Journal of Membrane Science, 646 (2022) 120269.
[131] K. Guan, Y. Sasaki, Y. Jia, R.R. Gonzales, P. Zhang, Y. Lin, Z. Li, H. Matsuyama, Interfacial polymerization of thin film selective membrane layers: Effect of polyketone substrates, Journal of Membrane Science, 640 (2021) 119801.
[132] M. Yasukawa, S. Mishima, Y. Tanaka, T. Takahashi, H. Matsuyama, Thin-film composite forward osmosis membrane with high water flux and high pressure resistance using a thicker void-free polyketone porous support, Desalination, 402 (2017) 1-9.
[133] Q. Zhang, Z. Zhang, L. Dai, H. Wang, S. Li, S. Zhang, Novel insights into the interplay between support and active layer in the thin film composite polyamide membranes, Journal of Membrane Science, 537 (2017) 372-383.
[134] Z. Yang, P.-F. Sun, X. Li, B. Gan, L. Wang, X. Song, H.-D. Park, C.Y. Tang, A Critical Review on Thin-Film Nanocomposite Membranes with Interlayered Structure: Mechanisms, Recent Developments, and Environmental Applications, Environmental science & technology, 54 (2020) 15563-15583.
[135] L. Long, C. Wu, Z. Yang, C.Y. Tang, Carbon Nanotube Interlayer Enhances Water Permeance and Antifouling Performance of Nanofiltration Membranes: Mechanisms and Experimental Evidence, Environmental science & technology, 56 (2022) 2656-2664.
[136] F. Wang, Z. Yang, C.Y. Tang, Modeling Water Transport in Interlayered Thin-Film Nanocomposite Membranes: Gutter Effect vs Funnel Effect, ACS ES&T Engineering, 2 (2022) 2023-2033.
[137] Y. Zhu, W. Xie, S. Gao, F. Zhang, W. Zhang, Z. Liu, J. Jin, Single-Walled Carbon Nanotube Film Supported Nanofiltration Membrane with a Nearly 10 nm Thick Polyamide Selective Layer for High-Flux and High-Rejection Desalination, Small, 12 (2016) 5034-5041.

[138] Z.Y. Zhou, Y.X. Hu, C. Boo, Z.Y. Liu, J.Q. Li, L.Y. Deng, X.C. An, High-Performance Thin-Film Composite Membrane with an Ultrathin Spray-Coated Carbon Nanotube Interlayer, Environmental Science & Technology Letters, 5 (2018) 243-248.
[139] G. Gong, P. Wang, Z. Zhou, Y. Hu, New Insights into the Role of an Interlayer for the Fabrication of Highly Selective and Permeable Thin-Film Composite Nanofiltration Membrane, ACS applied materials & interfaces, 11 (2019) 7349-7356.
[140] Z. Yang, F. Wang, H. Guo, L.E. Peng, X.H. Ma, X.X. Song, Z. Wang, C.Y. Tang, Mechanistic Insights into the Role of Polydopamine Interlayer toward Improved Separation Performance of Polyamide Nanofiltration Membranes, Environmental science & technology, 54 (2020) 11611-11621.
[141] Q.Q. Song, Y.Q. Lin, T. Ueda, T. Istirokhatun, Q. Shen, K.C. Guan, T. Yoshioka, H. Matsuyama, Mechanism insights into the role of the support mineralization layer toward ultrathin polyamide nanofilms for ultrafast molecular separation, Journal of Materials Chemistry A, 9 (2021) 26159-26171.
[142] L.-x. Dong, X.-c. Huang, Z. Wang, Z. Yang, X.-m. Wang, C.Y. Tang, A thin-film nanocomposite nanofiltration membrane prepared on a support with in situ embedded zeolite nanoparticles, Separation and Purification Technology, 166 (2016) 230-239.
[143] L. Sarango, L. Paseta, M. Navarro, B. Zornoza, J. Coronas, Controlled deposition of MOFs by dip-coating in thin film nanocomposite membranes for organic solvent nanofiltration, Journal of Industrial and Engineering Chemistry, 59 (2018) 8-16.
[144] G.S. Lai, W.J. Lau, P.S. Goh, A.F. Ismail, Y.H. Tan, C.Y. Chong, R. Krause-Rehberg, S. Awad, Tailor-made thin film nanocomposite membrane incorporated with graphene oxide using novel interfacial polymerization technique for enhanced water separation, Chemical Engineering Journal, 344 (2018) 524-534.
[145] C. Cheng, P. Li, K. Shen, T. Zhang, X. Cao, B. Wang, X. Wang, B.S. Hsiao, Integrated polyamide thin-film nanofibrous composite membrane regulated by functionalized interlayer for efficient water/isopropanol separation, Journal of Membrane Science, 553 (2018) 70-81.
[146] X. Wu, M. Ding, H. Xu, W. Yang, K. Zhang, H. Tian, H. Wang, Z. Xie, Scalable Ti(3)C(2)T(x) MXene Interlayered Forward Osmosis Membranes for Enhanced Water Purification and Organic Solvent Recovery, ACS Nano, 14 (2020) 9125-9135.
[147] M.J. Park, C. Wang, D.H. Seo, R.R. Gonzales, H. Matsuyama, H.K. Shon, Inkjet printed single walled carbon nanotube as an interlayer for high performance thin film composite nanofiltration membrane, Journal of Membrane Science, 620 (2021) 118901.
[148] S. Gao, Y. Zhu, Y. Gong, Z. Wang, W. Fang, J. Jin, Ultrathin Polyamide Nanofiltration Membrane Fabricated on Brush-Painted Single-Walled Carbon Nanotube Network Support for Ion Sieving, ACS Nano, 13 (2019) 5278-5290.
[149] H. Gao, Y. Chen, Hybrid Dimensional MXene/CNC Framework-Regulated Nanofiltration Membrane with High Separation Performance, ACS ES&T Water, (2022).
[150] J.-J. Wang, H.-C. Yang, M.-B. Wu, X. Zhang, Z.-K. Xu, Nanofiltration membranes with cellulose nanocrystals as an interlayer for unprecedented performance,

Journal of Materials Chemistry A, 5 (2017) 16289-16295.
[151] L. Bai, J. Ding, H. Wang, N. Ren, G. Li, H. Liang, High-performance nanofiltration membranes with a sandwiched layer and a surface layer for desalination and environmental pollutant removal, Science of The Total Environment, 743 (2020) 140766.
[152] S. Dhaka, R. Kumar, A. Deep, M.B. Kurade, S.-W. Ji, B.-H. Jeon, Metal–organic frameworks (MOFs) for the removal of emerging contaminants from aquatic environments, Coordination Chemistry Reviews, 380 (2019) 330-352.
[153] J.R. Li, J. Sculley, H.C. Zhou, Metal-organic frameworks for separations, Chemical reviews, 112 (2012) 869-932.
[154] L. Wang, M. Fang, J. Liu, J. He, J. Li, J. Lei, Layer-by-Layer Fabrication of High-Performance Polyamide/ZIF-8 Nanocomposite Membrane for Nanofiltration Applications, ACS applied materials & interfaces, 7 (2015) 24082-24093.
[155] M. Navarro, J. Benito, L. Paseta, I. Gascon, J. Coronas, C. Tellez, Thin-Film Nanocomposite Membrane with the Minimum Amount of MOF by the Langmuir-Schaefer Technique for Nanofiltration, ACS applied materials & interfaces, 10 (2018) 1278-1287.
[156] L. Paseta, D. Antorán, J. Coronas, C. Téllez, 110th Anniversary: Polyamide/Metal–Organic Framework Bilayered Thin Film Composite Membranes for the Removal of Pharmaceutical Compounds from Water, Industrial & Engineering Chemistry Research, 58 (2019) 4222-4230.
[157] R. Sun, Y. Lv, X. Zhang, J. Zhao, Z. Qian, Q. Lan, Z. Wang, F. He, T. Liu, Silicification-interlayered nanofiber substrates regulated crumpled ultrathin polyamide nanofilms for highly enhanced nanofiltration, Journal of Membrane Science, 672 (2023) 121476.
[158] B. Yuan, S. Zhao, P. Hu, J. Cui, Q.J. Niu, Asymmetric polyamide nanofilms with highly ordered nanovoids for water purification, Nat Commun, 11 (2020) 6102.
[159] S. Zhou, K. Guan, Z. Wang, Q. Song, Z. Li, P. Xu, L. Deng, S. Xiang, H. Matsuyama, Confined and mediated intercalation of nanoparticles in graphene oxide membrane to fine-tune desalination performance, Chemical Engineering Journal, 465 (2023) 143005.
[160] K. Guan, Y. Jia, Y. Lin, S. Wang, H. Matsuyama, Chemically Converted Graphene Nanosheets for the Construction of Ion-Exclusion Nanochannel Membranes, Nano Lett, 21 (2021) 3495-3502.
[161] H.-g. Choi, A.A. Shah, S.-E. Nam, Y.-I. Park, H. Park, Thin-film composite membranes comprising ultrathin hydrophilic polydopamine interlayer with graphene oxide for forward osmosis, Desalination, 449 (2019) 41-49.
[162] B. Li, X.-X. Ke, L.-B. Zhong, R.-X. Wu, Z.-H. Yuan, J.-J. Fan, Y.-M. Zheng, Super-hydrophilic nanofiber substrate supported forward osmosis membrane with less polyamide layer defects by polydopamine-graphene oxide modification for high salinity desulfurization wastewater desalination, Journal of Membrane Science, 659 (2022) 120767.

[163] L. Huang, Y. Li, Q. Zhou, W. Yuan, G. Shi, Graphene oxide membranes with tunable semipermeability in organic solvents, Adv Mater, 27 (2015) 3797-3802.
[164] Z. Wang, Q. Tu, S. Zheng, J.J. Urban, S. Li, B. Mi, Understanding the Aqueous Stability and Filtration Capability of MoS2 Membranes, Nano Letters, 17 (2017) 7289-7298.
[165] Y. Li, C. Li, S. Li, B. Su, L. Han, B. Mandal, Graphene oxide (GO)-interlayered thin-film nanocomposite (TFN) membranes with high solvent resistance for organic solvent nanofiltration (OSN), Journal of Materials Chemistry A, 7 (2019) 13315-13330.
[166] M. Naguib, V.N. Mochalin, M.W. Barsoum, Y. Gogotsi, 25th anniversary article: MXenes: a new family of two-dimensional materials, Adv Mater, 26 (2014) 992-1005.
[167] M. Naguib, O. Mashtalir, J. Carle, V. Presser, J. Lu, L. Hultman, Y. Gogotsi, M.W. Barsoum, Two-dimensional transition metal carbides, ACS nano, 6 (2012) 1322-1331.
[168] Z. Ahmed, F. Rehman, U. Ali, A. Ali, M. Iqbal, K.H. Thebo, Recent Advances in MXene-based Separation Membranes, ChemBioEng Reviews, 8 (2021) 110-120.
[169] H.E. Karahan, K. Goh, C.J. Zhang, E. Yang, C. Yildirim, C.Y. Chuah, M.G. Ahunbay, J. Lee, S.B. Tantekin-Ersolmaz, Y. Chen, T.H. Bae, MXene Materials for Designing Advanced Separation Membranes, Adv Mater, 32 (2020) e1906697.
[170] P.-F. Sun, Z. Yang, X. Song, J.H. Lee, C.Y. Tang, H.-D. Park, Interlayered Forward Osmosis Membranes with Ti3C2Tx MXene and Carbon Nanotubes for Enhanced Municipal Wastewater Concentration, Environmental science & technology, 55 (2021) 13219-13230.
[171] P.-F. Sun, P. Sarkar, E.-T. Yun, J.H. Lee, C.Y. Tang, H.-D. Park, Multi-layer structure toward simultaneous enhancement of forward osmosis membrane separation performance and anti-biofouling property, Journal of Membrane Science, 683 (2023) 121804.
[172] F. Li, T.D. Liu, S. Xie, J. Guan, S. Zhang, 2D Metal-Organic Framework-Based Thin-Film Nanocomposite Membranes for Reverse Osmosis and Organic Solvent Nanofiltration, ChemSusChem, 14 (2021) 2452-2460.
[173] W.F. Chan, E. Marand, S.M. Martin, Novel zwitterion functionalized carbon nanotube nanocomposite membranes for improved RO performance and surface anti-biofouling resistance, Journal of Membrane Science, 509 (2016) 125-137.
[174] M.-B. Wu, Y. Lv, H.-C. Yang, L.-F. Liu, X. Zhang, Z.-K. Xu, Thin film composite membranes combining carbon nanotube intermediate layer and microfiltration support for high nanofiltration performances, Journal of Membrane Science, 515 (2016) 238-244.
[175] A.A. Shah, Y.H. Cho, H.-g. Choi, S.-E. Nam, J.F. Kim, Y. Kim, Y.-I. Park, H. Park, Facile integration of halloysite nanotubes with bioadhesive as highly permeable interlayer in forward osmosis membranes, Journal of Industrial and Engineering Chemistry, 73 (2019) 276-285.
[176] L. Ye, L. Wang, Z. Wei, S. Zhou, Z. Yao, F. Fan, Y. Mei, Thin film composite nanofiltration membrane with tannic acid-Fe(III) complexes functionalized CNTs interlayer toward energy efficient remediation of groundwater, Desalination, 552 (2023)

116438.
[177] Z. Yang, Z.-w. Zhou, H. Guo, Z. Yao, X.-h. Ma, X. Song, S.-P. Feng, C.Y. Tang, Tannic Acid/Fe3+ Nanoscaffold for Interfacial Polymerization: Toward Enhanced Nanofiltration Performance, Environmental science & technology, 52 (2018) 9341-9349.
[178] D. Ma, Z. Zhang, S. Xiong, J. Zhou, Y. Wang, Additive manufacturing of defect-healing polyamide membranes for fast and robust desalination, Journal of Membrane Science, 671 (2023) 121407.
[179] Y. Yang, Y. Xu, Z. Liu, H. Huang, X. Fan, Y. Wang, Y. Song, C. Song, Preparation and characterization of high-performance electrospun forward osmosis membrane by introducing a carbon nanotube interlayer, Journal of Membrane Science, 616 (2020) 118563.
[180] X. Song, S. Li, W. Zhang, H. Liu, J. Jiang, C. Zhang, Constructing semi-oriented single-walled carbon nanotubes artificial water channels for realized efficient desalination of nanocomposite RO membranes, Journal of Membrane Science, (2022) 121029.
[181] A. Güvensoy-Morkoyun, S. Kürklü-Kocaoğlu, C. Yıldırım, S. Velioğlu, H.E. Karahan, T.-H. Bae, Ş.B. Tantekin-Ersolmaz, Carbon nanotubes integrated into polyamide membranes by support pre-infiltration improve the desalination performance, Carbon, 185 (2021) 546-557.
[182] M.A. Shannon, P.W. Bohn, M. Elimelech, J.G. Georgiadis, B.J. Mariñas, A.M. Mayes, Science and technology for water purification in the coming decades, Nature, 452 (2008) 301-310.
[183] V.G. Gude, Desalination and water reuse to address global water scarcity, Reviews in Environmental Science and Bio/Technology, 16 (2017) 591-609.
[184] M.T.H. van Vliet, E.R. Jones, M. Flörke, W.H.P. Franssen, N. Hanasaki, Y. Wada, J.R. Yearsley, Global water scarcity including surface water quality and expansions of clean water technologies, Environmental Research Letters, 16 (2021) 024020.
[185] C.A. Quist-Jensen, F. Macedonio, E. Drioli, Membrane technology for water production in agriculture: Desalination and wastewater reuse, Desalination, 364 (2015) 17-32.
[186] T.-S. Chung, D. Zhao, J. Gao, K. Lu, C. Wan, M. Weber, C. Maletzko, Emerging R&D on membranes and systems for water reuse and desalination, Chinese Journal of Chemical Engineering, 27 (2019) 1578-1585.
[187] B. Nicolaisen, Developments in membrane technology for water treatment, Desalination, 153 (2003) 355-360.
[188] L.F. Greenlee, D.F. Lawler, B.D. Freeman, B. Marrot, P. Moulin, Reverse osmosis desalination: Water sources, technology, and today's challenges, Water Research, 43 (2009) 2317-2348.
[189] I.G. Wenten, Khoiruddin, Reverse osmosis applications: Prospect and challenges, Desalination, 391 (2016) 112-125.
[190] W.J. Lau, A.F. Ismail, N. Misdan, M.A. Kassim, A recent progress in thin film

composite membrane: A review, Desalination, 287 (2012) 190-199.
[191] C. Ji, Z. Zhai, C. Jiang, P. Hu, S. Zhao, S. Xue, Z. Yang, T. He, Q.J. Niu, Recent advances in high-performance TFC membranes: A review of the functional interlayers, Desalination, 500 (2021) 114869.
[192] Z. Zhang, G. Kang, H. Yu, Y. Jin, Y. Cao, From reverse osmosis to nanofiltration: Precise control of the pore size and charge of polyamide membranes via interfacial polymerization, Desalination, 466 (2019) 16-23.
[193] R. Reis, M. Duke, A. Merenda, B. Winther-Jensen, L. Puskar, M.J. Tobin, J.D. Orbell, L.F. Dumée, Customizing the surface charge of thin-film composite membranes by surface plasma thin film polymerization, Journal of Membrane Science, 537 (2017) 1-10.
[194] T. Ishigami, K. Amano, A. Fujii, Y. Ohmukai, E. Kamio, T. Maruyama, H. Matsuyama, Fouling reduction of reverse osmosis membrane by surface modification via layer-by-layer assembly, Separation and Purification Technology, 99 (2012) 1-7.
[195] X. Zhu, D. Jańczewski, S. Guo, S.S.C. Lee, F.J. Parra Velandia, S.L.-M. Teo, T. He, S.R. Puniredd, G.J. Vancso, Polyion Multilayers with Precise Surface Charge Control for Antifouling, ACS Applied Materials & Interfaces, 7 (2015) 852-861.
[196] Y. Wang, Q. Wang, Q.-C. Xia, W.-J. Yang, X.-X. Wang, S.-P. Sun, W. Xing, Nanocapsule controlled interfacial polymerization finely tunes membrane surface charge for precise molecular sieving, Chemical Engineering Journal, 409 (2021) 128198.
[197] S.-Y. Wang, R.R. Gonzales, P. Zhang, T. Istirokhatun, R. Takagi, A. Motoyama, L.-F. Fang, H. Matsuyama, Surface charge control of poly(methyl methacrylate-co-dimethyl aminoethyl methacrylate)-based membrane for improved fouling resistance, Separation and Purification Technology, 279 (2021) 119778.
[198] J. Li, R.R. Gonzales, R. Takagi, X. Yao, P. Zhang, T. Istirokhatun, J. Zhang, H. Matsuyama, Surface modification of thin film composite forward osmosis membrane using tris(2-aminoethyl)amine for enhanced ammonium recovery, Desalination, 541 (2022) 116002.
[199] Y. Yin, Y. Zhao, C. Li, R. Wang, Fabrication of polyamide hollow fiber nanofiltration membrane with intensified positive surface charge density via a secondary interfacial polymerization, Journal of Membrane Science, 682 (2023) 121778.
[200] J.R. Werber, S.K. Bull, M. Elimelech, Acyl-chloride quenching following interfacial polymerization to modulate the water permeability, selectivity, and surface charge of desalination membranes, Journal of Membrane Science, 535 (2017) 357-364.
[201] X. Cheng, Y. Peng, S. Li, B. Su, Alginate hydrogel interlayer assisted interfacial polymerization for enhancing the separation performance of reverse osmosis membrane, Journal of Membrane Science, 638 (2021) 119680.
[202] R.R. Gonzales, Y. Sasaki, T. Istirokhatun, J. Li, H. Matsuyama, Ammonium enrichment and recovery from synthetic and real industrial wastewater by amine-modified thin film composite forward osmosis membranes, Separation and Purification

Technology, 297 (2022) 121534.
[203] X. Yao, R.R. Gonzales, Y. Sasaki, Y. Lin, Q. Shen, P. Zhang, T. Shintani, K. Nakagawa, H. Matsuyama, Surface modification of FO membrane for improving ammoniacal nitrogen (NH4+-N) rejection: Investigating the factors influencing NH4+-N rejection, Journal of Membrane Science, 650 (2022) 120429.
[204] R.R. Gonzales, L. Zhang, K.C. Guan, M.J. Park, S. Phuntsho, A. Abdel-Wahab, H. Matsuyama, H.K. Shon, Aliphatic polyketone-based thin film composite membrane with mussel-inspired polydopamine intermediate layer for high performance osmotic power generation, Desalination, 516 (2021) 115222.
[205] X. You, K. Xiao, H. Wu, Y. Li, R. Li, J. Yuan, R. Zhang, Z. Zhang, X. Liang, J. Shen, Z. Jiang, Electrostatic-modulated interfacial polymerization toward ultra-permselective nanofiltration membranes, iScience, 24 (2021) 102369.
[206] M. Kahrizi, R.R. Gonzales, L. Kong, H. Matsuyama, P. Lu, J. Lin, S. Zhao, Significant roles of substrate properties in forward osmosis membrane performance: A review, Desalination, 528 (2022) 115615.
[207] A.K. Ghosh, E.M.V. Hoek, Impacts of support membrane structure and chemistry on polyamide-polysulfone interfacial composite membranes, Journal of Membrane Science, 336 (2009) 140-148.
[208] L. Deng, Q. Wang, X. An, Z. Li, Y. Hu, Towards enhanced antifouling and flux performances of thin-film composite forward osmosis membrane via constructing a sandwich-like carbon nanotubes-coated support, Desalination, 479 (2020) 114311.
[209] R.R. Gonzales, A. Abdel-Wahab, D.S. Han, H. Matsuyama, S. Phuntsho, H.K. Shon, Control of the antagonistic effects of heat-assisted chlorine oxidative degradation on pressure retarded osmosis thin film composite membrane surface, Journal of Membrane Science, 636 (2021) 119567.
[210] G.-Y. Chai, W.B. Krantz, Formation and characterization of polyamide membranes via interfacial polymerization, Journal of Membrane Science, 93 (1994) 175-192.
[211] Y. Jin, S. Liang, Z. Wu, Z. Cai, N. Zhao, Simulating the growth process of aromatic polyamide layer by monomer concentration controlling method, Applied Surface Science, 314 (2014) 286-291.
[212] K. Grzebyk, M.D. Armstrong, O. Coronell, Accessing greater thickness and new morphology features in polyamide active layers of thin-film composite membranes by reducing restrictions in amine monomer supply, Journal of Membrane Science, 644 (2022) 120112.
[213] C. Kong, T. Shintani, T. Kamada, V. Freger, T. Tsuru, Co-solvent-mediated synthesis of thin polyamide membranes, Journal of Membrane Science, 384 (2011) 10-16.
[214] Q. Gan, L.E. Peng, H. Guo, Z. Yang, C.Y. Tang, Cosolvent-Assisted Interfacial Polymerization toward Regulating the Morphology and Performance of Polyamide Reverse Osmosis Membranes: Increased m-Phenylenediamine Solubility or Enhanced Interfacial Vaporization?, Environmental science & technology, 56 (2022) 10308-

10316.
[215] G. He, X. He, X. Wang, C. Chang, J. Zhao, Z. Li, H. Wu, Z. Jiang, A highly proton-conducting, methanol-blocking Nafion composite membrane enabled by surface-coating crosslinked sulfonated graphene oxide, Chem Commun (Camb), 52 (2016) 2173-2176.
[216] W. Fu, L. Deng, M. Hu, Z. Mai, G. Xu, Y. Shi, K. Guan, R.R. Gonzales, A. Matsuoka, H. Matsuyama, Polyamide composite membrane with 3D honeycomb-like structure via acetone-regulated interfacial polymerization for high-efficiency organic solvent nanofiltration, Journal of Membrane Science, 679 (2023) 121711.
[217] E.-S. Kim, Q. Yu, B. Deng, Plasma surface modification of nanofiltration (NF) thin-film composite (TFC) membranes to improve anti organic fouling, Applied Surface Science, 257 (2011) 9863-9871.
[218] L. Zou, I. Vidalis, D. Steele, A. Michelmore, S.P. Low, J.Q.J.C. Verberk, Surface hydrophilic modification of RO membranes by plasma polymerization for low organic fouling, Journal of Membrane Science, 369 (2011) 420-428.
[219] J.H. Jhaveri, Z.V.P. Murthy, A comprehensive review on anti-fouling nanocomposite membranes for pressure driven membrane separation processes, Desalination, 379 (2016) 137-154.
[220] K. Boussu, A. Belpaire, A. Volodin, C. Van Haesendonck, P. Van der Meeren, C. Vandecasteele, B. Van der Bruggen, Influence of membrane and colloid characteristics on fouling of nanofiltration membranes, Journal of Membrane Science, 289 (2007) 220-230.
[221] H.A. Le Phuong, C.F. Blanford, G. Szekely, Reporting the unreported: the reliability and comparability of the literature on organic solvent nanofiltration, Green Chemistry, 22 (2020) 3397-3409.
[222] M.L. Jue, D.-Y. Koh, B.A. McCool, R.P. Lively, Enabling widespread use of microporous materials for challenging organic solvent separations, Chemistry of Materials, 29 (2017) 9863-9876.
[223] C. Liu, G. Dong, T. Tsuru, H. Matsuyama, Organic solvent reverse osmosis membranes for organic liquid mixture separation: A review, Journal of Membrane Science, 620 (2021) 118882.
[224] J.F. Kim, G. Szekely, M. Schaepertoens, I.B. Valtcheva, M.F. Jimenez-Solomon, A.G. Livingston, In Situ Solvent Recovery by Organic Solvent Nanofiltration, ACS Sustainable Chemistry & Engineering, 2 (2014) 2371-2379.
[225] G. Xu, Y.-H. Chiao, W. Fu, L. Deng, M. Hu, K. Guan, R.R. Gonzales, H. Matsuyama, Temperature-modulated formation of polyamide layer for enhanced organic solvent reverse osmosis (OSRO) performance, Journal of Membrane Science, 682 (2023) 121793.
[226] N. Kato, R.R. Gonzales, A. Nishitani, Y. Negi, T. Ono, H. Matsuyama, Single-step preparation of nanocomposite polyamide 6 hollow fiber membrane with integrally skinned asymmetric structure for organic solvent nanofiltration, Colloids and Surfaces A: Physicochemical and Engineering Aspects, 620 (2021) 126538.

[227] D. Ren, S. Ren, Y. Lin, J. Xu, X. Wang, Recent developments of organic solvent resistant materials for membrane separations, Chemosphere, 271 (2021) 129425.
[228] I. Sereewatthanawut, F.W. Lim, Y.S. Bhole, D. Ormerod, A. Horvath, A.T. Boam, A.G. Livingston, Demonstration of molecular purification in polar aprotic solvents by organic solvent nanofiltration, Organic Process Research & Development, 14 (2010) 600-611.
[229] M. Priske, M. Lazar, C. Schnitzer, G. Baumgarten, Recent applications of organic solvent nanofiltration, Chemie Ingenieur Technik, 88 (2016) 39-49.
[230] M. Liao, Y. Zhu, G. Gong, L. Qiao, Thin-Film Composite Membranes with a Carbon Nanotube Interlayer for Organic Solvent Nanofiltration, Membranes, 12 (2022) 817.
[231] Z. Nanyan, X. Jining, K.V. Vijay, Functionalization of carbon nanotubes by potassium permanganate assisted with phase transfer catalyst, Smart Materials and Structures, 11 (2002) 962.
[232] R.A. Moraes, C.F. Matos, E.G. Castro, W.H. Schreiner, M.M. Oliveira, A.J. Zarbin, The effect of different chemical treatments on the structure and stability of aqueous dispersion of iron-and iron oxide-filled multi-walled carbon nanotubes, Journal of the Brazilian Chemical Society, 22 (2011) 2191-2201.
[233] B. Kumanek, Ł. Przypis, P.S. Wróbel, M. Krzywiecki, K.Z. Walczak, D. Janas, Convenient but powerful method to dope single-walled carbon nanotube films with iodonium salts, Applied Nanoscience, 10 (2019) 529-539.
[234] N. Ataollahi, K. Vezzù, G. Nawn, G. Pace, G. Cavinato, F. Girardi, P. Scardi, V. Di Noto, R. Di Maggio, A Polyketone-based Anion Exchange Membrane for Electrochemical Applications: Synthesis and Characterization, Electrochimica Acta, 226 (2017) 148-157.
[235] C.Y. Tang, Y.-N. Kwon, J.O. Leckie, Probing the nano-and micro-scales of reverse osmosis membranes—A comprehensive characterization of physiochemical properties of uncoated and coated membranes by XPS, TEM, ATR-FTIR, and streaming potential measurements, Journal of Membrane Science, 287 (2007) 146-156.
[236] G. Socrates, “Infrared Characteristic Group Frequencies”, Wiley-Interscience, Chichester, 1980.
[237] S. Belfer, Y. Purinson, O. Kedem, Surface modification of commercial polyamide reverse osmosis membranes by radical grafting: An ATR-FTIR study, Acta Polymerica, 49 (1998) 574-582.
[238] D.J. Skrovanek, P.C. Painter, M.M. Coleman, Hydrogen bonding in polymers. 2. Infrared temperature studies of nylon 11, Macromolecules, 19 (1986) 699-705.
[239] D.J. Skrovanek, S.E. Howe, P.C. Painter, M.M. Coleman, Hydrogen bonding in polymers: infrared temperature studies of an amorphous polyamide, Macromolecules, 18 (1985) 1676-1683.
[240] R. Modi, R. Mehta, H. Brahmbhatt, A. Bhattacharya, Tailor Made Thin Film Composite Membranes: Potentiality Towards Removal of Hydroquinone from Water, Journal of Polymers and the Environment, 25 (2016) 1140-1146.

[241] V. Freger, J. Gilron, S. Belfer, TFC polyamide membranes modified by grafting of hydrophilic polymers: an FT-IR/AFM/TEM study, Journal of Membrane Science, 209 (2002) 283-292.
[242] J. Wang, S. Zhang, P. Wu, W. Shi, Z. Wang, Y. Hu, In Situ Surface Modification of Thin-Film Composite Polyamide Membrane with Zwitterions for Enhanced Chlorine Resistance and Transport Properties, ACS applied materials & interfaces, 11 (2019) 12043-12052.
[243] M. Miwa, A. Nakajima, A. Fujishima, K. Hashimoto, T. Watanabe, Effects of the Surface Roughness on Sliding Angles of Water Droplets on Superhydrophobic Surfaces, Langmuir, 16 (2000) 5754-5760.
[244] L. Xia, J.R. McCutcheon, Understanding the influence of solvents on the intrinsic properties and performance of polyamide thin film composite membranes, Separation and Purification Technology, 238 (2020) 116398.
[245] Y. Li, J. Zhu, S. Li, Z. Guo, B. Van der Bruggen, Flexible Aliphatic–Aromatic Polyamide Thin Film Composite Membrane for Highly Efficient Organic Solvent Nanofiltration, ACS Applied Materials & Interfaces, 12 (2020) 31962-31974.
[246] B. Liang, X. He, J. Hou, L. Li, Z. Tang, Membrane Separation in Organic Liquid: Technologies, Achievements, and Opportunities, Advanced materials, 31 (2019) e1806090.
[247] P. Alafogianni, K. Dassios, S. Farmaki, S.K. Antiohos, T.E. Matikas, N.M. Barkoula, On the efficiency of UV–vis spectroscopy in assessing the dispersion quality in sonicated aqueous suspensions of carbon nanotubes, Colloids and Surfaces A: Physicochemical and Engineering Aspects, 495 (2016) 118-124.
[248] C.M. Hansen, Hansen solubility parameters: a user's handbook, Second ed., CRC press, 2007.
[249] M. Yasukawa, S. Mishima, M. Shibuya, D. Saeki, T. Takahashi, T. Miyoshi, H. Matsuyama, Preparation of a forward osmosis membrane using a highly porous polyketone microfiltration membrane as a novel support, Journal of Membrane Science, 487 (2015) 51-59.
[250] Q. Ye, F. Zhou, W. Liu, Bioinspired catecholic chemistry for surface modification, Chemical Society reviews, 40 (2011) 4244.
[251] C.-C. Ho, S.-J. Ding, Structure, Properties and Applications of Mussel-Inspired Polydopamine, Journal of Biomedical Nanotechnology, 10 (2014) 3063-3084.
[252] S.M.D. Haeshin Lee, William M. Miller, Phillip B. Messersmith, Mussel-Inspired Surface Chemistry for Multifunctional Coatings, Science, 318 (2007) 426-430.
[253] Y. Liu, K. Ai, L. Lu, Polydopamine and its derivative materials: synthesis and promising applications in energy, environmental, and biomedical fields, Chemical reviews, 114 (2014) 5057-5115.
[254] H. Lee, N.F. Scherer, P.B. Messersmith, Single-molecule mechanics of mussel adhesion, Proceedings of the National Academy of Sciences of the United States of America, 103 (2006) 12999-13003.
[255] S.J. Vanhook, M.F. Schatz, J.B. Swift, W.D. McCormick, H.L. Swinney, Long-

wavelength surface-tension-driven Bénard convection: experiment and theory, Journal of Fluid Mechanics, 345 (1997) 45-78.
[256] S.M. Aharoni, The solubility parameters of aromatic polyamides, Journal of Applied Polymer Science, 45 (1992) 813-817.
[257] L.D.C. Baldi, E.T. Iamazaki, T.D.Z. Atvars, Evaluation of the polarity of polyamide surfaces using the fluorescence emission of pyrene, Dyes and Pigments, 76 (2008) 669-676.
[258] B. Van der Bruggen, J. Schaep, D. Wilms, C. Vandecasteele, Influence of molecular size, polarity and charge on the retention of organic molecules by nanofiltration, Journal of Membrane Science, 156 (1999) 29-41.
[259] I.W.G.o.t.E.o.C.R.t. Humans, Methyl tert-butyl ether, in: E. Heseltine (Ed.) Some Chemicals that Cause Tumours of the Kidney or Urinary Bladder in Rodents and Some Other Substances, International Agency for Research on Cancer, France, 1999, pp. 339-341.
[260] S. He, W. Fan, H. Huang, J. Gao, D. Xu, Y. Ma, L. Zhang, Y. Wang, Separation of the Azeotropic Mixture Methanol and Toluene Using Extractive Distillation: Entrainer Determination, Vapor-Liquid Equilibrium Measurement, and Modeling, ACS omega, 6 (2021) 34736-34743.
[261] S. Sridhar, B. Smitha, A. Shaik, Pervaporation-Based Separation of Methanol/MTBE Mixtures—A Review, Separation & Purification Reviews, 34 (2005) 1-33.
[262] S. Mandal, V.G. Pangarkar, Separation of methanol–benzene and methanol–toluene mixtures by pervaporation: effects of thermodynamics and structural phenomenon, Journal of Membrane Science, 201 (2002) 175-190.
[263] C. Hao, Y. Wen, B. Wang, F. Ahmad, Y. Liu, H. Li, W. Huang, Synthesis of HTLcs modified by K3PO4 for side chain alkylation of toluene with methanol, Green Energy & Environment, 6 (2021) 961-967.
[264] T. Sano, M. Hasegawa, Y. Kawakami, H. Yanagishita, Separation of methanolrmmethyl-tert-butyl ether mixture by pervaporation using silicalite membrane, Journal of Membrane Science, 107 (1995) 193-196.
[265] J. Wang, P.A.G. Cormack, D.C. Sherrington, E. Khoshdel, Monodisperse, Molecularly Imprinted Polymer Microspheres Prepared by Precipitation Polymerization for Affinity Separation Applications, Angewandte Chemie, 115 (2003) 5494-5496.
[266] O.K. Castell, C.J. Allender, D.A. Barrow, Novel biphasic separations utilising highly selective molecularly imprinted polymers as biorecognition solvent extraction agents, Biosensors & bioelectronics, 22 (2006) 526-533.
[267] A.F. Barton, Handbook of polymer-liquid interaction parameters and solubility parameters, First ed., Routledge, 2018.
[268] Z. Ranjbar, S. Rastegar, Influence of co-solvent content on electro-deposition behavior of acrylic lattices of different glass transition temperatures, Progress in Organic Coatings, 57 (2006) 365-370.

[269] K. Rezzadori, F. Marques Penha, M.C. Proner, G. Zin, J.C. Cunha Petrus, P. Prádanos, L. Palacio, A. Hernández, M. Di Luccio, Evaluation of reverse osmosis and nanofiltration membranes performance in the permeation of organic solvents, Journal of Membrane Science, 492 (2015) 478-489.
[270] P. Teas J, Graphic Analysis of Resin Solubilities, Journal of Paint Technology, 40 (1968) 19-25.
[271] C. Andecochea Saiz, S. Darvishmanesh, A. Buekenhoudt, B. Van der Bruggen, Shortcut applications of the Hansen Solubility Parameter for Organic Solvent Nanofiltration, Journal of Membrane Science, 546 (2018) 120-127.
[272] S. Kitamura, T. Yoshioka, K. Nakagawa, T. Kitagawa, Y. Okamoto, A. Matsuoka, E. Kamio, H. Matsuyama, Organic solvent reverse osmosis characteristics of TiO2-ZrO2-organic chelating ligand (OCL) composite membranes using OCLs with different molecular sizes, Separation and Purification Technology, 315 (2023) 123576.

Publication list

Deng Luyao, Gonzales Rolly Ralph*, Matsuyama Hideto*, et al, Carbon nanotube intermediate layer intercalation and its influence on surface charge of thin film composite membrane, submitted. (***Chapter 2***)

Deng Luyao, Gonzales Rolly Ralph, Matsuyama Hideto*, et al, Carbon nanotubes regulated polyamide membrane by intercalation to improve the organic solvent nanofiltration performance, Carbon, 216 (2024) 118582. (***Chapter 3***)

Deng Luyao, Gonzales Rolly Ralph*, Matsuyama Hideto*, et al, Organic solvent separation using carbon nanotube-interlayered thin film composite membrane, Chemical Engineering Journal, 473 (2023) 145197. (***Chapter 4***)

Doctoral Dissertation, Kobe University
“Intercalation of carbon nanotube layer for fabrication of high-performance thin film composite membrane for efficient separation (効率的分離のための高性能薄層複合膜作製を目指したカーボンナノチューブインターカレーションに関する研究)”, 139 pages
Submitted on January 15, 2024
When published on the Kobe University institutional repository /Kernel/, the publication date shall appear on the cover of the repository version.